Report Title:	Investigation of “Smart Parts” with Embedded Sensors for Energy System Applications
Type of Report:	Final
Reporting Period:	10/1/2013—09/30/2017
Principal Author:	Yirong Lin, PhD
Date Report Issued:	November 30, 2017
DOE Award Number:	DE-FE0012321
Submitting Organization:	**The University of Texas at El Paso** 500 W. University, ENG. Annex Suite - A111 El Paso, TX 79968

Disclaimer:

This report was prepared as an account of work sponsored by an agency of the United States Government. Neither the United States Government nor any agency thereof, nor any of their employees, makes any warranty, express or implied, or assumes any legal liability or responsibility for the accuracy, completeness, or usefulness of any information, apparatus, product, or process disclosed, or represents that its use would not infringe privately owned rights. Reference herein to any specific commercial product, process, or service by trade name, trademark, manufacturer, or otherwise does not necessarily constitute or imply its endorsement, recommendation, or favoring by the United States Government or any agency thereof. The views and opinions of authors expressed herein do not necessarily state or reflect those of the United States Government or any agency thereof.

Table of Contents

List of Tables

List of Figures

CHAPTER 1 EXECUTIVE SUMMARY

The goal of this proposed research is to design, fabricate, and evaluate "smart parts" with embedded sensors for energy systems. The "smart parts" will be fabricated using Electron Beam Melting (EBM) 3D printing technique with built-in piezoceramic sensors. The objectives of the proposed project are: 1) Fabricate energy system related components with embedded sensors, 2) Evaluate the mechanical properties and sensing functionalities of the "smart parts" with embedded piezoceramic sensors, and 3) Assess in-situ sensing capability of energy system parts. The second year's research of the research is centered on fabrication of the "smart parts" with considerations of overall material property as well as demonstration of sensing functionalities.

The results for the final report are presented here, including all research accomplishment, project management. Details are included such as: how the design and fabrication of sensor packaging could improve the sensor performance, demonstration of "smart parts" sensing capabilities, analysis on the elements that constitute the "smart sensors", advanced "stop and go" fabrication process, smart injector fabrication using SLM technology, smart injector testing in combustion environments etc. Research results to date have generated several posters and papers.

CHAPTER 2 SMART PARTS FABRICATION

2.1 Electron Beam Melting Technology

EBM fabricates metals parts in a layer-by-layer fashion, and has the ability to work with a range of metal powders. According to Arcam, the recommended materials are Ti-6Al-4V, Ti-6Al-4V ELI, Titanium grade 2, and cobalt-chrome ASTM F75. Due to the early development of EBM technology, parameters for different metals are still being developed. For the fabrication of the "smart parts", the material selected for fabrication by EBM is Ti-6Al-4V due to its excellent mechanical properties and it corrosive resistance. In order to fabricate the desired parts, the design is created as a ".stl" file and further layered by the Arcam builder software. The powder metal is melted using an electron beam at roughly 30mA, using a power of 60 keV in a vacuum chamber of 10^{-4} Torr. EBM can be described as a three-step process: 1) the powder is evenly distributed in 70μm thick-layers using the raking system; 2) the electron beam then strikes the powder with a low intensity to sinter it; 3) the powder is then melted with the full power of the electron beam to achieve a fully dense layer. Once the three steps are completed, the build table is lowered one layer thickness, and the three steps are replicated until the 3D component is complete. Figure 2.1 shows the Acram S-12 machine used for the fabrication of "Smart Parts", available at the W.M. Keck Center for 3D Innovation at UTEP.

Figure **2** shows the images of fabricated "smart parts" without embedded sensor using the ARCAM system.

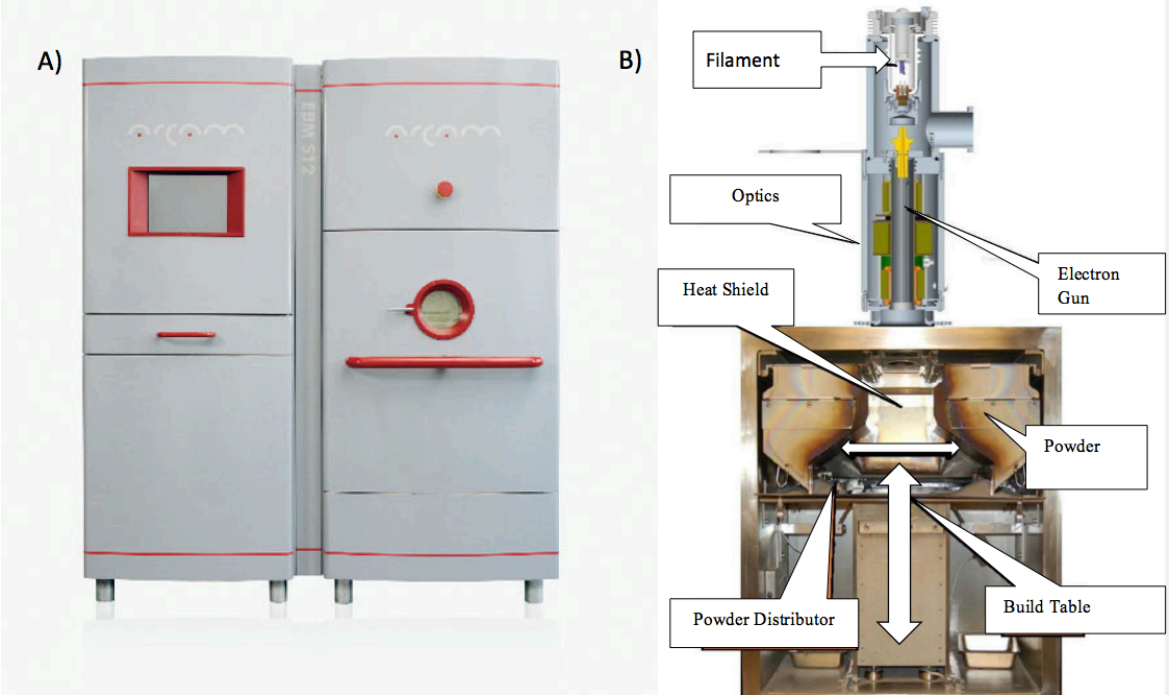

Figure 2.1: (A) The Arcam S-12 machine used for the fabrication of the "Smart Parts" and (B) schematic of the machine with key components labeled.

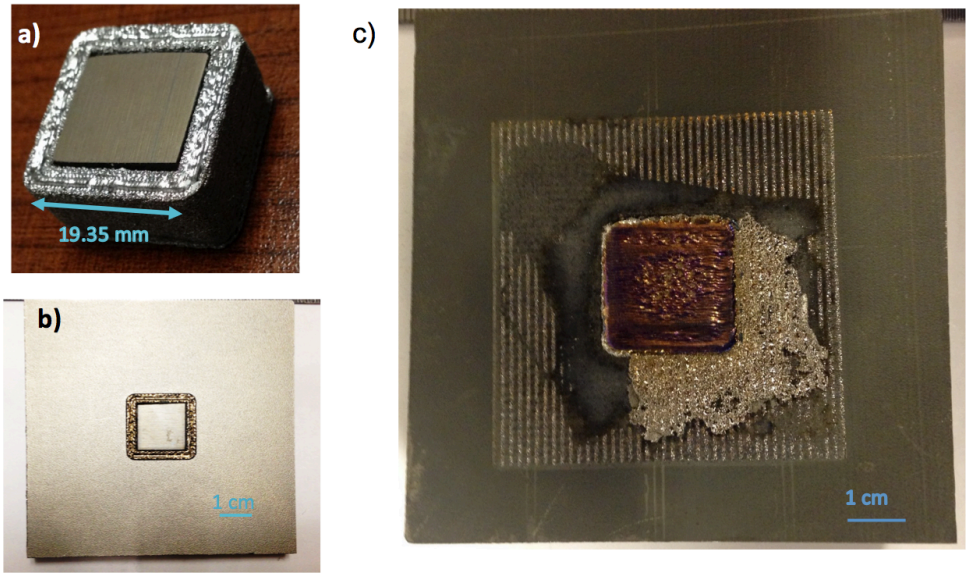

Figure 2.2: Images of fabricated "Smart Parts", (a) bottom part consisting of piezoceramic sensor and insert part, (b) the bottom part press fitted in the mast plate, and (c) fabricated "smart part" (with mask plate surrounding the part).

2.2 Titanium Alloy Fabrication

Preliminary fabrication process was carried out using EBM for both mechanical testing samples and energy conversion components. EBM is one type of rapid prototyping techniques using a chosen metal powder, e.g. titanium, stainless steel or other alloy that is melted and manufactured in a layer-by-layer fashion using an electron beam in vacuum. Computer generated models inputted into EBM machine are decomposed into slices with thickness typically less than 100 μm. Digitally controlled techniques then guide the fabrication process to final product. Given the ability to use various metals with controlled porosity, including titanium alloys, EBM has been used extensively in biomedical component fabrication, e.g. orthopedic implants. The EBM system used for our fabrication is ARCAM A2, where the cross sectional view of the EBM is shown in Figure 2.1. The system builds 100 μm thick layers from bottom to top by selectively focusing the electron beam to melt specific areas of the powder bed while simultaneously powder is continuously added from the powder cassettes from the top. The rake shown at in Figure 2.1 moves laterally between the two powder cassettes to evenly distribute powder layers over the surface after each prior build layer is complete. As each fabrication process is completed, the build table moves down.

In order to build samples for mechanical properties testing, samples with cylindrical cross section were fabricated, as shown in Figure 2.3 (a) and (b) below. We also fabricated metal parts with the same dimension as energy conversion parts such as swirler, fuel injector, and pre-mixer, as shown in Figure 2.3 (c), (d) and (e). The success of energy conversion parts fabrication has demonstrated the feasibility of using EBM to fabricate parts with complicated structure and trivial details. Therefore, it proves the feasibility of run the "stop and go" process during the fabrication process for the piezoelectric sensor embedding, ultimately leading to the "smart parts" with embedded sensing capabilities.

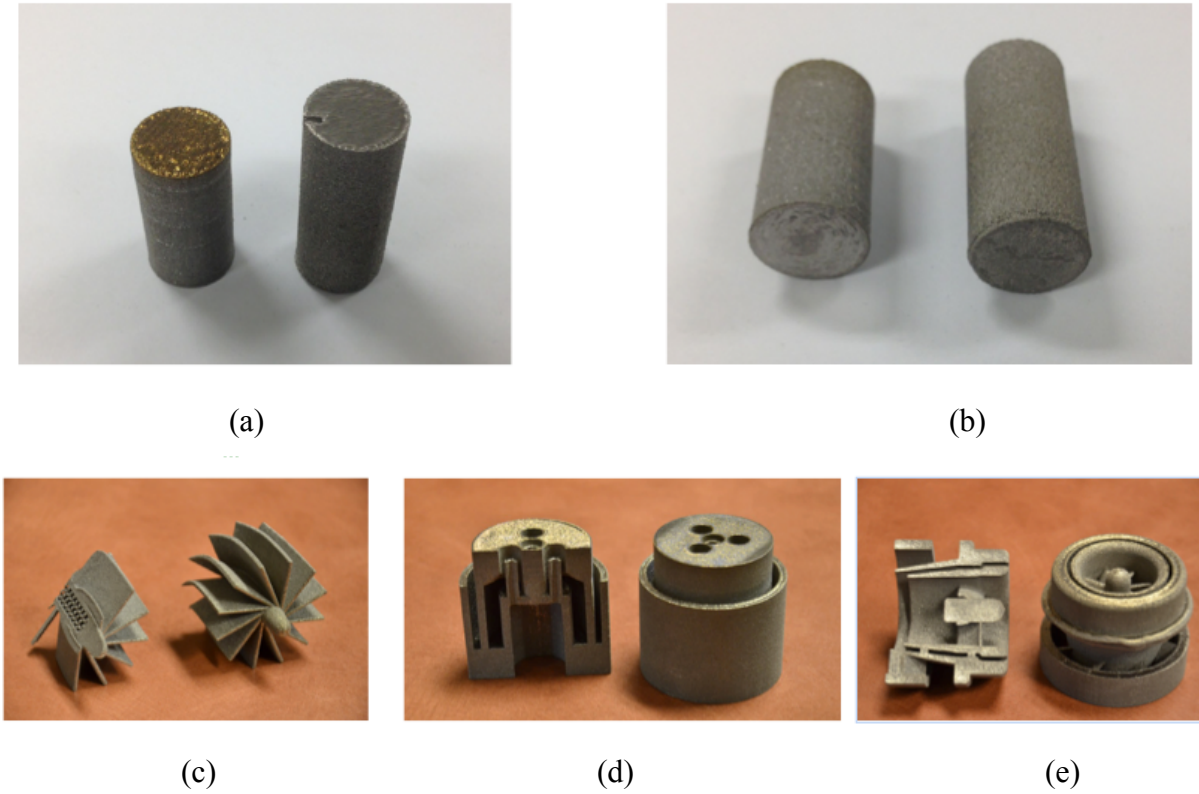

(a) (b)

(c) (d) (e)

Figure 2.3: Photos of (a) angle view of fabricated cylinders, (b) top view of fabricated cylinders, (c) swirler fabricated by EBM, (d) fuel injector fabricated by EBM, and (e) pre-mixer fabricated by EBM

2.3 Simulation of Smart Parts

Simulation was designed to obtain an approximation of the behavior of the sensor under combined conditions of temperature, pressure, and time. The main objective is to estimate an electrical response that will support the calibration results as well as tracking the performance of the sensor (see Figure) during operation.

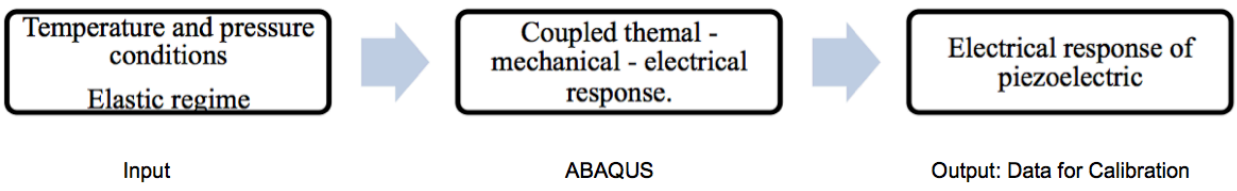

Figure 2.4: Conceptual design of simulation for piezoelectric sensor.

For this report, a 3D model simulation is being done in ABAQUS under the assumptions that perfect contact and zero thermal resistivity exist on the interface. Mechanical and piezoelectric properties of the different materials were obtained in literature. The simulation assumes transient heat transfer, which depends on the temperature conditions – starting at room temperature and raising it up to 1000°C.

As preliminary simulation, a simplification of the problem that includes the piezoelectric ceramic and the alumina coating is presented in Figure . Transient heat transfer, as well as coupled thermal displacement response was achieved at this stage of the simulation. The thermal rate was 19.5°C/s from 25°C to 1000°C. Further studies will include the implementation of piezoelectric properties to obtain a relationship between voltage and temperature, and the inclusion of the other parts of the sensor.

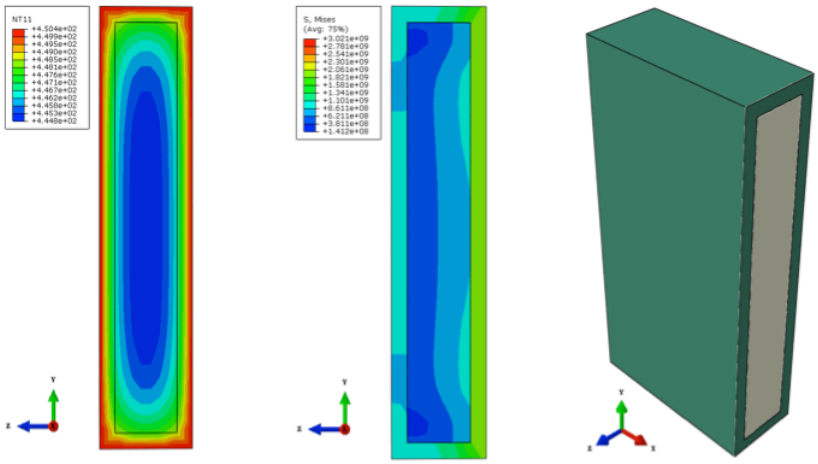

Figure 2.5: Preliminary results on 3D simulation of piezoelectric ceramic and alumina coating. Results of temperature distribution (left) and von mises stress (middle) are presented.

2.4 Simulation of Temperature Gradient in "Smart Parts

To study the temperature profile across the whole "smart parts", a transient heat transfer simulation in Abaqus 6.13 was performed to investigate the heat profile of the components during the second fabrication in the Arcam S12 (EBM). The objective of the analysis was to determine the maximum temperature of the piezoceramic, and to compare the possible evaporation of alloy components that were being coated inside the cavity.

The simulation consisted in five steps that were taken from the temperature reading of the thermocouple positioned beneath the mask plate during the actual fabrication. The reading (see Figure 2.4) consists in preheating until 500 °C (~700s), holding section for degasing during 750s, preheating continues until 736 °C (~450s), building (~1900s), and cooling (~2600s). The electron beam provides power at 30 kV and alternating current during preheating and building sections.
To simplify the complexity of the problem the assumptions included:

- No mass transfer during the building step.
- Heat flux as source of power on the mask plate. The value used was optimized to be closer to the actual measurements. The initial value was obtained considering the average of the alternating current (343±283 W). The optimized value was 641 W.
- Heat flux loss from the film condition. In reality, the mask plate is embedded in a bed of Ti6Al4V powder. A correct calculation of the heat transfer coefficient from the thermocouple to the ambient temperature required readings on more surfaces of the EBM machine. These limitations were addresses by assuming a film condition coefficient (h) to be $h=k/L$ was k is the thermal conductivity of the powder bed of Ti64 and L is the height of the bed. The maximum value was calculated to be $h=64$. Nonetheless, after optimization of this value, the final was $h=2.5$.
- During the building step, concentrated heat flux in center point of top surface of assembly was used.
- No heat losses in the interface of the components.
- No heat transfer radiation from the top of the mask plate.

The simulation included a stainless steel mask plate, two alumina plates, a LiNbO3 plate, and a Ti64 cavity.

Table 2.1: Material and geometry properties of the components used on the simulation.

Material	Geometry	Thermal Conductivity (W/m °C)	Heat Capacity (J/kg°C)	Density (kg/m^3)
Stainless Steel	15x15x1 cm	15.4	497	7830
Al_2O_3	5x5x1 mm	25	880	3900

$LiNbO_3$	10x10x1 mm	4.18	628	4650
Ti6Al4V	Cylinder 20xØ2435 mm Cavity 12x12x11 mm	6.7	526	4430

Detail of the geometry of the cavity and the overall assembly is shown in Figure ,

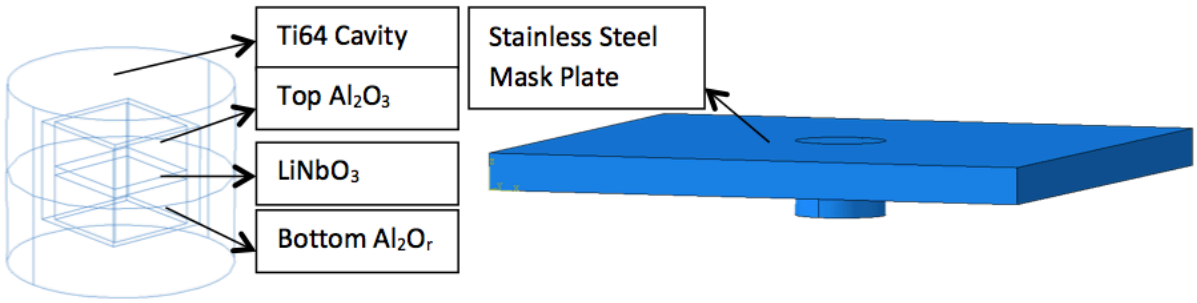

Figure 2.6 Wireframe for Ti64 cavity (left) and assembly with the stainless steel mask plate (right).

The mesh was formed by 122049 linear tetrahedral elements of type DC3D4 for heat transfer analysis. Detail towards the cavity and sensor components can be observed in Figure and Figure . No distorted elements were used.

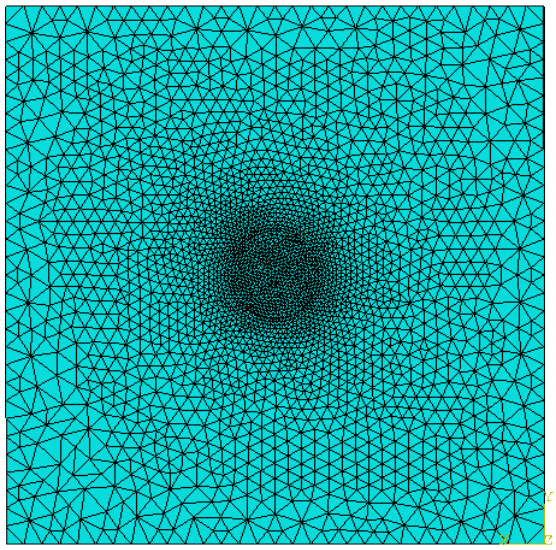

Figure 2.7 Mesh detail from the bottom view of the assembly.

The simulation consisted in five transient steps:

1. Preheating by heat flux of 28.5 kW/m2 located at the top surface of assembly for 700s.
2. Removal of heat flux for 12.5 min.
3. Preheating continues with parameters of no. 1.
4. Building by specifying temperature of 1700 °C on the center point at the top surface of the cylinder.
5. Removal of all heat sources.

All steps included constant heat loss from the bottom and side surfaces with a film surface coefficient of 2.5 (W/m^2C). The nodal temperature profile of the cross section is shown at the ending of each step in Figure 2.3. Furthermore, a comparison between several points in the cavity during the all the steps is presented in Figure .

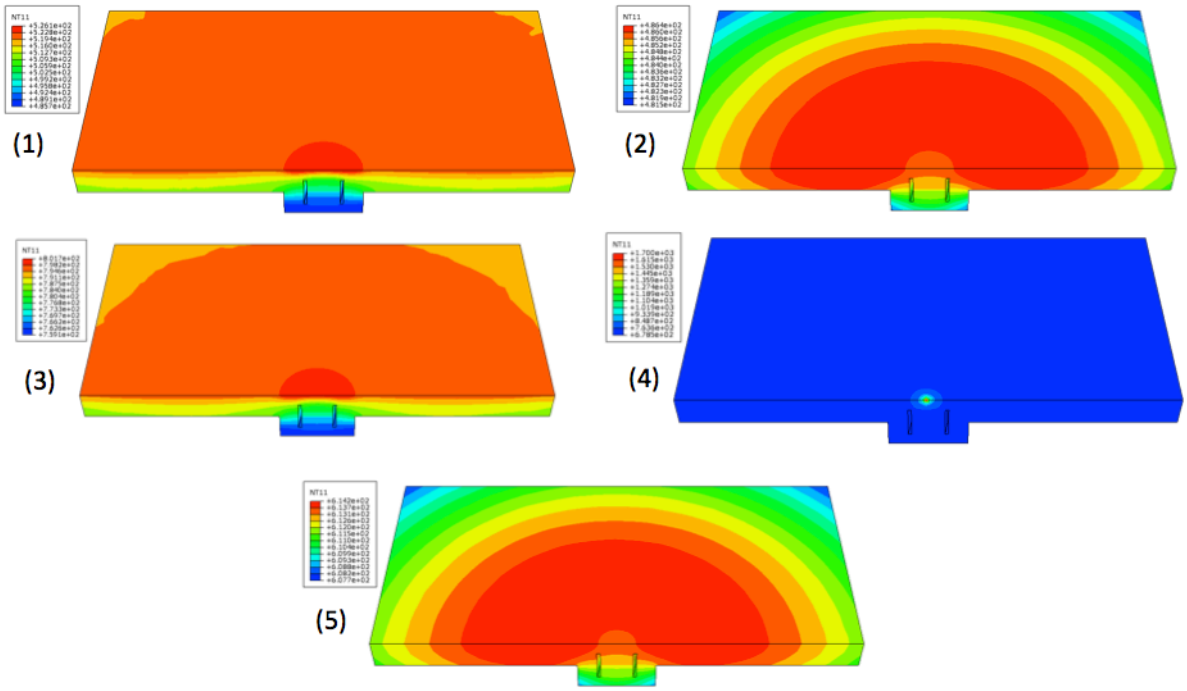

Figure 2.3 Temperature profile at the end of each step of the simulation. Initial preheating (1), holding (2), resume preheating (3), building (4), cooling (5).

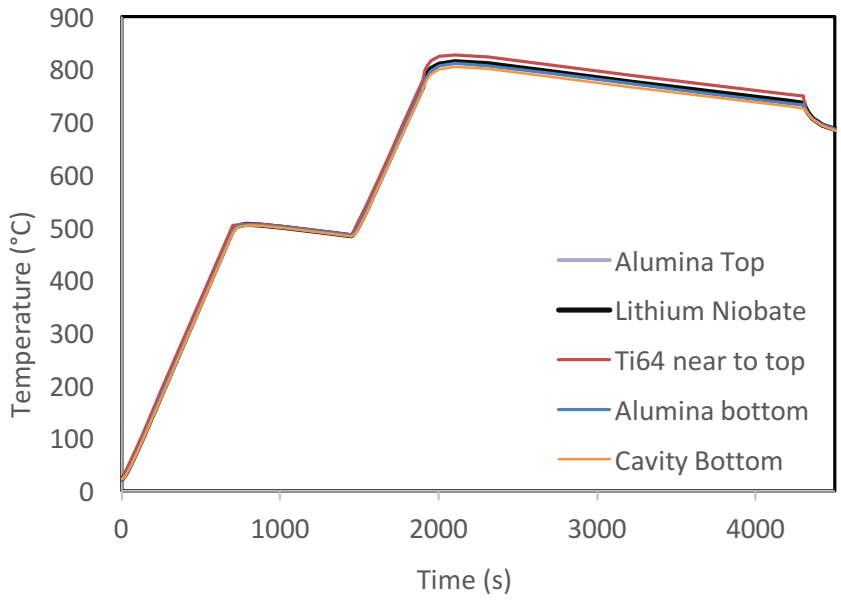

Figure 2.9: Temperature from different locations of nodes in the centerline of the sensor (cylinder).

It is observed that the variation of temperature achieved by the preheating stage, remain throughout the components of the sensor cavity. Finally, the comparison between the thermocouple and the simulation is presented in Figure 2.4.

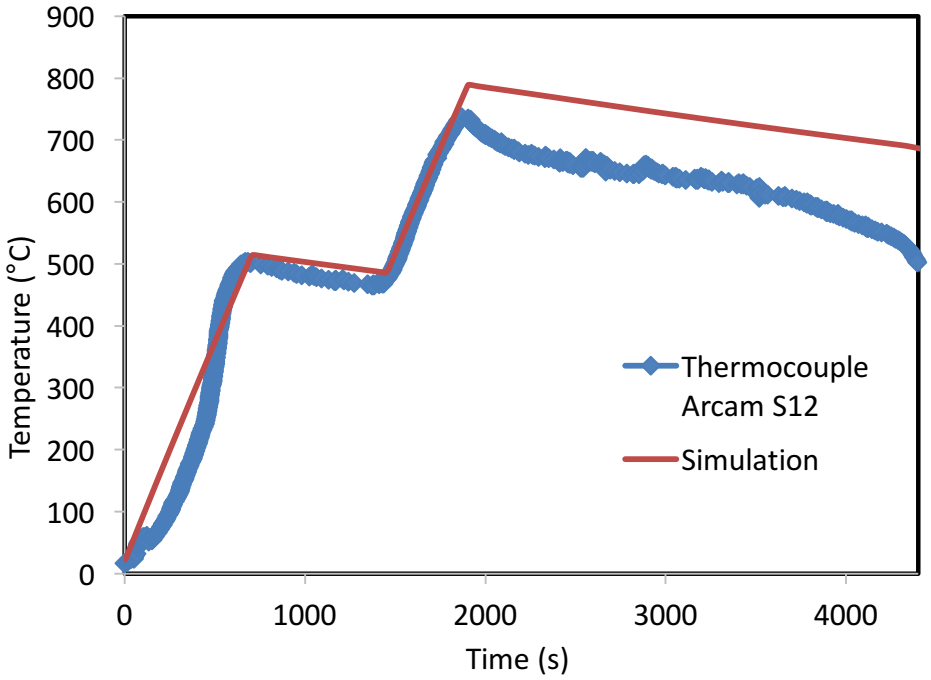

Figure 2.4: Comparison of temperature between the thermocouple and simulation.

The deviation of Figure 2.4 is a consequence of the optimization process. Although accuracy on the assumptions should be addressed, the results shows that from a concentrated heat source on a single point during fabrication, is not enough to reach Curie temperature of $LiNbO_3$.

2.5 "Smart Parts" Preliminary Force Sensing Demonstration

The sensor was designed to be built by a layered assembly. The assembly contains six layers of different materials stacked into the cavity of the fabricated base. These materials (see Figure 2.5) are alumina (AI203) plates (1st and 5th layer), electrodes built by joining titanium wires (Aldrich GF69168662-1EA) and titanium foils (2nd and 4th layer), a piezoceramic (3rd layer; PZT) element that acts as sensing material for temperature and pressure, and the insert part (6th layer) that closes the cavity that is fabricated with EBM technology. Ideally, the insert part would be pressed fitted into the cavity, but for this demonstration, the edges were reduced for better handling and facilitate corrections during fabrication.

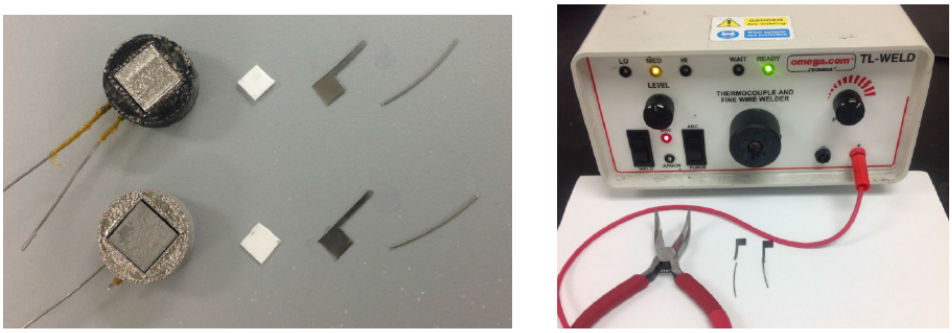

Figure 2.5 Sensor prototypes used to evaluate the response under cyclic displacement (right). The elements used are alumina plates, titanium foil (electrodes) and titanium wires. A thermocouple welder (TL-WELD) was used to join the titanium wire with titanium foil.

The electrodes and the piezoceramic were cut in smaller sizes hence no contact would be caused between the walls of the cavity. Electrical insulation of the titanium wires was achieved by using insulation tape (see Figure 2.5). Two sensors with same layered procedure were fabricated and tested for the response under cyclic displacement.

The sensors were tested in a Low-Capacity 8800 Servohydraulic Fatigue Testing Instron machine (see Figure 2.6). Preliminary testing was done to find the relationship between load and displacement, since a displacement control is more stable; this testing determined safe values of parameters for displacement control. The experiments methodology included two modes:

1. Single step displacement control method, cyclic amplitude (compression-compression, compression-release), and different frequencies (0.25 Hz, 0.5 Hz, 1 Hz, 2 Hz, 4Hz, 10Hz) for 10 cycles.
2. Three multi-step displacement control method, cyclic amplitude (compression-compression, compression-release) - decreasing amplitude by half each step, and different frequencies (0.25 Hz, 1 Hz, and 10Hz) with 10 cycles each step.

To record voltage response, an oscilloscope (RIGOL DS1102E) was used. (as shown in Figure 2.6). Because of the layered and the testing setup, a predefined stress was needed on the sensor before testing. This stress was defined previously by calculating the mean line of the sinusoidal function of force, thus the peaks fell in the compressive-compressive stress region, and the compressive-release region.

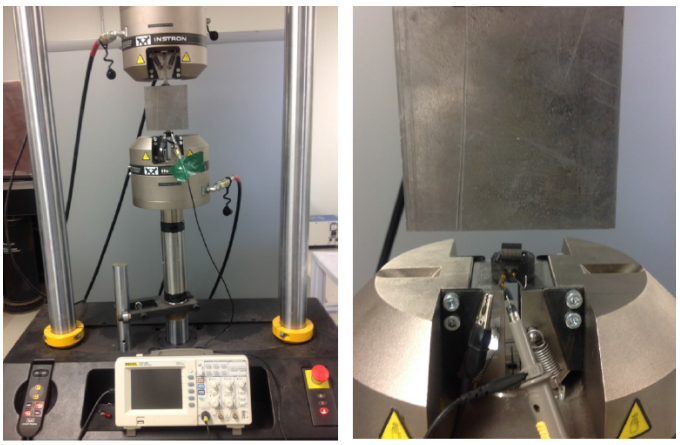

Figure 2.6 Instron machine and testing setup (right). Closer view (left) in which fabricated sensor is positioned before testing.

The results obtained from the experiments showed good agreement in the frequency and very low noise for the Instron machine outputs. Contrarily, human error and noise levels were presented in the voltage readings. The shifting caused by the human synchronization of the oscilloscope was reduced by correcting the time axis of the voltage with the first peak of the force output. Additionally, a smooth process was done in the voltage signal using a smooth ratio of 0.005 to preserve true peaks heights and widths (see Figure 2.7).

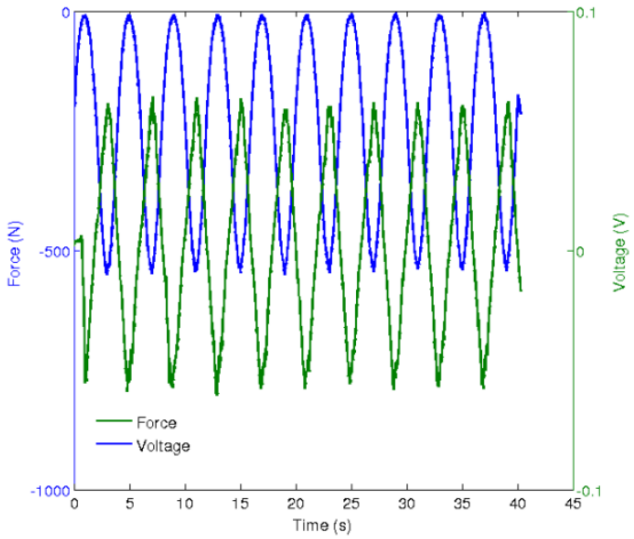

Figure 2.7 Synchronized values for voltage and force from an experiment done in one sample at 0.25 Hz, with amplitude of 20 microns.

The analysis is focused on studying the ratio between amplitude of force to voltage. Statistical considerations included a Chauvenet's criterion [2] for the rejection of outliers during experimentation, and hypothesis testing to compare means of independent samples [2]. For single step process, results from the samples on the single step method are summarized in Figure 2.8 . The results showed that the sensitivity of the piezoceramic reduces as the frequency of loading increases. The intensity of the response is attributed to the mass of the piezoceramic, since the peak force deviation is only 5% for both samples. The trend would be explained by an exponential decay, but the discrepancy of the sample 2 at 4 Hz requires further testing to demonstrate the mathematical correlation.

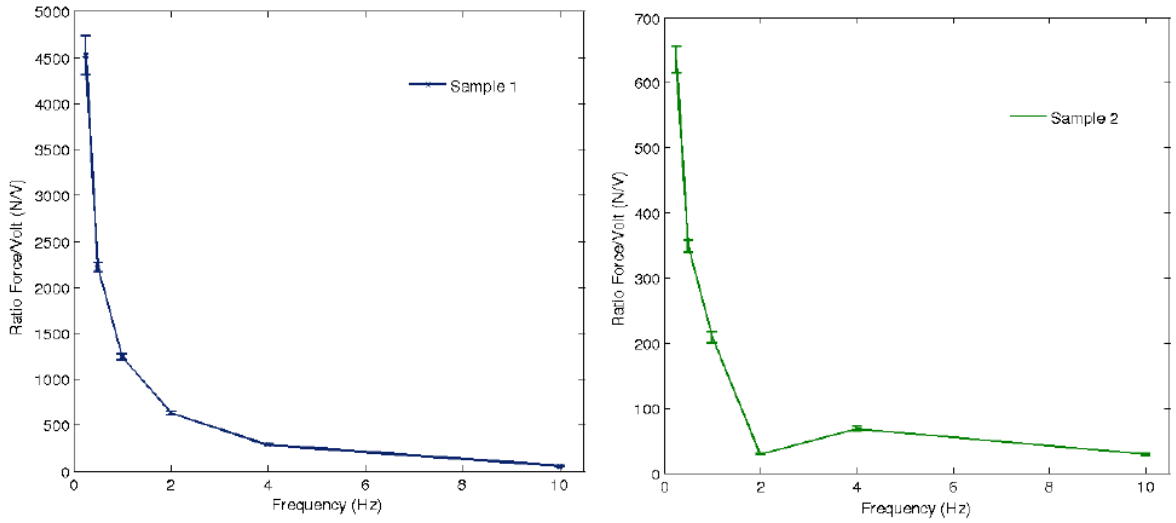

Figure 2.8 Single step method; each point represents the average of the 10 cycles at different frequencies with 95% confidence interval bars.

For Multi step method, summary of the results are shown in Figure 2.9 and Figure 2.10 . For both samples, a similar behavior was observed when frequency of the cyclic displacement was increased. The results were processed by tens of cycles. Average and sample standard deviation was taken. To verify the amplitude of the force, a Chauvenet's criterion was applied to the data to identify outliers values from experimental trend. The criterion was applied since the repeatability was observed and the normal distribution of the data was confirmed. The deviation was reduced, resulting a maximum standard deviation at 0.25 Hz at the 21-30 cycles of 15%.

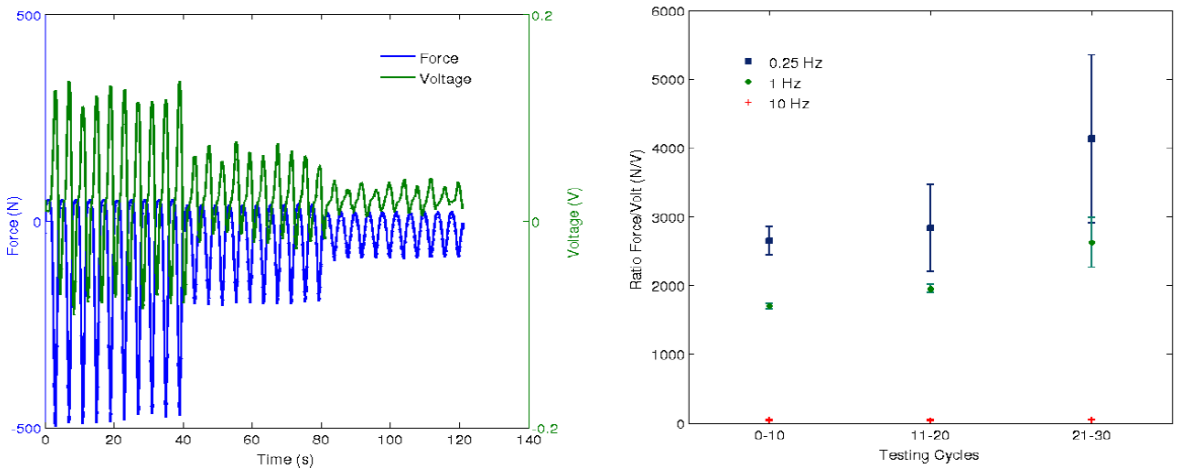

Figure 2.9 Multi-step method for sample 1 showing the synchronization of force and voltage (left), and the summary of the results (right). Each point represents the average of the testing cycles, and the bars represent the 95% confidence interval.

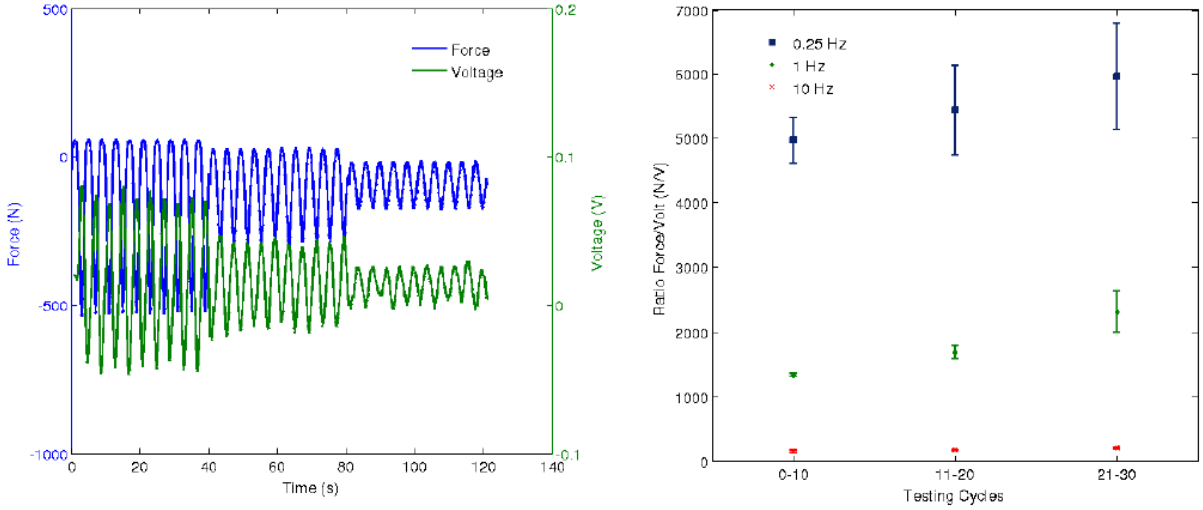

Figure 2.10 Multi-step method for sample 2 showing the synchronization of force and voltage (left), and the summary of the results (right). Each point represents the average of the testing cycles, and the bars represent the 95% confidence interval.

To further investigate the trend in the results, the samples averages were compared using hypothesis testing. The analysis showed, for each experiment, that each set of 10 cycles were independent of the other two (with at least 95% confidence) except at 0.25 Hz of Figure 2.10

between the first set (1-10) and second set (11-20) with 88% confidence that they were different (Table 2.2).

Table 2.2 Sensitivity increase between set of cycles shown in shown in Figure 2.9 and Figure 2.106. 1st, 2nd and 3rd corresponds to 1-10, 11-20 and 21-30 testing cycles' values. Exception from hypothesis testing that shows only 88% that 2nd and 1st corresponds to different sample means.

	Sample 1 (Figure 2.9)		Sample 2 (Figure 2.10)	
Set Relation	2nd to 1st	3rd to 2nd	2nd to 1st	3rd to 2nd
0.25 Hz	9%	9%	**7%	31%
1 Hz	21%	27%	13%	26%
10 Hz	10%	16%	-2%	16%

The results of Table 2.2 showed no clear trend among results. There is an equal increase at 0.25 Hz of sample 1, but at higher frequencies variation occurs to 6%. In contrast, the exception of 7% and the high deviation occurring at the 3rd set of 0.25 Hz of sample 2, impedes a good comparison with sample 1.

2.6 Preliminary Concept of "Smart Parts" Fabrication

The piezoceramic sensors embedded in energy system components (e.g., exhaust tubes, gas turbine fuel/air premixers, etc.) or "smart parts" fabrication is performed using the EBM system. As an initial step, a rectangular prism shape part with an embedded sensor was fabricated. The illustrative figure along with dimensions is shown in Figure 2.11 (a) and partial inside view is shown in Figure 2.11 (b). The simple design of "smart parts" was fabricated to establish the proof of fabrication process. The process will be applied to fabricate energy system components in the future. The dimension of simple design "smart parts" was 19.35mm × 19.35mm × 15.15mm. A cavity of 9.35mm × 9.35mm × 4 mm was designed for the piezoceramic sensor and alumina paste. The piezoceramic sensor was inserted in the cavity of the "smart parts" surrounded by an alumina paste, 989 Ceramic (COTRONS CORP., Brooklyn, NY), used to separate the piezoceramic sensor from the Ti-6Al-4V metal. The purpose of the paste is as protective insulation and positioning in

the desired location. The thickness of the alumina paste used was approximately 1.5 mm. A seating place of 14.30mm × 14.30mm × 3.15mm, was considered in the design for the insert part (previously cut Ti-6Al-4V part). In addition, two circular cavities of 1.5 mm in diameter were made for wiring purposes, as shown in Figure 2.11.

The fabrication of "smart parts" is a multi-step process, which is achieved by interrupting the EBM fabrication after the desired height (in this case 12.15 mm) is fabricated. Then, the piezoceramic sensor with mounting assembly (alumina paste and insert part) are embedded in the cavity. The process then continued to finish the fabrication by building the last 3mm of the build (top part). The entire fabrication process, referred as "stop and go", is shown in Figure . The "stop and go" process consisted the following six steps:

Step 1: Fabrication of the 1st or bottom part (with cavity) using EBM system.

Step 2: Cutting of the "insert part" from Ti-6Al-4V bar.

Step 3: Interruption of the fabrication and embedment of the piezoceramic sensor.

Step 4: Machining of the mask plate using CNC Mini Mill 2 (HAAS Automatic Inc. USA) machine.

Step 5: Press fitting of the bottom part in the mask plate and aligning of the top surface.

Step 6: Fabrication of the rest of the part (on top of the bottom part).

Step 7: Cleaning of the finished "smart part".

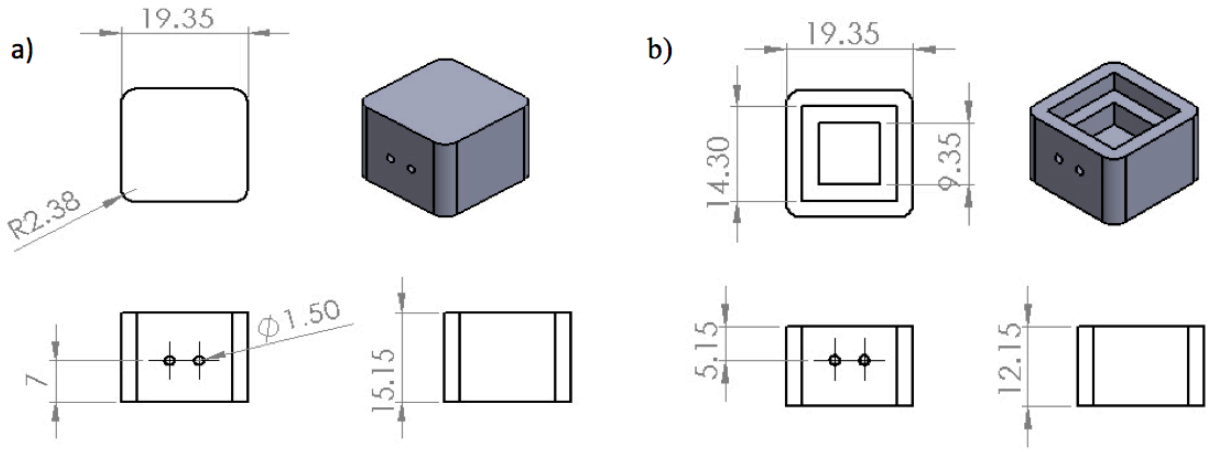

Figure 2.11: (a) blue Print drawing of "Smart Parts", (b) partial view (3mm offset from the top) of "smart parts".

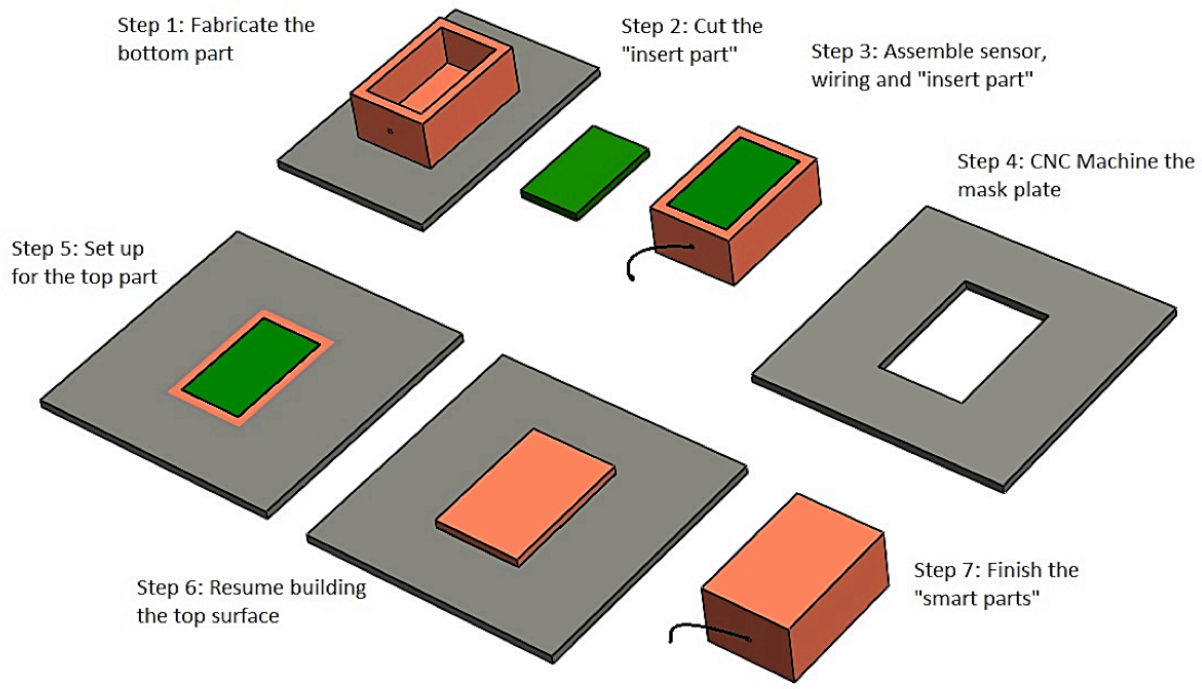

Figure 2.18: Schematic diagram showing the sequence of "stop and go" process.

2.7 High Temperature Wiring and Sensor Material

The purpose of high-temperature wiring is to guide a sensing signal out from the piezoceramic sensor in the "smart parts" when used in energy conversion applications. The piezoceramic sensor works under a piezoelectric and dielectric-shifting principle of the material's dielectric property. Aside from piezoelectric properties, where strain, vibration, and pressure can be sensed, the piezoceramic material will have a corresponding dielectric value, when the temperature changes, the dielectric value of the piezoceramic will shift accordingly. The dielectric-shift will cause a corresponding change in the capacitance measured from the piezoceramic material. Thus, the sensor can be calibrated according to a temperature-capacitance relationship that will make temperature sensing possible. The piezoceramic chosen for this application is Lithium Niobate ($LiNbO_3$) due to its high Curie Temperature (1100°C), which is the maximum service temperature for piezoceramics. Figure below shows a piezoceramic sensor that will be embedded in the smart parts for demonstration.

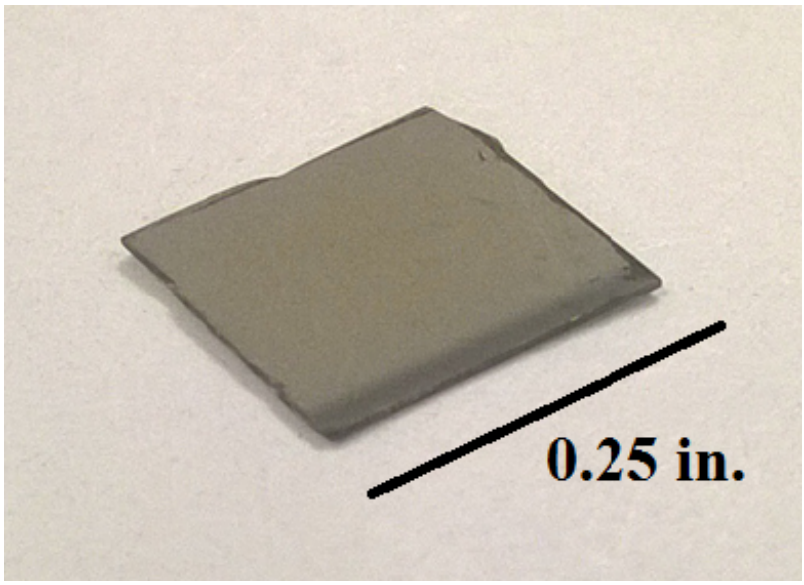

Figure 2.19: Thin piezoceramic material to be used as the sensor. Dimensions of the piezoceramic are 0.25 by 0.25 inches.

The wiring needed for this type of application needs to meet special demands. The wiring must be able to resist high-temperatures and harsh-environments. Thus a metal with a high-melting point which is corrosion and oxidation resistant is preferable. The wiring must also offer adequate electrical conductivity (low electrical resistivity) in order to better transmit the sensing signal out from the piezoceramic sensor. One commonly used wiring material that meets these requirements is Platinum: a chemically stable metal at high-temperatures and harsh-environments with good electrical conductivity. Titanium also has a high-melting point and is corrosion resistant, it is also chemically similar to the building material used to manufacture the sensor structure, and thus should not pose a powder contamination problem during the EBM build phase. The electrical conductivity of Titanium is not as good as Platinum, but it is considerably more inexpensive. Titanium will be considered to prove the concept that a sensing signal can be transmitted out of the piezoceramic sensor. Once parameters for the manufacturing and parts fitting of the whole sensor structure have been refined, Platinum will be used as the wiring material of choice. Copper offers the best electrical conductivity (lowest electrical resistivity), but it offers poor corrosion and oxidation resistance. Melting point, and electrical resistivity values are given in Table 2.3. Therefore, we are planning on using titanium for the initial fabrication process and would adjust properly if necessary.

Table 2.3 Materials property comparison of potential wiring materials.

Wiring Material	Melting Point	Electrical Resistivity
Platinum	1768.3 °C	(20 °C) 105 nΩ·m
Titanium	1668 °C	(20 °C) 420 nΩ·m
Copper	1084.62 °C	(20 °C) 16.78 nΩ·m

In order to protect the sensing signal from being disrupted or lost, high-temperature electrical insulation will be used to insulate the piezoceramic sensor and the wiring from the rest of the sensor housing. The high-temperature electrical insulation (COTRONS CORP., Brooklyn, NY) considered here comprises of adhesives/cements products that are manufacturer-designed for this specific purpose. These products all offer an exceptionally high-temperature operation limit (1400+ °C), and are intended to be used for electrical insulating applications.

The performance of the proposed High- temperature wiring elements has been assessed. Assessments have been made on the material selection and design of the High-Temperature Wiring components. The main change of the High-Temperature Wiring involves switching from alumina paste to alumina plates. This change has spurred subsequent design considerations of the layout and material selection of the High-Temperature Wiring.

Originally Alumina paste was considered because it could be easily applied into the sensor-housing cavity, and it could completely fill out the volume of the cavity. Properly applied and cured, the Alumina paste has a service temperature of +1400 °C, making it suitable for the "Stop-and-Go" high build-temperatures of the Electron Beam Melting machine. The main function of the alumina paste is to provide electrical insulation between the piezoelectric sensor and its wiring against the metal sensor housing. This electrical insulation prevents a short circuit of the sensor and helps protect the integrity of the sensing signal. The secondary function of the paste is to serve as a mechanical medium for pressure and heat transfer. Upon drying and curing, the alumina paste becomes a rigid ceramic, thus allowing the transformed alumina paste to serve as a mechanical medium for stress (pressure) and heat transfer. Pressure and heat will be able to be transferred from the surface of the sensor housing to the embedded piezoelectric sensor which will output a corresponding electrical signal.

Severe problems were encountered with the alumina paste as it was incorporated into the

Electron Beam Melting build phase. These problems occurred because alumina paste composition contains water, which must be fully evaporated for the paste to harden completely and become a ceramic. Even after the alumina paste was air-dried well beyond the manufacture's dry time, the high build-temperatures of the EBM caused further evaporation residuals from the alumina paste which contaminated the machines vacuum system. Additional problems arose from the high build-temperature. Extremely high localized temperatures were suspected to cause bubbling and burning of the alumina paste, which left undesirable voids and cavities.

To deal with the EMB contamination issues, it was decided that alumina paste could not be used during the build phase. The current solution is to use alumina ceramic plates, which will sandwich the wiring (electrodes) and the piezoelectric sensor, as schematically shown in Figure 2.12. The alumina plates will serve the same purpose of the alumina paste. A subsequent design consideration to the alumina plates is to machine a slot in the alumina plates so that the contents within, the electrodes and piezoelectric sensor, will be better insulated and restrained. Additionally, in order to accommodate the flat face of the piezoelectric sensor and the alumina plates, titanium foil will be used for the electrodes. Titanium foil is flat, and will provide a stable and effective interface that will not cause undesirable stress-concentrations like a wire on a flat surface would. The wires that protrude from the sensor housing and get the signal out can be welded to the titanium foil using a thermocouple tack welder.

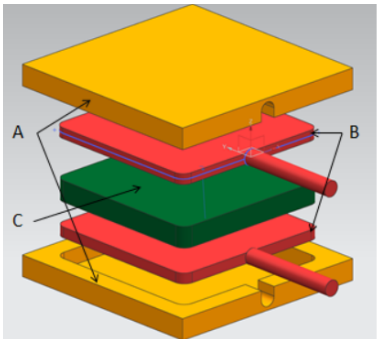

Figure 2.12 A) alumina plate(s), b) titanium foil electrode(s) with welded titanium wires, c) piezoelectric ceramic sensor.

Since the alumina paste will no longer be used during the build phase, and alternative method must be used to insulate the wires from the metal housing. Current solutions are the use of commercially

available insulated thermocouple wire, as shown in Figure 2.13 (High Temperature Wire with Nextel or Silica Yarn Fiber Insulation, OMEGA Engineering Inc.) which already comes with high-temperature (~1000 °C) insulation, or the use of high-temperatures wire sleeves (Very High Temperature Sleeving Nextel Ceramic or 96% Silica, OMEGA Engineering Inc.). The high-temperature wire sleeves use the same material as the insulation of the thermocouple wire, but with the added advantage that the sleeves can be fitted to other separate wires of choice.

Figure 2.13 A) Omega high temperature wire sleeving, b) high-temperature thermocouple wiring.

2.8 Preliminary Design of "Smart Parts" and Fabrication Process

The circular shape "smart part" was fabricated in oppose to the rectangular one in order to avoid registration issue during fabrication of the top part. The diameter of the circular shape "smart part" was 24.35 mm and overall height was 15.15 mm (Figure 2.14). The dimensions of the internal part (insert part, cavity for sensor) were kept similar to that of rectangular one. The only exception was the diameter of the hole was changed to 2.5 mm (Figure 2.14) as the previous diameter of 1.5 mm was not enough to insert the wires into it. In actual, due to shrinkage and some unsintered powder left in the hole, the diameter of the hole was found approximately 2.18 mm.

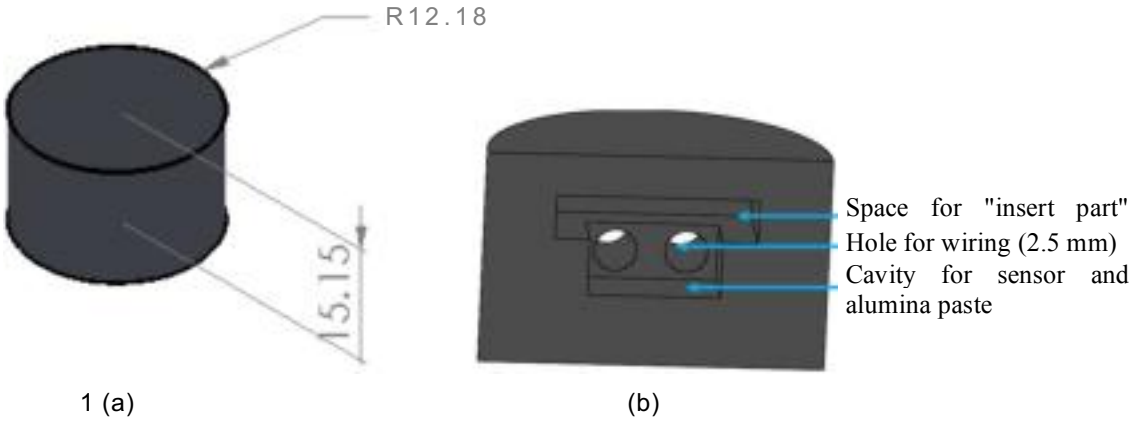

Figure 2.14 Blue print drawing a) 3D view of "smart parts", and b) cross sectional view of "smart part".

The entire "smart part" was built using the "stop and go" process (shown Figure 2.15). The "stop and go" process consist of inserting piezoceramic sensor and insert part in place of bottom section and after that, inserting the entire bottom section into the mask plate. The top part was continued to build onto the bottom part. A misalignment of 435 |jm from bottom part to top part was found after fabrication which was caused due to the alignment of the electron beam. The fabrication process confirms the multiple step fabrication using electron beam melting (EBM) system in compare to the commonly used single build fabrication process.

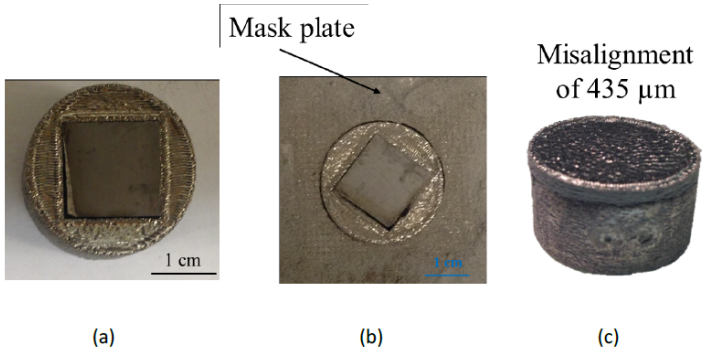

Figure 2.15 Fabricated "Smart Part", a) bottom part consist of piezoceramic sensor and insert part, b) bottom part press fitted into the mask plate, and the entire "smart part".

As a modification of design, a flexible part was added along with cavity for the sensor. The flexible part was considered in the design to minimize the slacking of wires from the alumina and wires which can cause of dismantling of the wires during operation. The schematic diagram along with cross sectional view of the drawing is shown in Figure 2.16. The diameter of the entire part was kept constant at 24.35 mm and diameter of the whole was changed to 4 mm to provide enough space for wiring consisting sleeves. The flexible part is just to fix the wire at that place so that it does not slake during operation and is just a simple addition to the design.

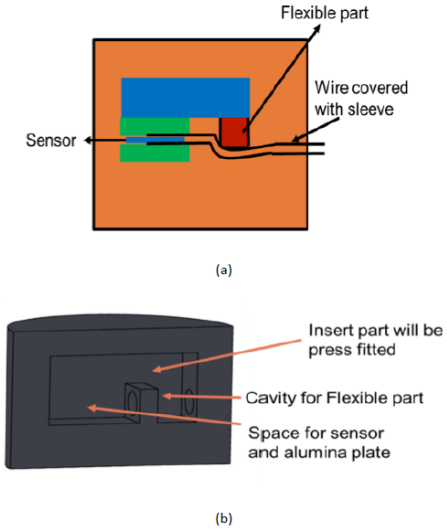

Figure 2.16 Modified design of "Smart Part", a) Schematic diagram, and b) CAS model.

2.9 Metallization Issue of "Smart Parts" Fabrication

To investigate the cause of sensing electrical shorting after fabrication, a completed part was sectioned from the top in order to access the sensor and parts to observe the after build condition. The parts exposed to the EBM were compared to the original parts, and a dark visible coating was present in all parts, as shown in Figure 2.17. The conductive coating appears to be as metal coating at first that occurred during the second fabrication, when the powder was heated to melting point under vacuum. Further investigation was done to determine what the composition of the coating is and how to avoid it in future builds. The metal coating (confirmed by EDS later on) is also one of the main reasons that caused the sensor non-functionality.

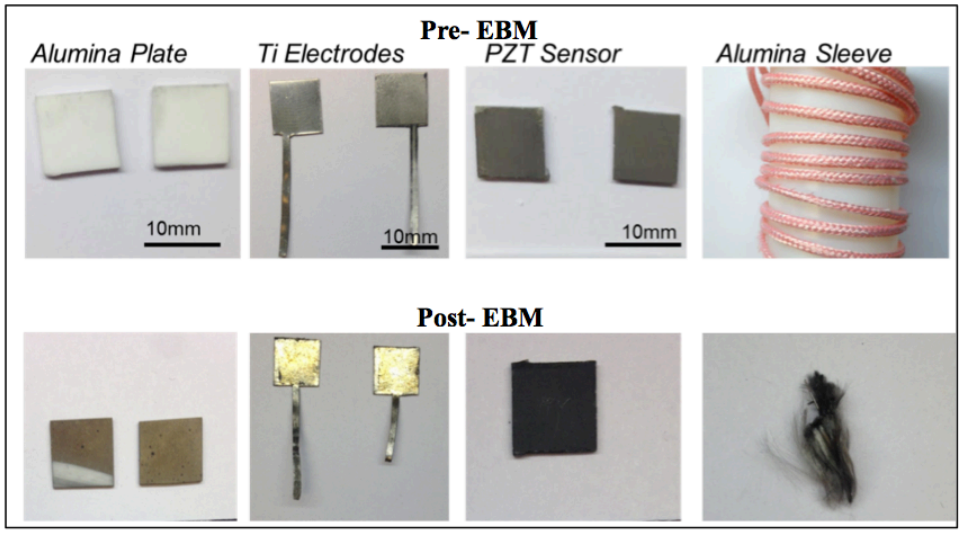

Figure 2.17 Parts included for embedment of sensor inside "smart part". Top images are as-bought before EBM fabrication, where bottom images include post EBM fabrication.

EDX results

SEM and EDS were conducted in order to identify the composition of the coating. Two samples of the alumina plate, as-bought and post-EBM, were analyzed and compared under the SEM. Figure 2.18(a) shows the SEM image of alumina plate as bought, where Figure 2.18(b) shows the SEM image of alumina that appears after EBM fabrication. Table 2.4 shows the difference in composition that is present for both as pre-EBM and post-EBM samples considering only the surface of the alumina. The post- EBM sample has additional titanium that was present, which may be the metal coating that is present on surface. One of the main issues in metallization is assumed to be caused by metal vapor created during fabrication. As the Ti-6Al-4V powder is consist of three different components which have different vaporization temperature that may be the reason to create the metal coating. The vaporization temperature is even low due to the vacuum fabrication process. As a result, any components of the Ti-6Al-4V fabricated parts may metalize the sensor assembly. As a result, insulating components becomes conductive and as so, no sensor reading was obtained.

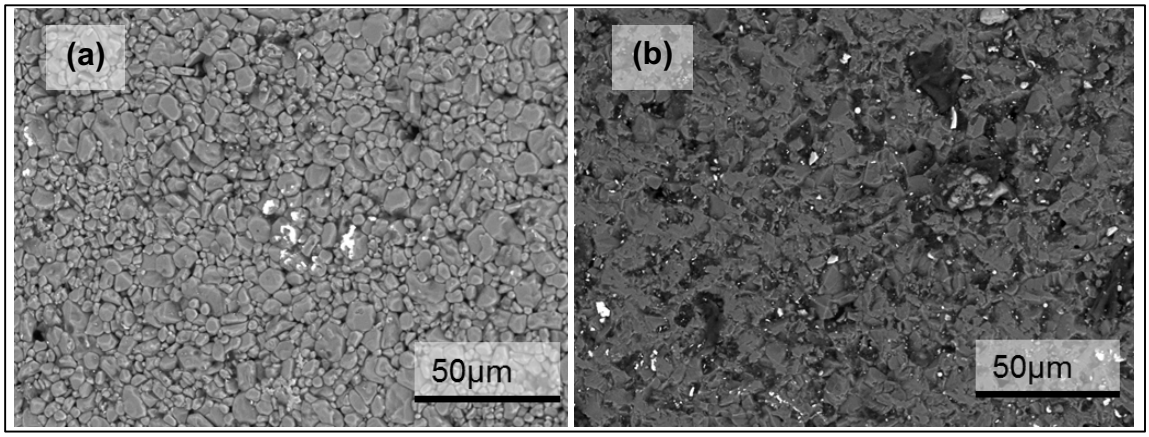

Figure 2.18 Design B of "smart Part".(a) Shows the bottom part with embedded sensor (b) Top view of finished part (c) Side view of finished part.

Table 2.4 EDS Results for the Alumina Plates

Element	Pre-EBM	Post-EBM
Aluminum	98.5%	89.3%
Silicon	1.5%	3.6%
Titanium	0	4.2%

2.10 High Temperature Capable Electrode

The presence of the titanium was observed in the sensor housing. One of the sources of the titanium was titanium electrode that was used in the sensor packaging. The vaporization temperature of the Titanium may not be high enough to overcome the high temperature EBM fabrication process. Platinum, and Tungsten was found to be a better replacement of Titanium electrode as the vaporization temperature is higher for Platinum, and Tungsten, as shown in Table 2.5.

Table 2.5: Metal vaporization temperature as a function of pressure.

Element	Vaporization Temperature (^{0}C)		
Pressure (Torr)	10^{-4}	10^{-3}	10^{-2}
Titanium	1250	1384	1546
Platinum	1744	1904	2090
Tungsten	2767	3016	3309

2.11 Metallurgical Characterization

As a successful "Smart Part" was fabricated using EBM, the part was then cross- sectioned and analyze for further classification of microstructure and hardness. The part was sectioned using the Buehler Isomet 4000 Linear Precision Saw. The sectioned part was then polished and etched using Kroll's Reagent, which is 92% water; 3% hydrofluoric acid; and 5% nitric acid, in order to view the alpha and beta phases that may be present. After etching, the part was looked under the optical microscope. Figure 2.19 shows optical view of the microstructures using 100 x magnifications. The top and bottom sections have a similar Widmanstatten or Lamellar-like microstructure, which referrers to the fine needle like structure that is arranged in alternating a and (B phases. The insert plate, which was commercially bought, has a more equiaxed a and (B mixture microstructure, which may have better isotropic properties when compared to the top and bottom sections. The sensor was also polished and etched; the sensor is a lead zirconate titanate (PZT) material. The microstructure of the sensor will be analyzed for understanding sensing properties. Figure demonstrates the type of interface that was created between the insert plate and the top section of the "smart part". Even though there is a solid bond between the two parts, a discontinuity of microstructure is visible, which may affect the mechanical properties of the "smart part".

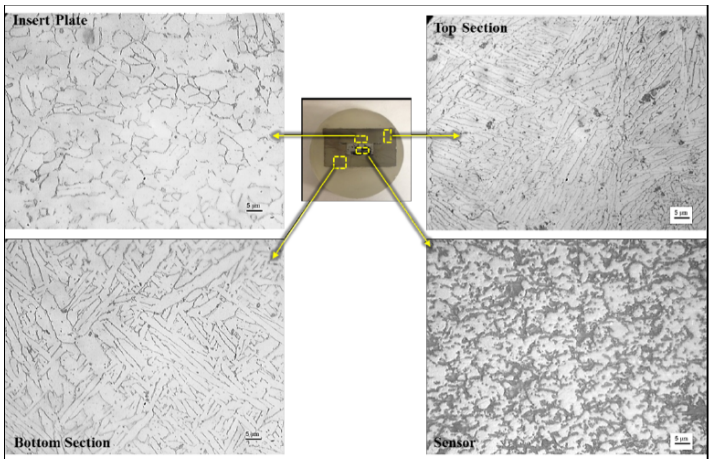

Figure 2.19 The 4 different sections that are present on "Smart Part". Bottom and top section have a more Lamellar microstructure when compared to the insect plate. The sensor consists of lead zirconate titanate material.

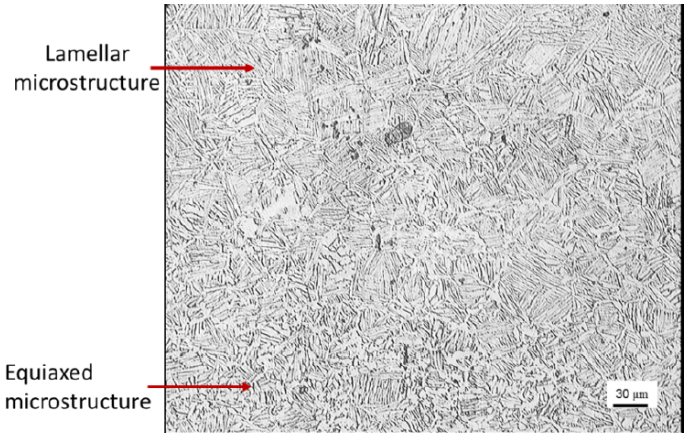

Figure 2.28 The interface between the insert plate and the top section of the "smart part" at 20X magi faction. A change in microstructure may have a change in mechanical properties.

Using the Duramin-A300: Hardness testing system, the micro hardness was tested. The average hardness of the "smart part" was 31.15 HRC, which is similar to annealed Ti-6AI-4V at 34.0 HRC. The hardness was taken along all three parts of the "smart part", bottom section, insert plate, and top section. Every 0.8mm a hardness value was taken and Figure 2.20 provides the hardness values with given distance. Figure 2.2029 below illustrates that there is no larger difference in the hardness as the distance increases.

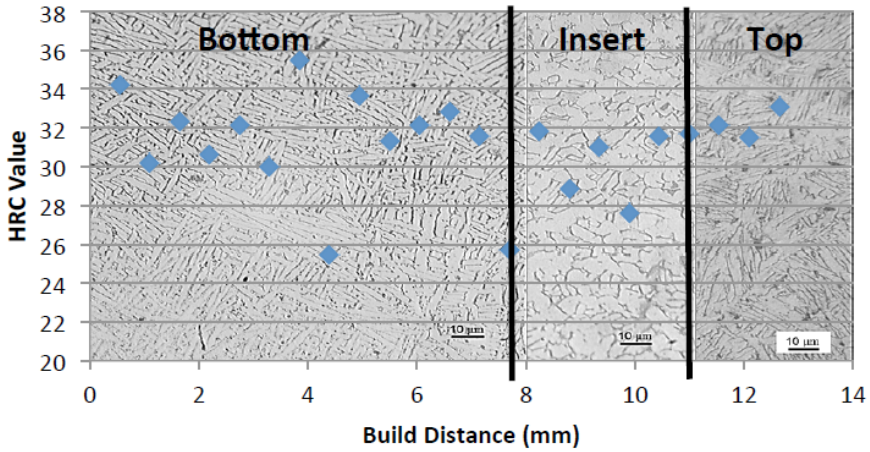

Figure 2.20 HRC value versus build distance

2.12 Improved Design Towards Alleviation of Metallization

An issue has come to our attention that all fabricated smart part prototype is electrically shorted after the second fabrication. We identified the problem comes from the second built where the metal powder vaporized and coated all over the sensor thus leading to shortage. Therefore, a new packaging procedure was adopted in order to avoid metallization of sensor. In doing so, an isolation cap attached to the start plate was introduced. The isolation cap served the purpose of avoiding metal powder insertion in the fabricated parts by avoiding metal powder contact with the bottom part. The isolation cap along with CAD assembly is shown in Figure 2.21. The machining of the start plate was done to have better sealing with isolation cap in order to avoid metal vapor. As a result, the isolation cap assembly can overcome the metallization issue occurring from the bottom or more specifically from the powder bed. The EBM fabrication process includes raking of powder during fabrication to have the desired powder layer. So, a design modification is needed to avoid metallization as well from the powder spreading at the top or during fabrication process.

The design modification involves of preventing the metal powder going into the sensor part. A seating for insert part (shown in Figure) in the cavity has been introduced to prevent the metal powder from going in due to raking of powder. A point noteworthy, the press fitting of the insert part actually prevents the metal powder from going in. The seating of the insert part may also prevent metallization of sensor assembly caused by vaporization of metal powder created in the build chamber.

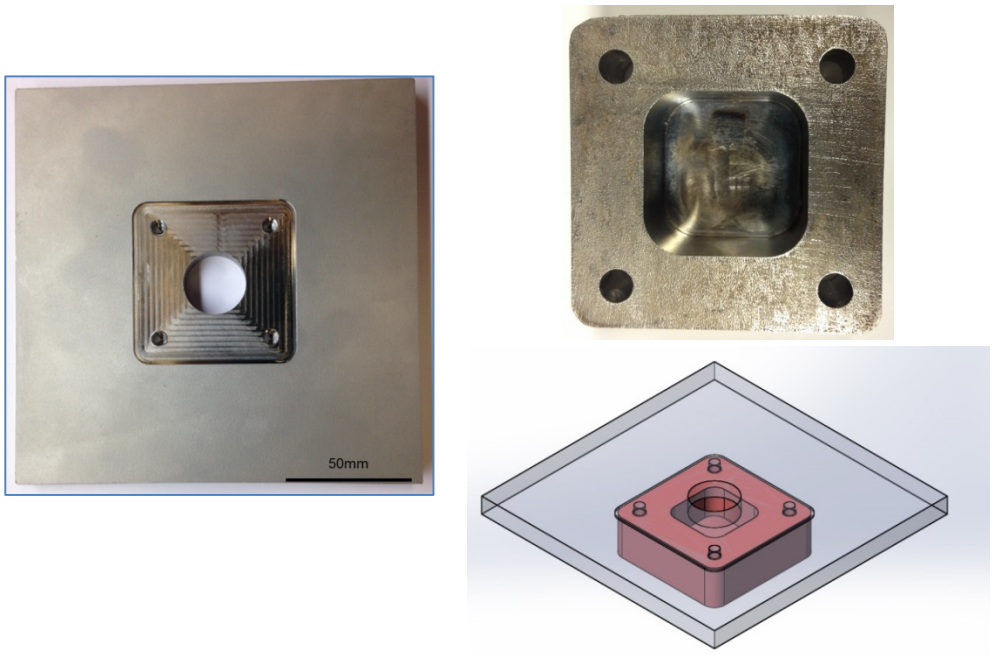

Figure 2.21 Modified fabrication using bottom cap for powder isolation

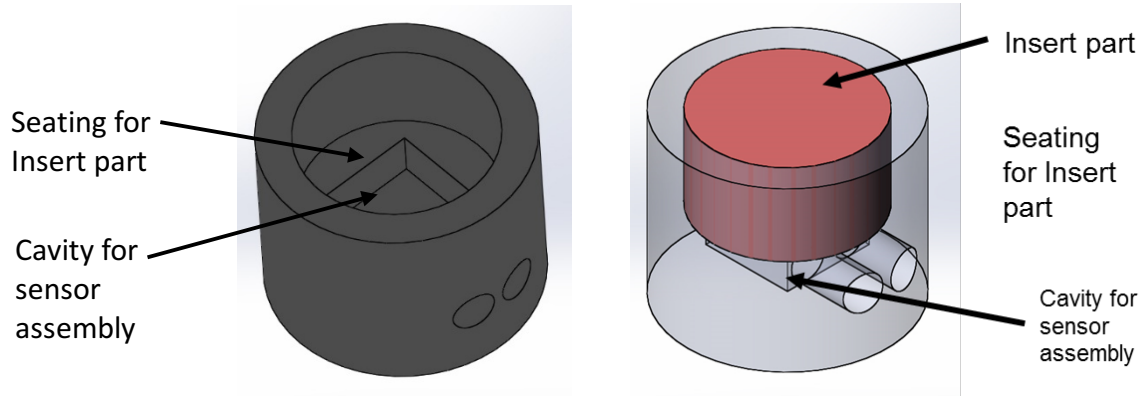

Figure 2.31 Modified design of the fabricated parts.

2.13 Improved Sensor Packaging Design towards Alleviation of Metallization

In order to avoid metallization that caused sensor shortage, alumina housings are being fabricated and implemented inside the smart part for protection. In this quarter, we are using traditional marching method and 3D printing method to fabrication the ceramic sensor housing. ExOne binder jetting technology is one method of fabrication for the alumina housing. ExOne is

a binder-jetting additive manufacturing technology that allows the fabrication of a large range of materials. We developed parameters to build alumina parts using the ExOne process in order to mass-produce the sensor housing for the smart parts. Experiments are being conducted in order to achieve fully dense parts, and shrinkage in the X, Y, and Z direction is also being taking into account of design. The ExOne fabricated parts are being sintered using a tube furnace for 16 hours and compared to the CNC machined alumina parts. CNC machined and ExOne fabricated parts will be used and compared as sensor housing. The sensor housing will be tested for metallization after they have been presented in the second building of the smart parts by the using of SEM and EDS. Figure 2.32 is the image of ExOne machine and an example of the ExOne fabricated alumina housing before sintering.

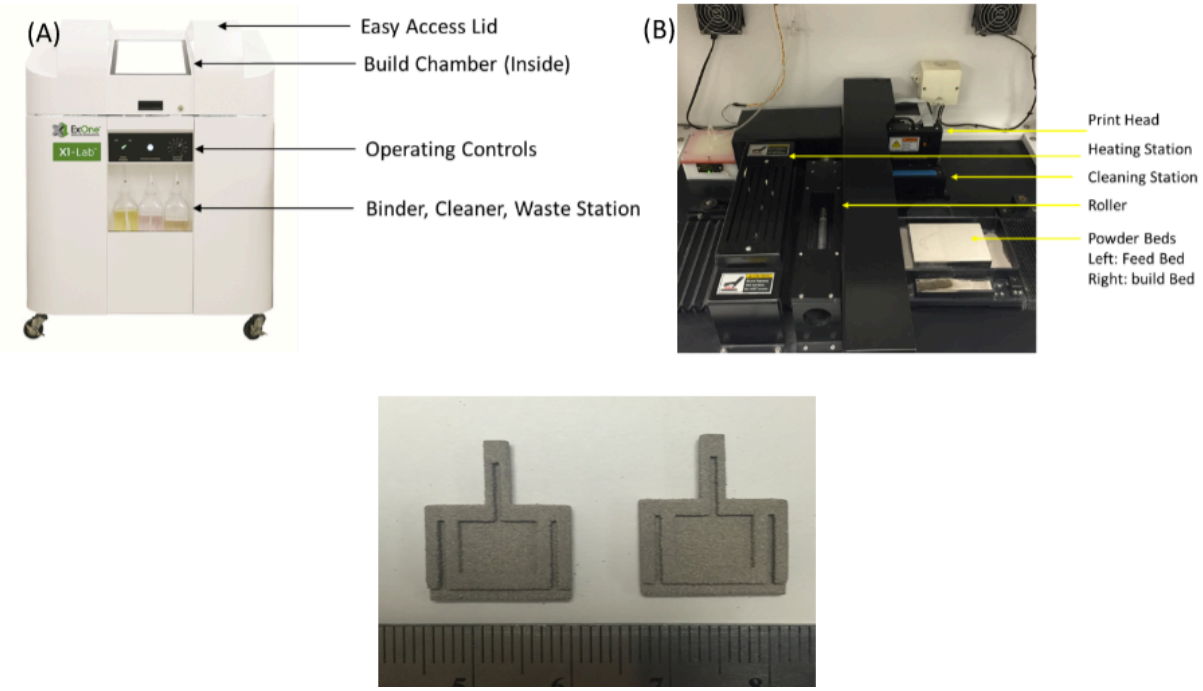

(C)

Figure 2.32: Images of (A) Ex-One outside view, (B) internal view, (C) sensor housing fabricated by binder jetting 3D.

Other than 3D printing, we also used traditional CNC machine with machinable alumina to fabricate the sensor housing. A first simple design for the packaging is presented in Figure 2.33. The piezoelectric and electrodes are positioned in the female part (right) and the package is closed

by press fit the male part (left). The friction in the mating faces will stopped or slowed down the diffusion of metal vapor into the piezoelectric thickness and preventing its shorting across the thickness after the second fabrication. The measurements are shown in Figure 2.33. The "leg" that protects the electrodes ends will be exposed during the second fabrication. They will be cut after the final fabrication for connecting electrical leads for sensing signals. Figure 2.33 shows the detailed dimension of the first design with an image of fabricated sample.

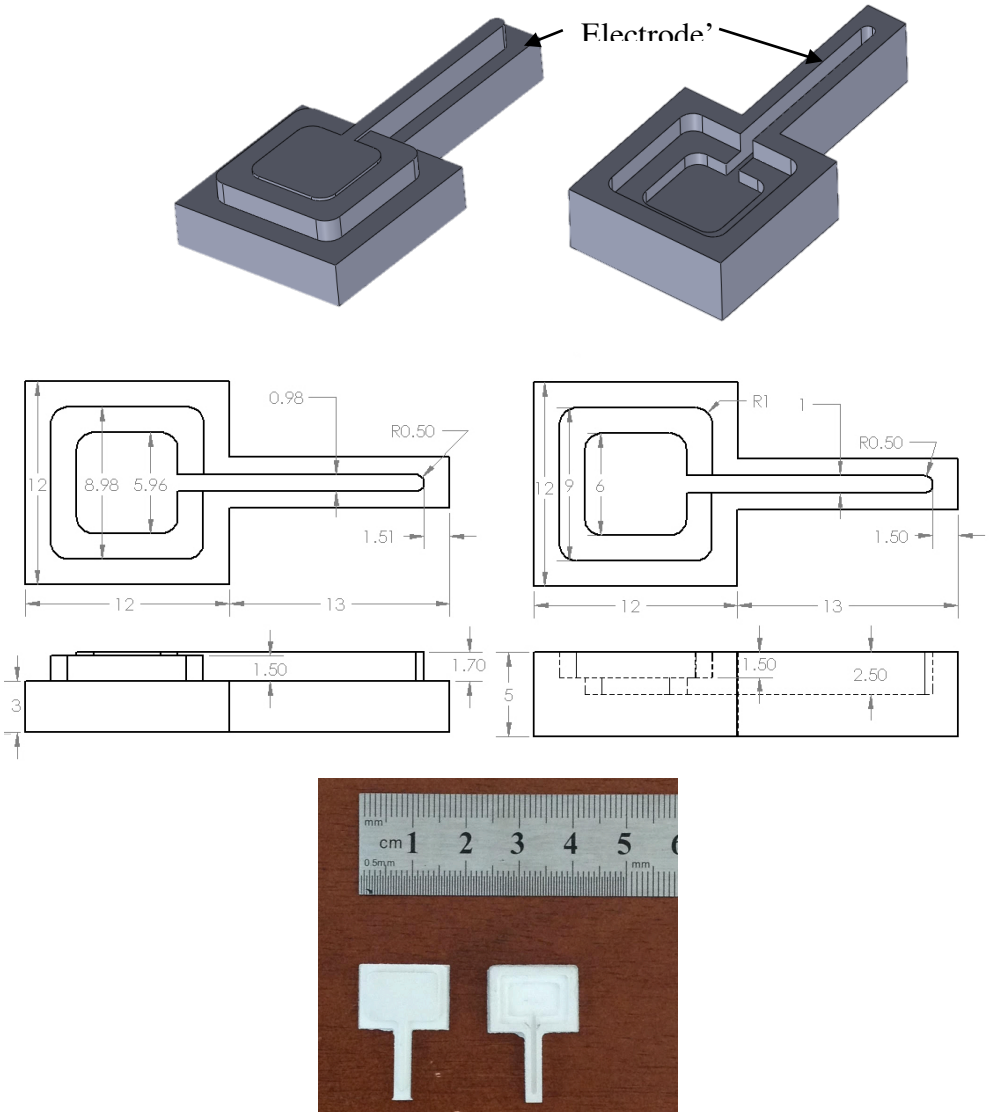

Figure 2.33: Blue prints for Male (left) and female (right) connectors for the simple - friction fit design.

2.14 Smart Part Fabrication using Sensor Housing

The sensor housing was used to protect the sensor from external source of metallization, such as: Ti-6Al-4V Part, and Ti-6Al-4V powder from powder bed. The following 4 types of sensor packaging was explored to fabricate the smart parts: Machinable Alumina, Injection molding Alumina, 3D Printed Alumina, and 3D Printed and Ceramic spray.

Figure 2.34 shows these 4 types sensor packaged parts. The most commonly used was machinable alumina due to its high density, and usability compared to other 3 types. For the sensor housing fabricated by injection molding, binder jetting 3D printing, and ceramic spray did not work out well. Metallization still happened for the sensor housing fabricated by these three methods. Only the sensor housing fabricated by machinable alumina worked out well and stopped metallization.

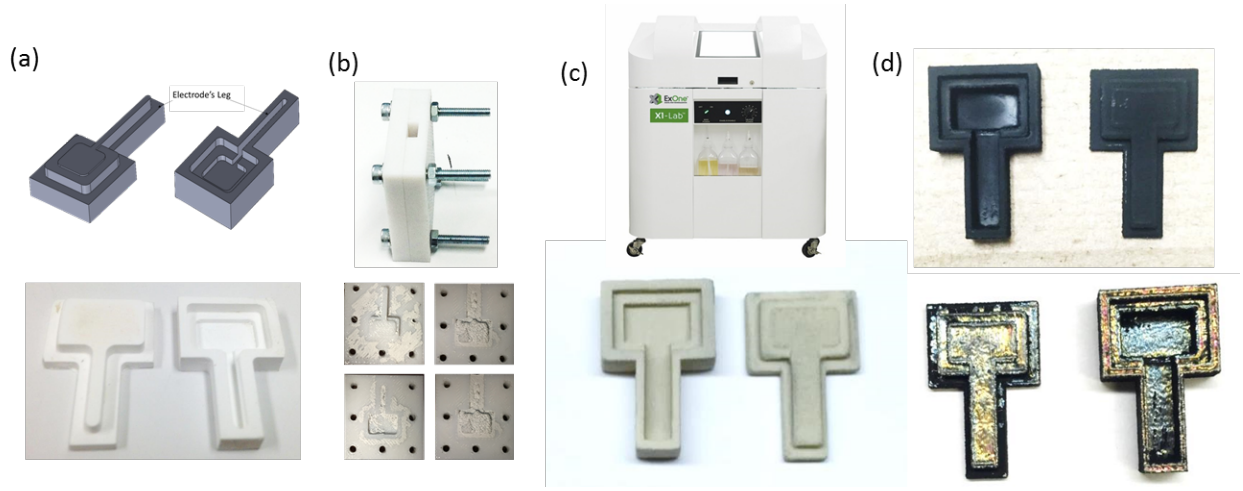

Figure 2.34: Sensor housing, (a) machinable Alumina, (b) injection molded Alumina, (c) 3D printed Alumina, and (d) EBM printed housing coated with ceramic spray

3D Printed Housing

Different methods of fabrication for the sensor housing were attempted in order to created the best possible protection to the piezoelectric sensor. The best process of fabrication was achieved from the machinable alumina machined using a CNC, however due to the eliminations of access to the CNC machine and the total amount of time needed to complete the housing, a decision to develop other methods of fabrication were considered and then compared to the CNC machining process. A good alternative to machining, can be binder-jetting technology, a type of additive manufacturing that uses binder and powder based materials to created complex geometrics components. Using the ExOne M-Lab, a type of binder jetting technology machine present at the

W.M. Keck Center, successful housing were created and sintered. Figure 2.35 shows how the green body part looks like, and how the final product appears after sintering. The sintering profile that was used to increase the furnace at 10°C per minute until furnace reached 1600°C, then sintered at 1600°C for 16 hours. After the parts were successfully sintered, density and shrinkage analysis was performed to be able and compare to the machinable alumina. After several calculations, the apparent percent density of the ExOne fabricated parts was about 96%, and the shrinkage ranged from 8 to 10% in the X, Y, and Z direction. The shrinkage should not be an issue since the CAD file can be altered to account to the shrinkage.

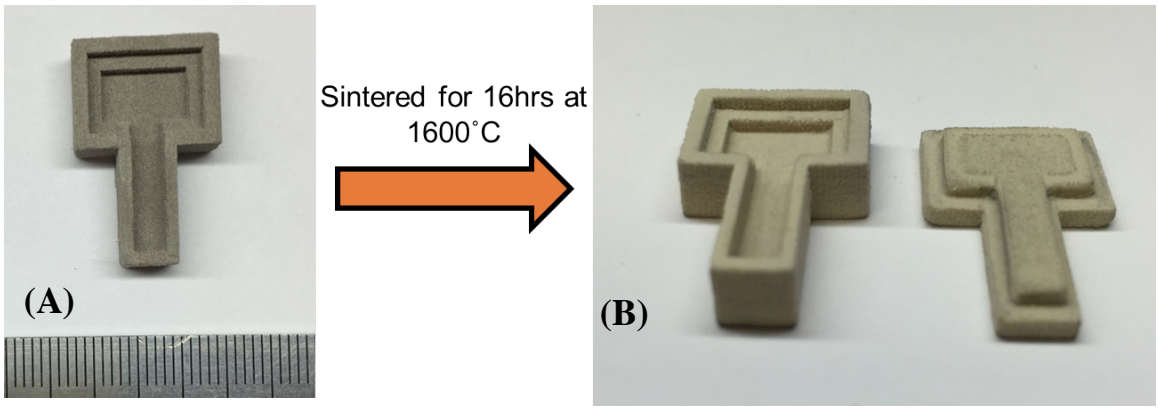

Figure 35: (a) Green body of sensor housing created by the ExOne M-Lab (b) finished sensor housing after sintering of powder.

Mold Injection Housing

The next possible fabrication process that was attempted was mold injection of alumina paste. The molds were printed at the W. K. Keck Center from ABS plastic. The alumina paste that was used was water-based alumina with high viscosity. The paste was carefully applied onto the mold of the female and male parts of the housing, closed, and then place in vacuum furnace to remove the as much amount of the water from the paste. Figure 2.36 shows how the molds appeared once removed from the furnace and opened up. Both molds had the paste stick onto the walls and made removal of housing very difficult without breaking. High amount of bubbles also appeared in the surface of the parts, which may become an issue since it may lead to no protection of metallization to the piezoelectric sensor. Due to the difficultly of achieving well fitting housing, this method was not further pursued.

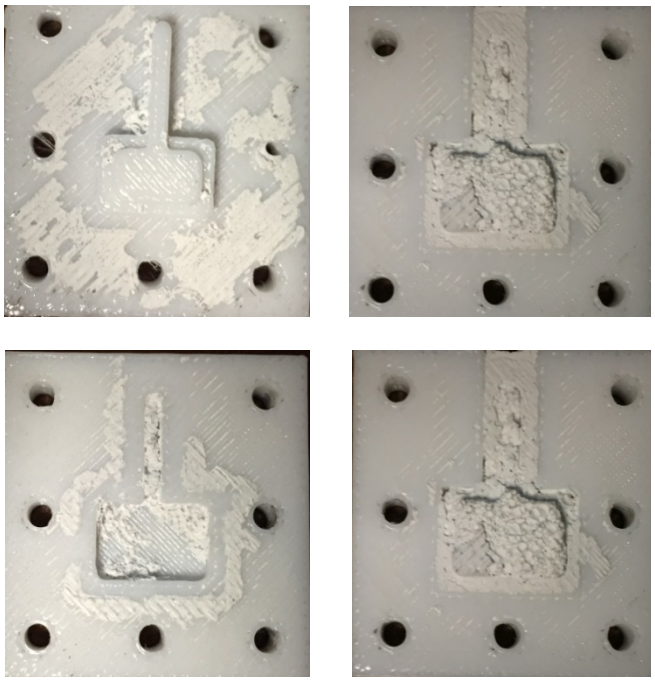

Figure 2.36: Molds of the female and male sensor housing, showing how well deposited and removal was a challenge.

EBM Built Housing

The next possible sensor housing was fabricated was EBM, which is the same process of fabrication that is used to fabricate the smart parts, as shown in Figure 2.37. The housing was made from Ti-6Al-V4, but then coated using a high temperature in order to make the housing not conductive. The high temperature was a silicon oxide, or silica, ceramic that can withstand up to 1200°C. The ceramic coating has a post curing process after application that must be performed in order to achieve high temperature survival. However once the post curing process was done to the housing, the ceramic coating begin to chip of the metal surface which defeated the purpose of the coating. A possible reason that the coating was not bonded to the surface could be due to the difference is coefficient of thermal expansion of the two different materials. Due to non-coating possibilities using a Ti-6Al-4V housing, this process was also not continued.

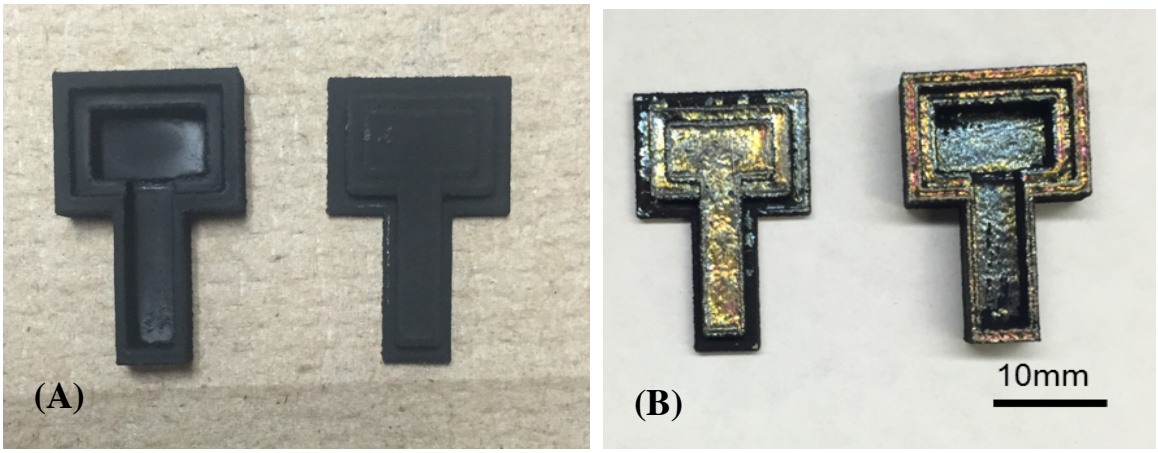

Figure 2.37: (a) EBM fabricated ti-6al-4v sensor housing coated with silica ceramic spray before curing (b) sensor housing after curing process

Machinable Alumina Sensor Housing

Improvement for the fabrication of the alumina for the packaging of the piezoceramic was mainly done on the design shown in Figure 2.38. The fabrication was done in a CNC machine. Different clearances for the package were tried in different runs. In Figure 2.38 a schematic for the CNC fabrication is shown.

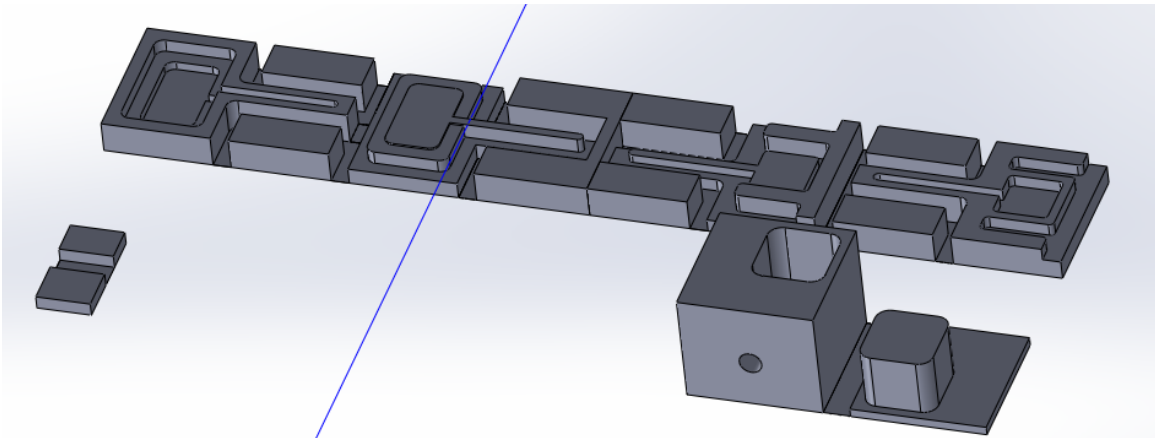

Figure 2.38: A schematic of a sample run for the CNC machining of the alumina package.

The fabrication of the alumina was done in several steps. Practice and experienced were used to improve the method. From the raw material (Alumina block 6''x6''x0.5''), cuts are done to approximate the final shape of alumina. This is done by a tile cutter design for ceramics and

composites. The slabs are attached to an aluminum plate that will work as a base during the machining process. The adhesive used is a commercial cyanoacrylate adhesive. A milling machine is used to obtain he final dimensions required by the CNC fabrication. This process is done by steps of 0.01 mm in all directions using carbide square end mills of 4 flutes. This process can be lengthy depending on the total number of pairs that will be machined in the CNC process. For a single pair, of the design shown in Figure 2.39, it took about one hour.

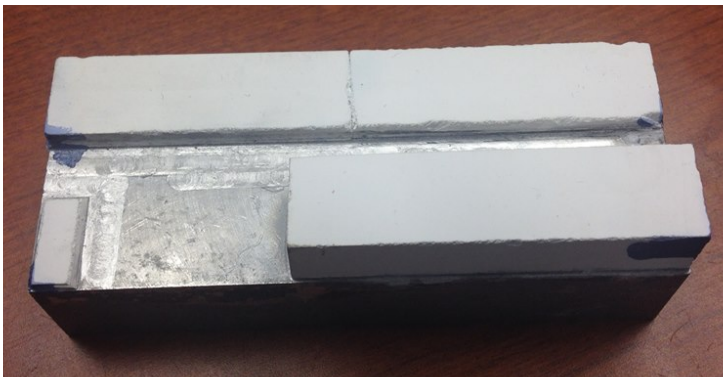

Figure 2.39: Preparation of machinable alumina for the CNC fabrication.

2.15 Smart Part Dynamic Force Sensing

A compression-compression test was performed in order to evaluate the force sensing capability of the smart part. A MTS Landmark servohydraulic test system (Eden Prairie, MN) was used to perform the compression-compression testing. The smart part was compressed at about 0.25 mm, which was referred as the test's initial position. Then, the part was oscillated at ±0.1 mm from the initial position at the frequency of 10 Hz, 15 Hz, 20 Hz, and 25 Hz. A DAQ system (NI PCI-6221) was used to record the voltage response. Figure 2.40 shows the test set up of smart parts force sensing. A flat cylindrical fixture was used for the compression-compression testing. A load concentrator was used to ensure the load was being applied at the center of the smart parts. The electrodes were connected with the DAQ system using a clamp to record the voltage response (V). Four different frequencies (10 Hz, 15 Hz, 20 Hz, and 25 Hz) were used to demonstrate the sensing capability across various dynamic loadings. Figure 2.41 shows the piezoelectric voltage response under these frequencies corresponding to the applied force (F).

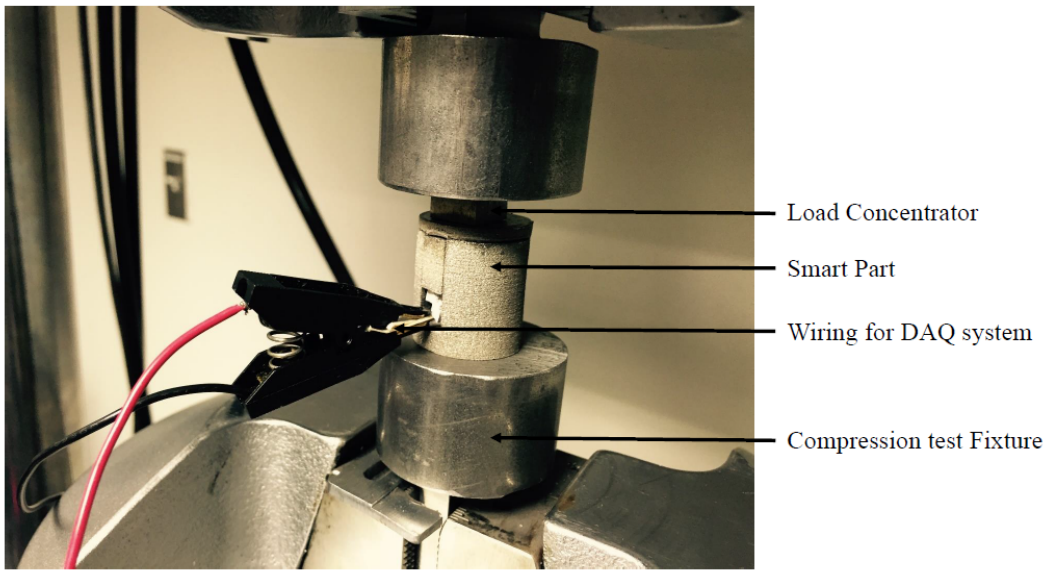

Figure 2.40. Compression - compression force sensing set up

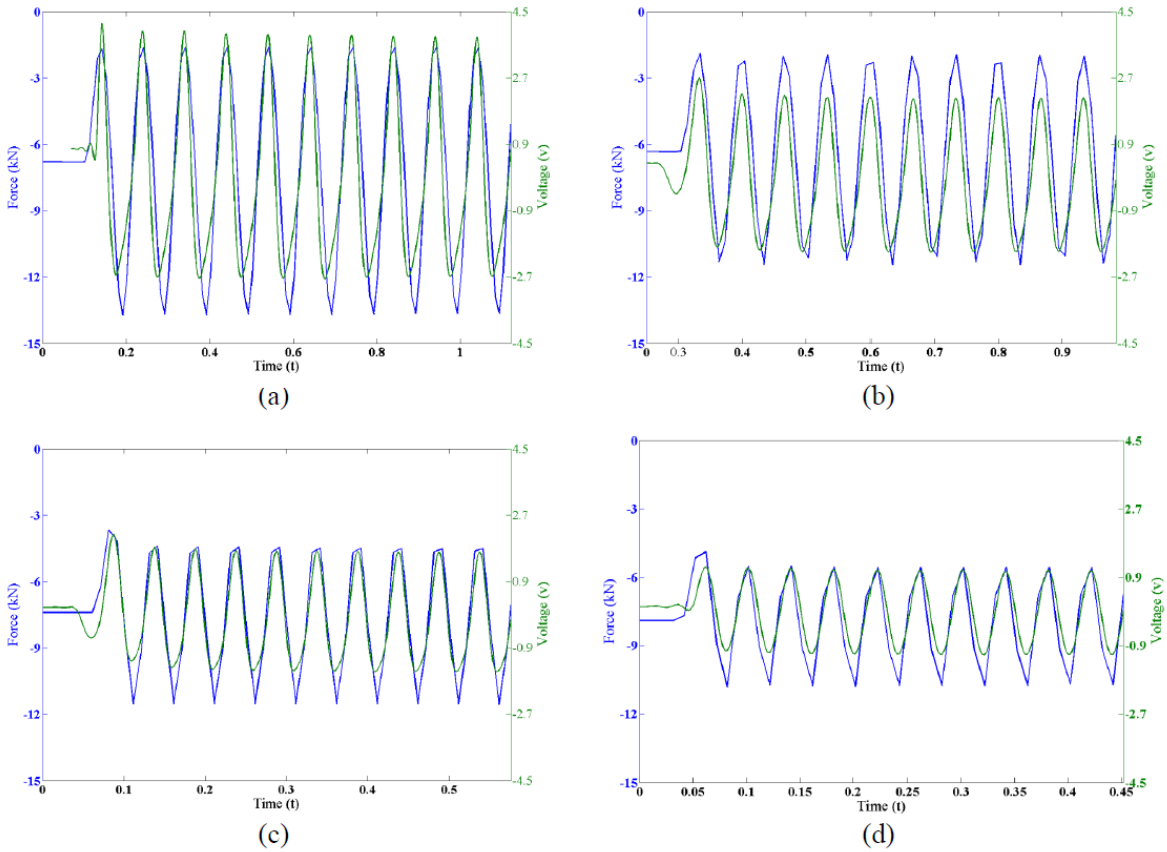

Figure 2.41. Voltage response obtained from Smart part in accordance of the compressive applied force. The voltage response was obtained at frequencies of (a) 10 Hz, (b) 15 Hz, (c) 20 Hz, and (d) 25 Hz

The sensitivity between voltage and force at these four frequencies was calculated and shown in Figure 2.42. The sensitivity result provides a comparison to characterize the integrity of the piezoelectric within the smart part. The sensitivity of a cycle was defined as the ratio of the range of the voltage by the range of the force. The overall sensitivity is the average using all the cycles during the test. The following equation summarizes the concept:

$$\text{Voltage-Force Ratio (V/kN)} = \frac{\sum_{i=1}^{N} \frac{(V_{max,i} - V_{min,i})}{(F_{max,i} - F_{min,i})}}{N}$$

where N is the total number of cycles applied during the compression-compression test and i is the cycle number.

The average sensitivities were 0.53, 0.43, 0.44, and 0.42 (V/kN) for the four frequencies 10 Hz, 15 Hz, 20 Hz, and 25 Hz, respectively. The result showed a decreasing trend in sensitivity with an increase in frequency except for the sensitivity response at 15 Hz. The DAQ sampling rate in the compression test was 99.9 Hz that ultimately decreases the data point in each cycle with the increase of frequency. That can affect the data sets reflecting the true maximum and minimum force response obtained at high frequencies. Besides, at higher frequency, the dipole movement in the piezoelectric sensor falls behind the frequency of applied dynamic loading, which could further lower the sensitivity. Nevertheless, all sensing voltage across different frequencies showed good agreement with the frequencies of the applied force, indicating force / pressure sensing capability of the fabricated smart part. As the part's dimensions and fabrication process can cause the damping of the sensor signal, a calibration method can be developed to evaluate the smart part's operation in practical engineering applications.

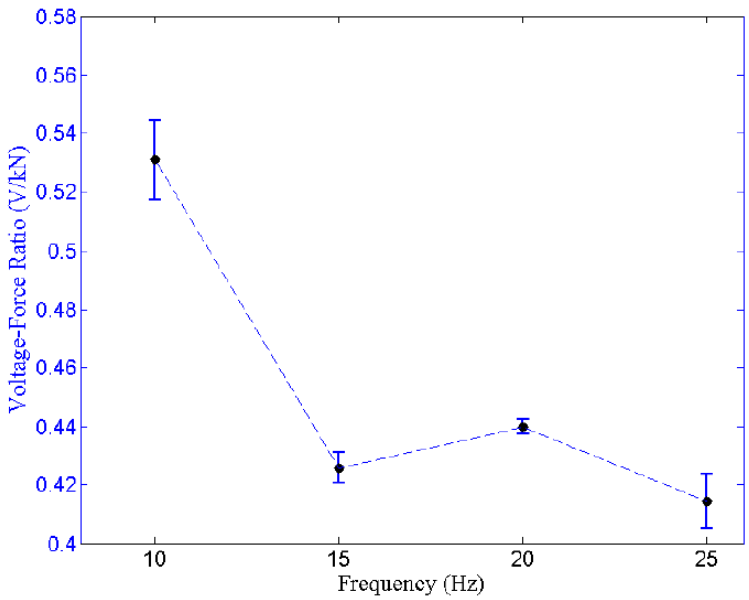

Figure 2.42. Sensitivity response obtained at four different frequencies 10 Hz, 15 Hz, 20 Hz, and 25 Hz. Each point represents the average sensitivity response of all the cycles at different frequencies with 95% confidence interval bars.

CHAPTER 3 SMART TUBE FABRICAITON

3.1 Smart Tube Fabrication Process

A smart pressure tube was fabricated using stop and go process using a mask plate. A stainless steel (SS) mask plate was machined using a CNC Mini Mill 2 (HAAS Automatic Inc., USA). The mask plate was used to hold the sample in the powder bed. Figure 3.1 shows the mask plate for smart tube.

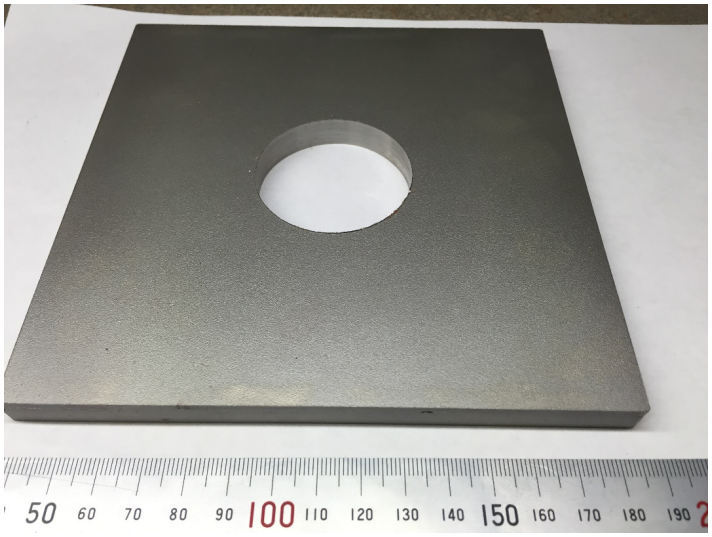

Figure 3.1: Mask plate for smart tube.

The bottom section, insert part for the sensor cavity, and middle insert part was fabricated using electron beam melting (EBM) machine. The parts were make sure to press fit in the component. Figure 3.2 shows the components of smart tube. The insert part for the sensor cavity was to make sure the attachment of the sensor in the cavity and a planar surface for the 2nd build. The middle section was serving as a planar surface to continue the 2nd build. After fabrication, the middle insert part was removed from the smart tube.

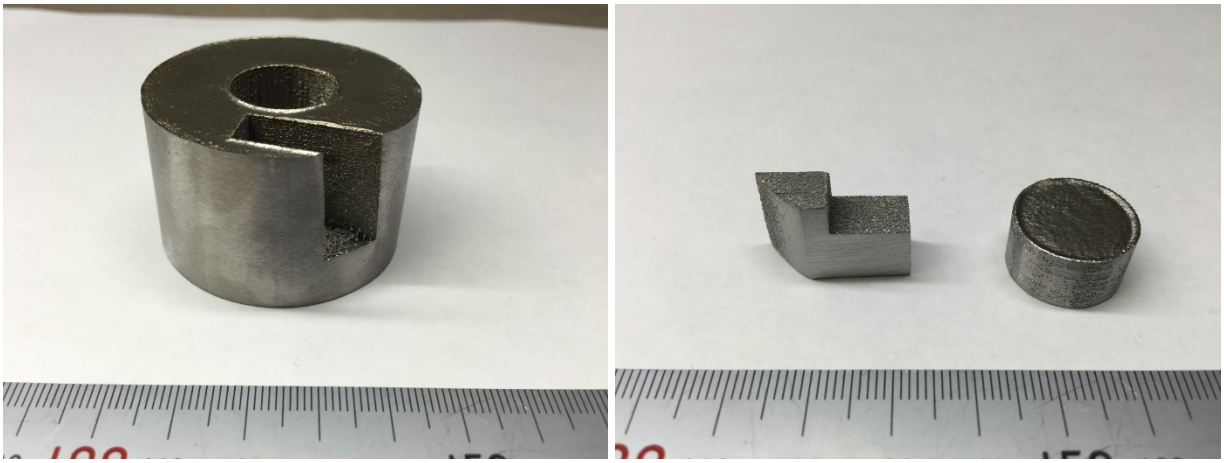

(a) (b)

Figure 3.2. Components of smart pressure tube, (a) bottom section of smart tube and (b) insert part for sensor cavity and middle insert part.

The sensor packaging consists of PZT material and tungsten electrode encapsulated in the sensor housing. The similar sensor housing that of used in the cylindrical shaped smart parts was used in the pressure tube. That way, any dimensional changes were avoided in the smart tube. Figure 3.3 (a) shows the assembled smart tube ready for the 2nd fabrication and Figure 3.3 (b) shows the first trail of the fabricated smart tube.

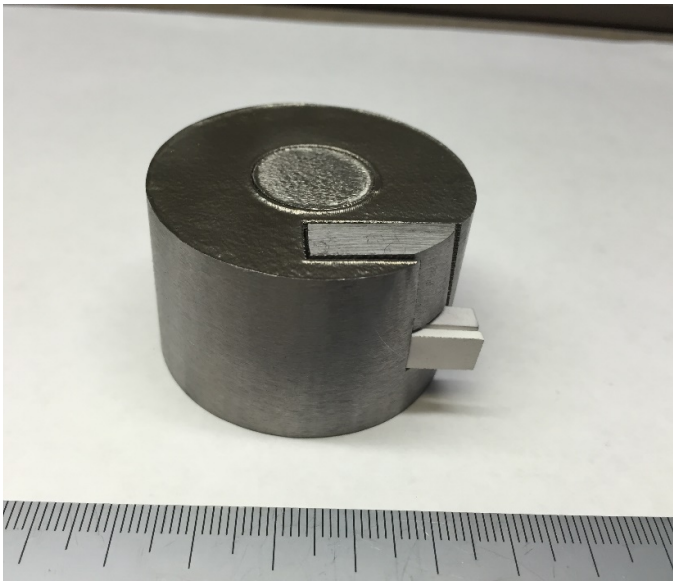

(a)

(b)

Figure 3.3. Smart tube (a) assembled part and (b) complete part.

3.2 Smart Tube Force Testing

As mentioned in our previous report, we fabricated the "Smart Tube" using the stop and go process. In this quarter, we did initial sensing demonstration by applying dynamic force on them. However, the response is very weak and some modification on fabrication and post processing is on going. First of all, we designed and fabricated a pair of fixtures to apply dynamic loading on the pressure tube. The fixture of test tube was designed to accommodate the stress to the radial direction of the local position of the piezoceramic of the test tube. The material used to fabricate the fixture was steel and aluminum (see Figure 3.22 for CAD of the fixture).

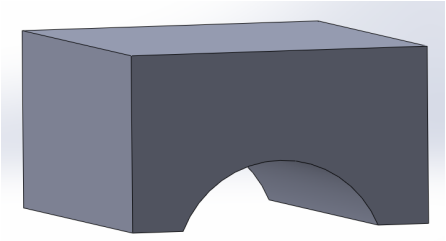

Figure **3.**22: Fixture model used for testing of the test tube.

The response of the smart test tube is shown in Figure 3.23. The response is low compared to smart cylinder we reported in previous quarterly reports, and an offset of the average voltage occurred during the testing. The response will be further investigated by testing under different conditions, and other aspects are being analyzed such as predicting the voltage response using finite element modeling, fabrication process and improved poling conditions in order to achieve similar response as smart cylinder prototypes.

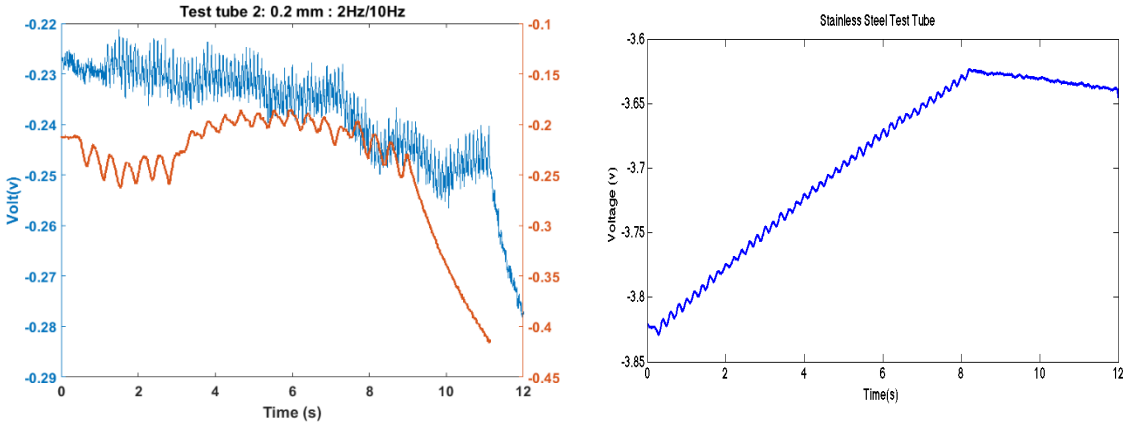

Figure 3.23: Response of test tube #2 with aluminum (left) fixture at 2 hz (red) and 10 hz (blue) and steel (right) fixture (5hz).

3.3 Smart Tube Temperature Sensing Test

Sensing capabilities of test tube were studied considering the pyroelectric properties of the PZT. The pyroelectric effect is responsible of generating current under changes in temperature over time across the sample. To study this property, the test tube was exposed to a temperature of 90 °C in a furnace. The generated current was measured by a picoammeter connected to the electrodes. After minutes of exposure, the door of the furnace was opened, and a cold compress was used to force the cooling of the test tube.

Generated currewnt (I) through a homogenous pyroelectric material with temperature T at any time (t) is presented in Eq. (1):

$$I = \frac{dQ}{dt} = pA\frac{dT}{dt} \qquad (1)$$

In Eq. (1), Q is generated charge due to temperature change, p is pyroelectric coefficient of the material, A is the surface area of the electrode and $\frac{dT}{dt}$ is the rate of temperature change of the material with respect to time. Eq. (1) can be rewrite into following to calculate the temperature of pyroelectric material at any time with considering the initial temperature as room temperature.

$$T_f = \frac{1}{pA}\int_{t_i}^{t_f} I dt + T_i \qquad (2)$$

Here, T_i is the initial temperature of the pyroelectric ceramic material at time t_i, which is considered as room temperature and T_f is final temperature of the material at any time t_f. By measuring the room temperature (T_i), pyroelectric coefficient (p), electrode area (A), and the total amount of current (I) generated by the material with a certain period of time (t_i to t_f), the final temperature (T_f) can be calculated at any time (t_f). For our samples, the contact area of the PZT was less than 39 mm2. The pyroelectric coefficient reported from the company Piezo.com was 400 μC/ m2°C.

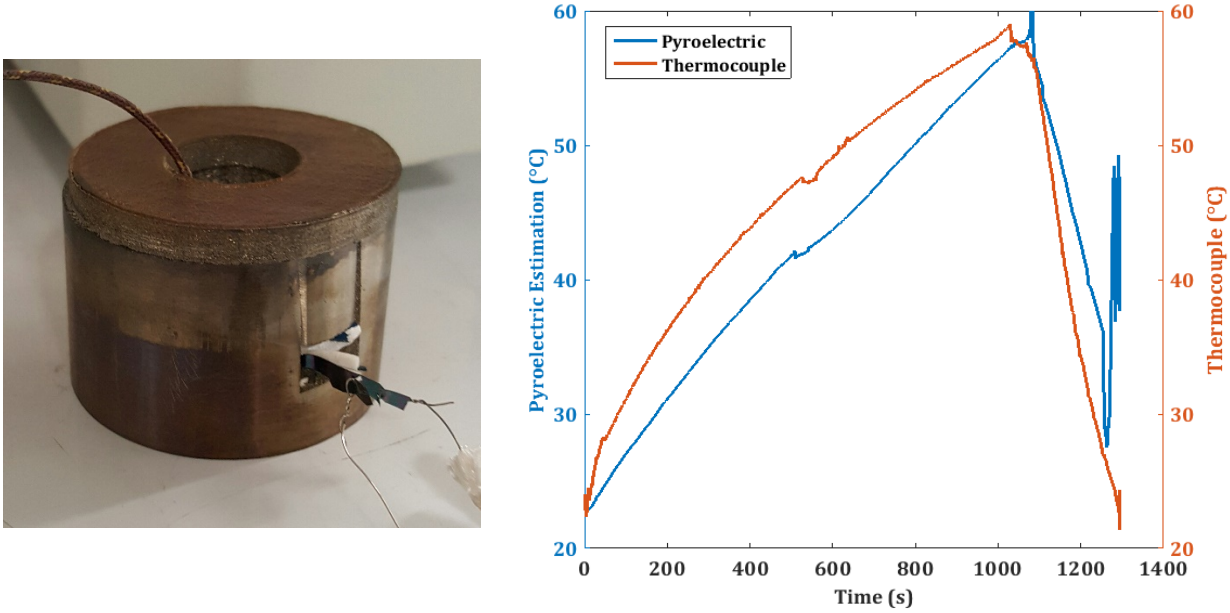

Figure 3.6: Test tube set up for pyroelectric testing. A surface thermocouple and high temperature wiring is atrtached to a picoammeter (left). Using eq. 1, the temperature was back calculated from the current (right).

An agreement during heating and cooling verifies the sensing capabilities of the test tube. However, the determination of contact area and pyroelectric effect is critical to the correct sizing of the signal. After the high temperature measurement of the dielectric, and electrical properties of the test tube, a repoling of the piezoelectric was done using an electric field of 1kV/mm under 120 ºC during 30 min. A dynamic testing procedure was followed, as previously done, using a DAQ to record the voltage, and a load frame to control the dynamic loading. Results were similar than the reported in the last period.

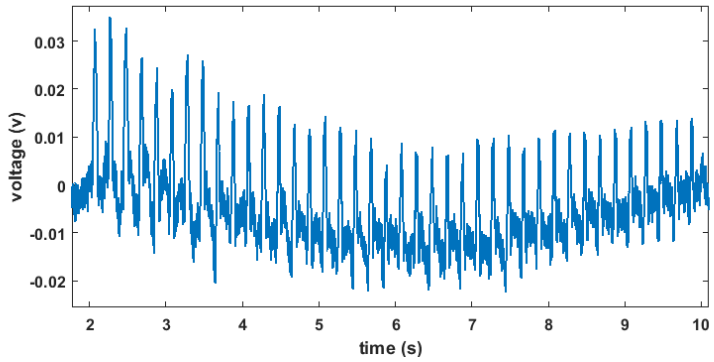

Figure **3.7**: Dynamic loading. Sample re-poled using 1kV/mm, 100°C, and 30 min. Dynamic loading of frequency 5Hz.

The testing showed an amplitude of 40 mV. These results are comparable with previous experiments ranging between 10-50 mV, but lower than the cylindrical counterpart.

A quasi-static simulation was performed to study different configurations of dynamic loadings to maximize the output voltage, or to mimic the radial stress loading that the test tube will be exposed during operation. A set of simulation was done exploring the following changes:

a) Changing the rotation of the piezoelectric with respect to the tube axis.

   A simulation in Abaqus Standard using piezoelectric properties of PZT-5A was done changing the orientation of the piezoelectric to observe the maximum output voltage.

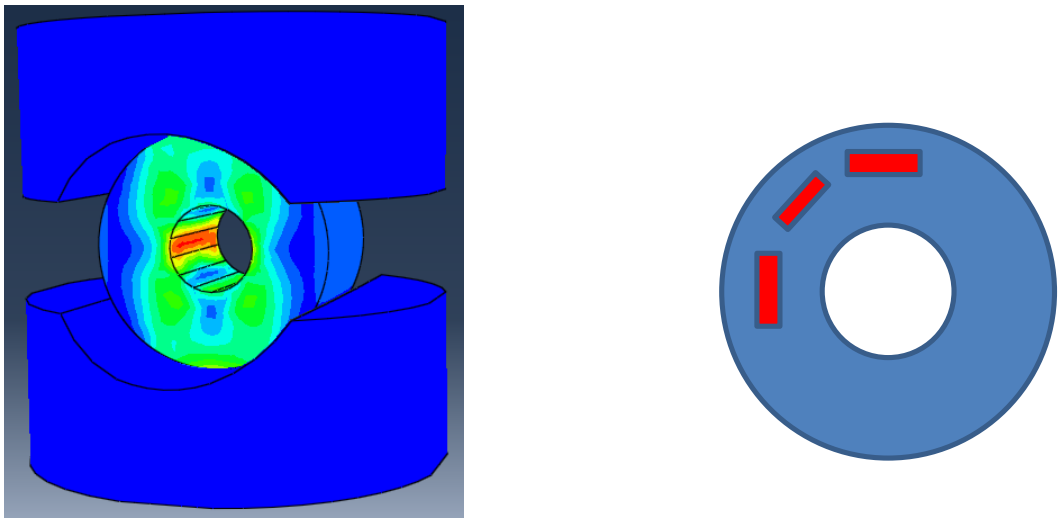

Figure 3.8: Test Tube simulation (Left). Orientation of 0, 45, and 90 degrees (right).

The simulation showed agreement with the experimental results. The voltage was less than 60 mV for the zero degree orientation.

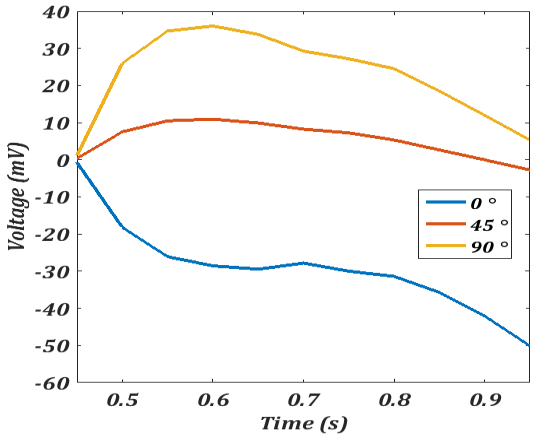

Figure 3.9: Voltage output for different orientation of the test tube.

The configuration for the dynamic loading, showed lower voltage output under these conditions.

b) Temporarily filled the hole of the tube to increase the pressure across the load cells of the Instron machine.

A variation of the simulation was done by filling the hole with a Ti64 tube. An improvement of 10% with respect to previous simulation was found. The response is lower in comparison with the cylinder model reported previously.

3.4 Smart Tube Temperature Sensing Test with Varying Heating Condition

For this study, we use two different heat guns, one with electronic temperature controller and other with only two settings; heating and room temperature.

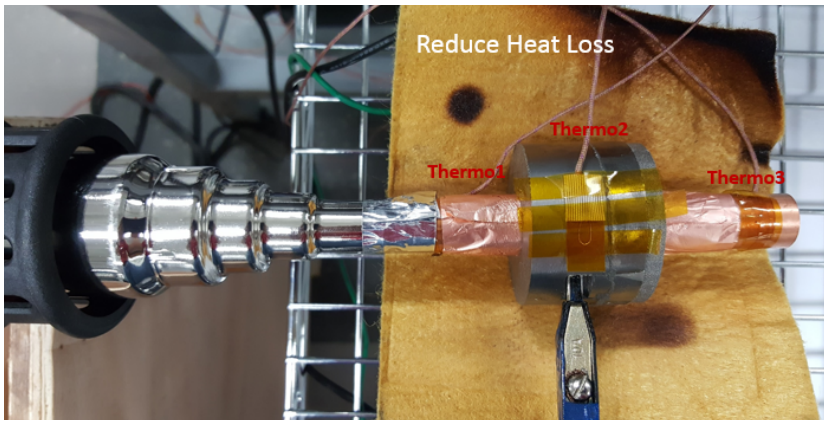

Figure ***3.10***. Experimental setup of temperature variation using heat gun with temperature electronic controller.

The results from this heat gun showed an unexpected sensitivity to electromagnetic fields that caused interference on the current reading. This noise can be seen clearly in Figure 24.11.

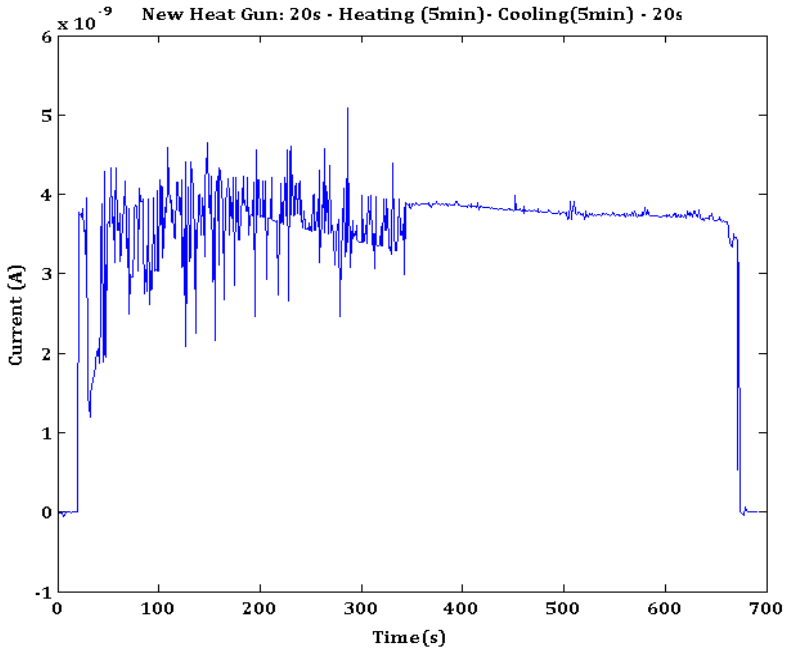

Figure 24**.11**. Current reading using the heat gun with electronic temperature controller. The red circle indicates the cooling section. During heating, no distinguishable trend can be observed due to interference of electromagnetic fields.

An alternative to test temperature variation on the test tube was to use a conventional heat gun with only two settings: high temperature and low temperature (room temperature). The experimental setup is the same, but the temperature variation is obtained by changing the length of the cooper tube that transport the heat to the test tube.

Figure 3.12: copper tube extensions to test temperature variation on the test tube. Three settings were tested: 3 in, 6 in, and 12 in.

Figure 3.13: Experimental setup using heat gun with two settings. Extension is changed to obtain temperature variation.

The temperature of air entering the test tube is shown in Figure (left). The variation is achieved by increasing the heat loss using larger lengths of cooper tube. The temperature on the surface of the test tube is shown in Figure (right) and this temperature is comparable to that registered using the current generated by the temperature change (pyroelectric effect). The analysis includes the trend using the dT/dt of the temperature of the surface and the current generated is shown in Figure . By integrating the current using Eq. 2, we can use the current as real time sensing device (Figure).

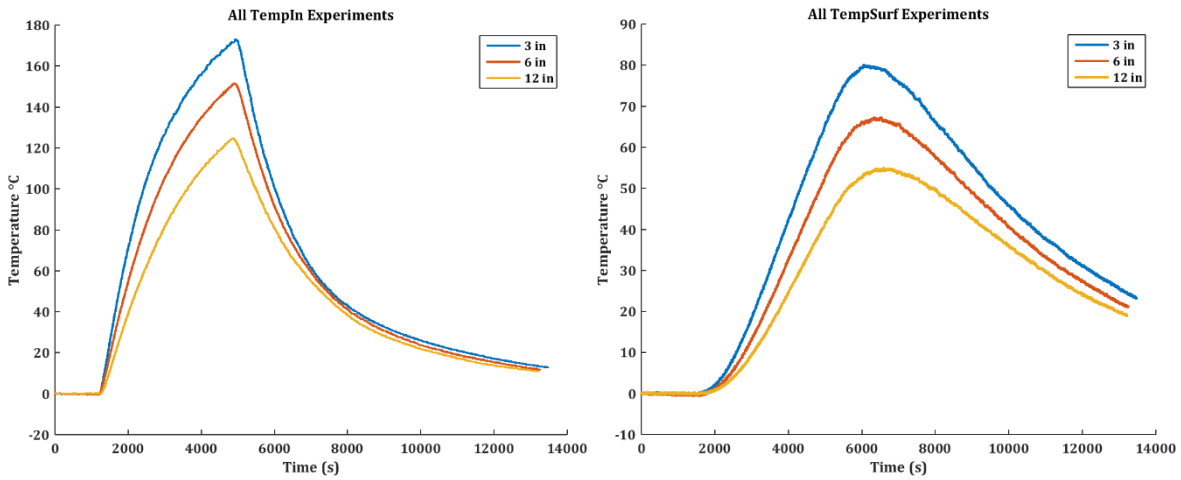

Figure *3.14*: Temperature entering (left) the test tube, and temperature measured at the surface of the test tube (right).

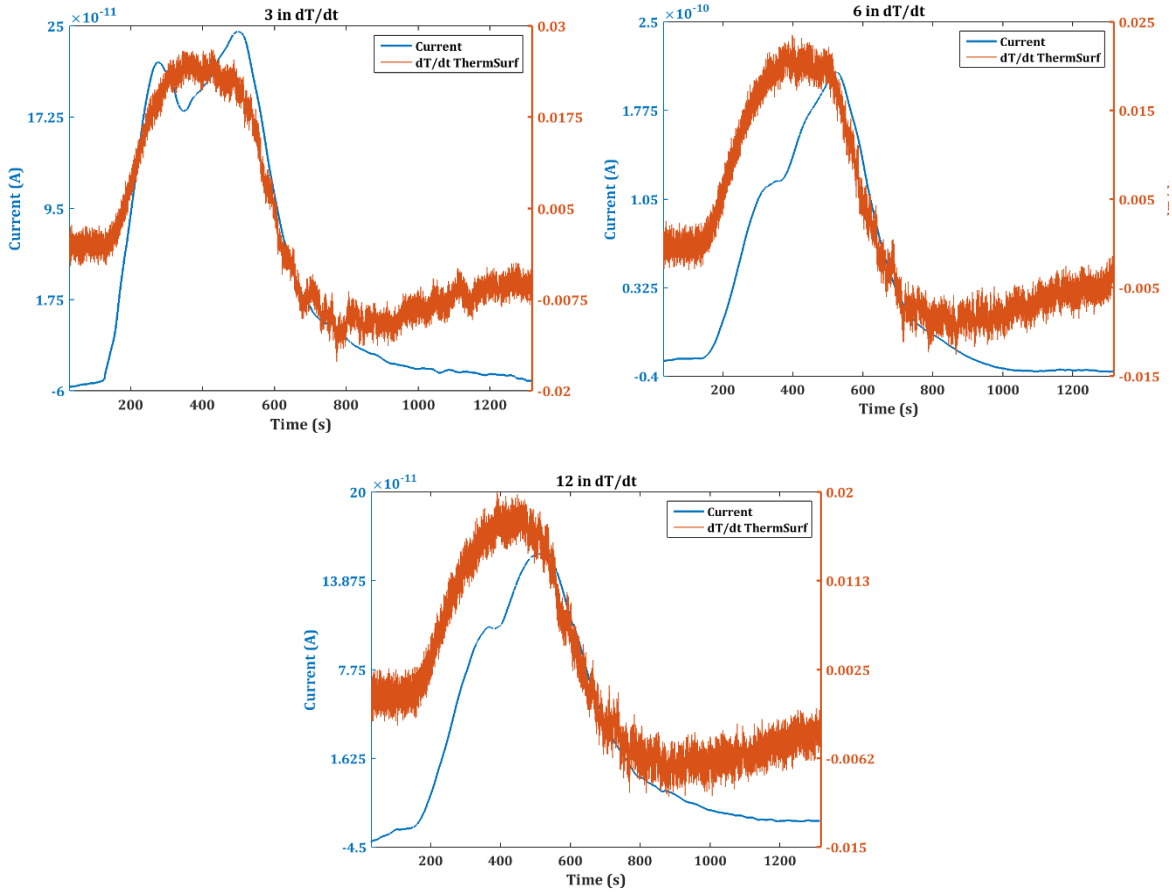

Figure 3.15: Comparison between dt/dt of the surface temperature and the generated current at different copper tube extensions.

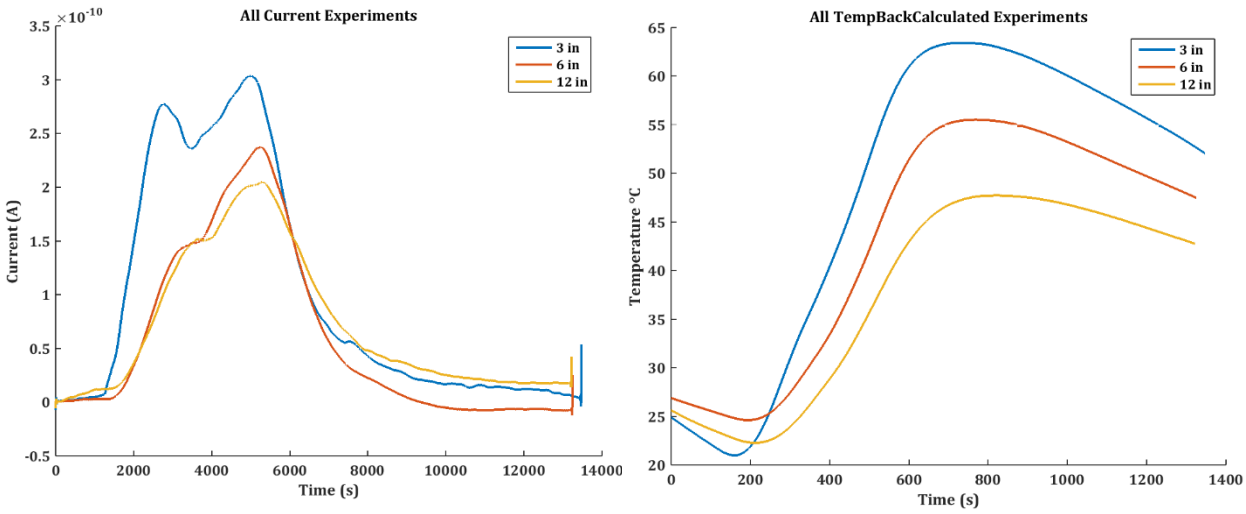

Figure 3.16: Current variation (left) and back calculated temperature using the pyroelectric coefficient and contact area (right).

The variation of the current observed in Figure , in particular the bump during the heating stage, can be explained due to the existence of first-order ferroelectric phase transitions that occur in this temperature range. It has been proven that tetragonal, rhombohedral and monoclinic symmetries exist in the ferroelectric phase of PZT in these temperature regimes, causing a piezoelectric and pyroelectric variation in the current response. Other explanations may reside in internal geometrical adjustments during the heating expansion of the PZT, changing during the experiment the contact area that directly affects the amount of current that is recorded.

CHAPTER 4 ADVANCED STOP AND GO FABRICATION PROCESS

4.1 Smart Part Fabrication without Mask Plate

The conventional method that has been used in this project requires a mask plate. The mask plate serves the purpose of holding the bottom part in the build chamber, and maintains a planar surface for the second build. The mask plate has some drawbacks as it requires some CNC machining beforehand. The CNC machining needs to be tight fit with the fabricated part. The energy system components that contain complex shape geometry such as: swirler, air fuel pre-mixer, etc. may difficult to machine at the position of the bottom section. Another issue is that as the part is being moved to insert the mask plate, the 2nd fabrication needs the exact position to overcome the registration issue, as shown in Figure 4.1.

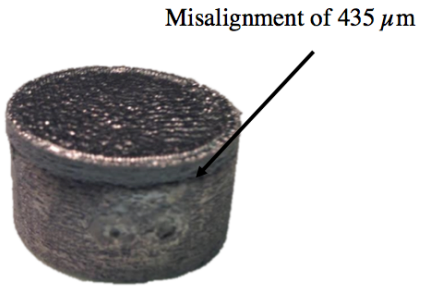

Figure 4.1: Registration issue associated with 2nd built of "Smart Parts".

The fabrication of 2nd build without mask plate helps by reducing the CNC machining work and time. Figure 2 shows the fabrication process without using the mask plate. First, the bottom part will be fabricated in the powder bed of electron beam melting machine. Then, a manual cleaning might be required to insert the sensor housing, and on top of that top part or 2nd build will be fabricated, as schematically shown in Figure 4.2.

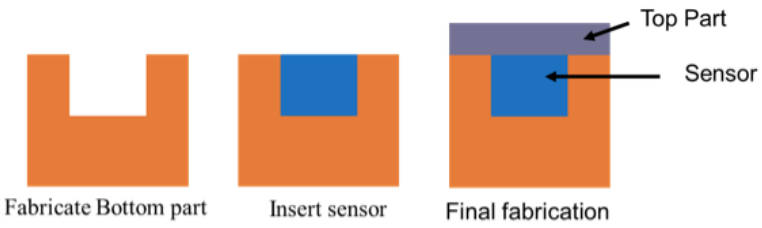

Figure 4.2: Fabrication scheme of smart parts without masking plate.

As a proof of concept, cylindrical shape object was fabricated using no mask plate, as shown in Figure 4.3. The fabrication modification was able to build the part without causing any powder explosion in the EBM machine. The next attempt will be to fabricate the cylindrical shape smart parts using this method. We mainly tuned the EBM parameters such as intensity and raster speed to achieve the "stop and go" process. Therefore, after placing the sensor, the temperature of the starting plate should be increased to withhold the inter layer strength. We have designed a heating unit that will increase the temperature of the start plate. Ten cartage heaters will be inserted into previously made holes of the newly designed start plate.

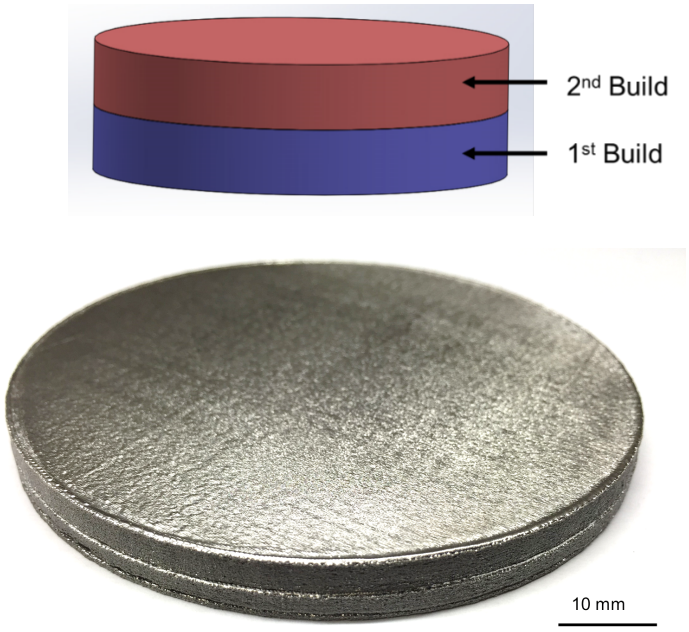

Figure 4.3: Cylindrical shape part fabricated without using mask plate

4.2 Modification of Fabrication Parameters

In our previous study, the interface between first and second build is the weakest and caused material failure at lower ultimate strain. Therefore, in this quarter, we investigated the modification of 3D printing parameters aiming to enhance the interface properties. The interface of the bonded area in stop and go process is important for smart parts applications. Tensile test was performed for characterizing the interface of the fabricated parts. The tensile test was performed according to ASTM E8 standard using a MTS Landmark servohydraulic test system

(MTS, Eden Prairie, MN). A straining rate of 0.005 mm/mm/min was used in this experiment. At the initial stage, the stop and go process was compared with vertical build parts for both as fabricated and machined. Four different types of specimens were fabricated according to following:

1. Vertical build as fabricated specimens
2. Vertical build machined specimens
3. Stop and go as fabricated specimens
4. Stop and go machined specimens

Ultimate tensile strength (UTS), Young's modulus, and tensile strain were obtained from tensile tests for all those 4 types of specimens. From each category, 3 specimens were tested. The machined samples showed comparably higher UTS and tensile strain for both vertical, and stop and go process fabricated specimens. The machined specimens overcomes typical rough surface obtained by the electron beam melting (EBM) technology that would reduce any crack initiation zone from the fabrication aspect. Figure 4.4 shows the UTS result obtained from the 4 types of specimens. The highest average UTS of 1.07 GPa was obtained for vertical build machined specimens. The specimen fabricated using stop and go process failed at the interface which indicates a weak bonding. The average highest UTS obtained using stop and go machined specimen was obtained around 600 MPa, only about half of those vertically built machined samples.

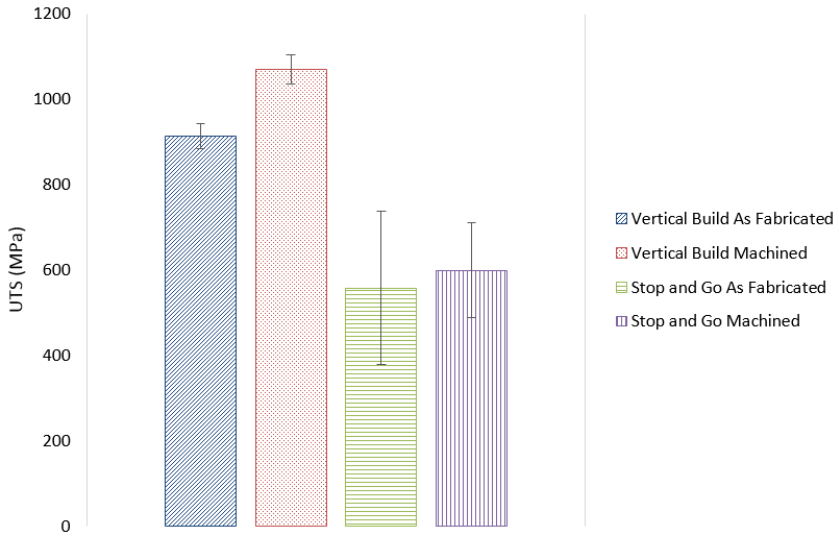

Figure 4.4. Ultimate tensile strength (UTS) result with standard deviation.

Figure 4.5 shows Young's modulus results of vertical build, and stop and go process. The highest average Young's modulus achieved was 131 GPa. The stop and go process yielded similar results of Young's modulus when comparing to vertical build results for as fabricated and machined specimens, respectively.

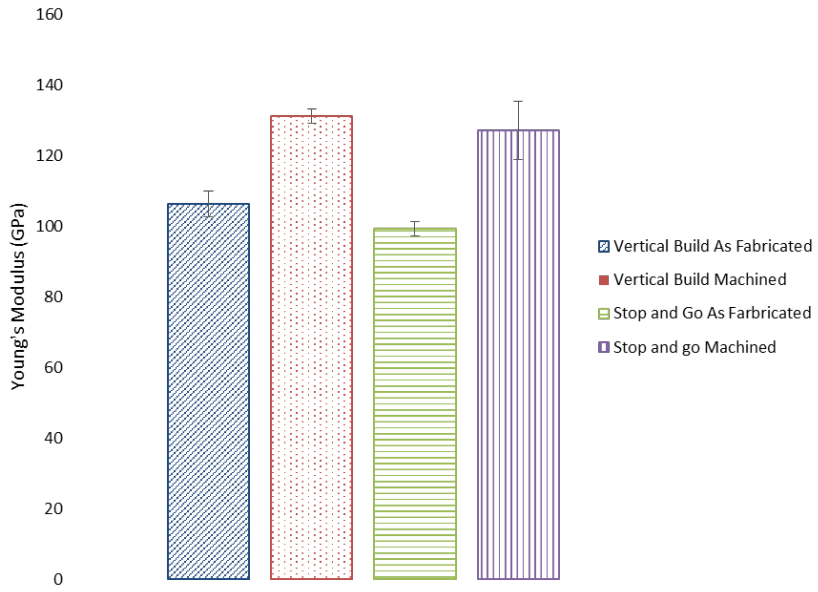

Figure 4.5: Young's modulus result. The error bar shows the +/- standard deviation

Figure 4.6 shows tensile strain results for the 4 different types of samples. The highest average tensile strain was 2.38% for vertical build machined specimen. As the specimens fabricated using stop and go process broke at the interface, it showed little plastic deformation before failure thus yielded low tensile strain.

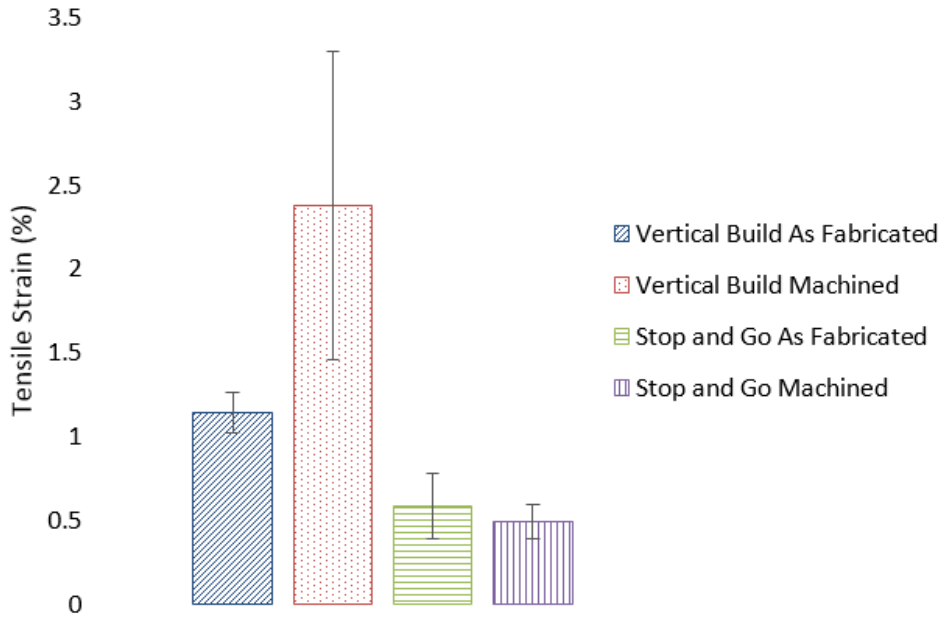

Figure 4.6: Tensile strain result. The error bar shows the +/- standard deviation.

To further understand the structure-property relationship of the low property of stop and go fabricated samples, Figure 4.7 shows the scanning electron microscopy (SEM) images of the fracture surface of specimen fabricated using stop and go process. The SEM image shows the semi-melted and unmelted powder at the fracture surface. The unmelted area causes the voids and porosity within the fabricated parts that could affect the mechanical properties of the stop and go process fabricated parts.

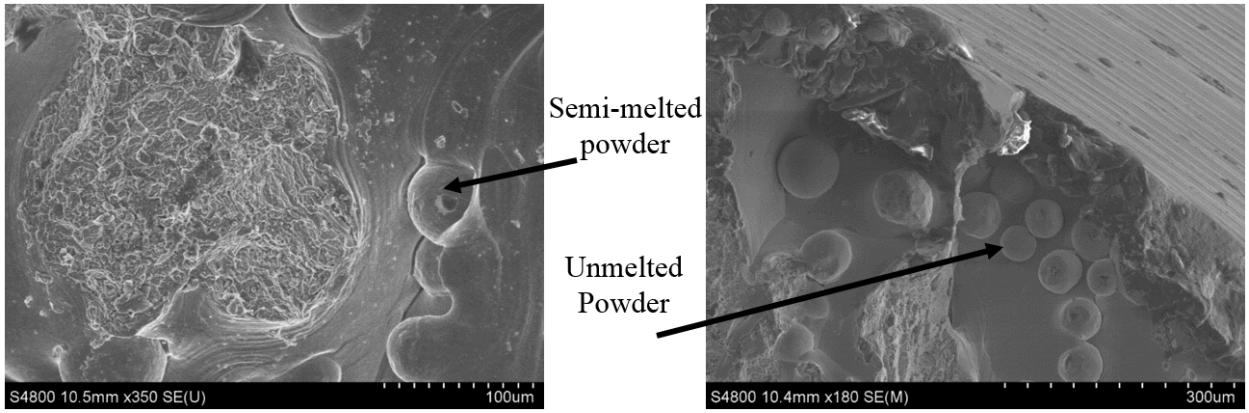

Figure 4.7: Fracture surface of stop and go process fabricated specimen.

The SEM images in Figure 4.7 shows the mechanical properties of the fabricated part could be improved by modifying build parameters to reduce voids. Therefore, six parameter modifications were experimented on the stop and go process to obtain improved mechanical properties. The parameter modifications and explanation are:

- Single melt
- Double melt
- Triple melt
- Temperature and speed modification
- Speed modification
- Temperature modification

Single melt fabrication is similar to the part described as previously mentioned stop and go process. Double and triple melt refers to double and triple melt sequences, respectively. Temperature and speed modification refers to the high temperature and reduced speed fabrication during stop and go process. Speed modification refers to reducing just the speed, and temperature modification refers to the increase of temperature in the build surface. The speed was reduced to half of the regular speed, and increase of temperature was obtained through increasing build current.

Figure 4.8 shows the average ultimate tensile strength (UTS) result obtained for the build modifications applied at the interface. Point to be noted, 0.3 mm was considered as the modification length at the interface. As the fracture occurs at the interface, the parameter modification can be significant only for the interface region. The length was chosen minimal to avoid any further delamination that can happen due to overheating of the interface during the modified fabrication process. The single melt shows the base line for the interface bonding, while the other five modifications shows the increase or decrease of mechanical properties from the base line. A higher average UTS was observed for double melting process and shown a value of 840 MPa. The other modifications showed increase in UTS value other than temperature modification. The temperature modification showed lowest average UTS results only reaching a value of 420 MPa, which is 36% less than baseline result.

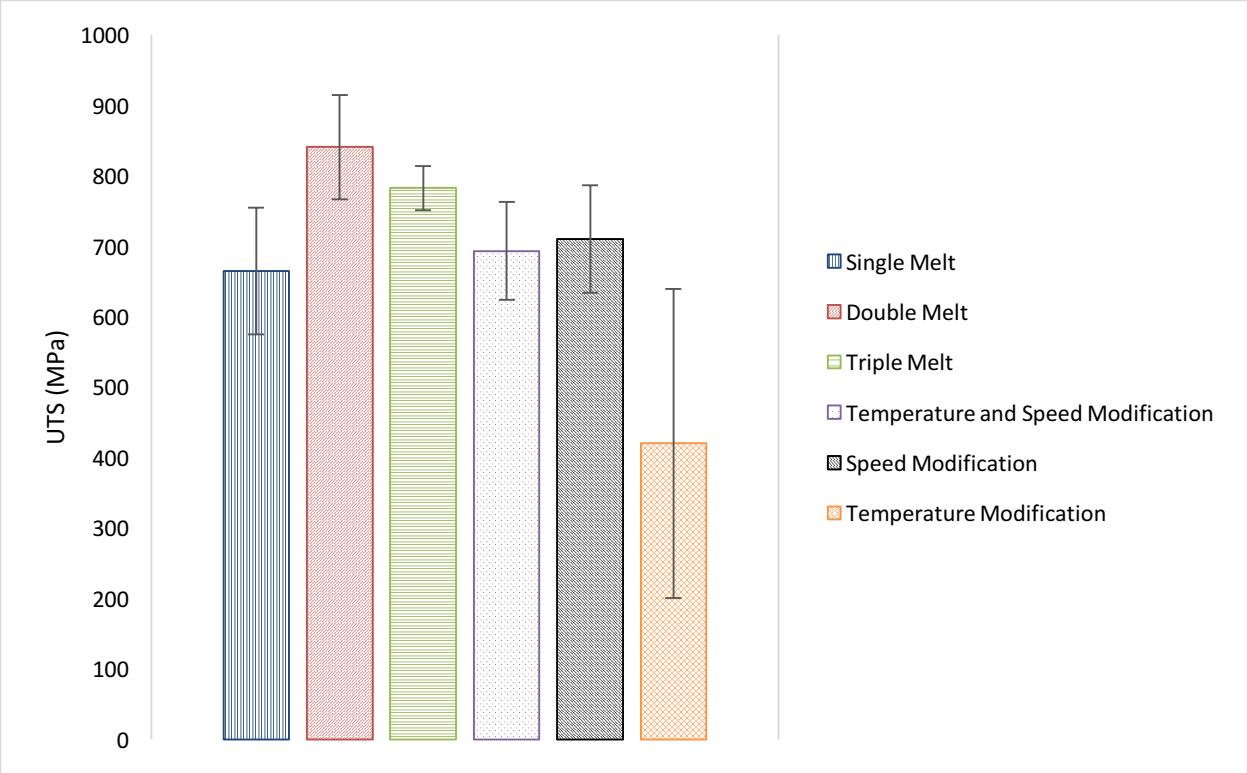

Figure 4.8. UTS result for modifying parameters in paused build fabrication process. The error bar shows the +/- standard deviation

Figure 4.9 shows the Young's modulus result for the six different parameter modifications for the paused build fabrication. The highest average Young's modulus obtained was 123 GPa for the temperature parameter modifications.

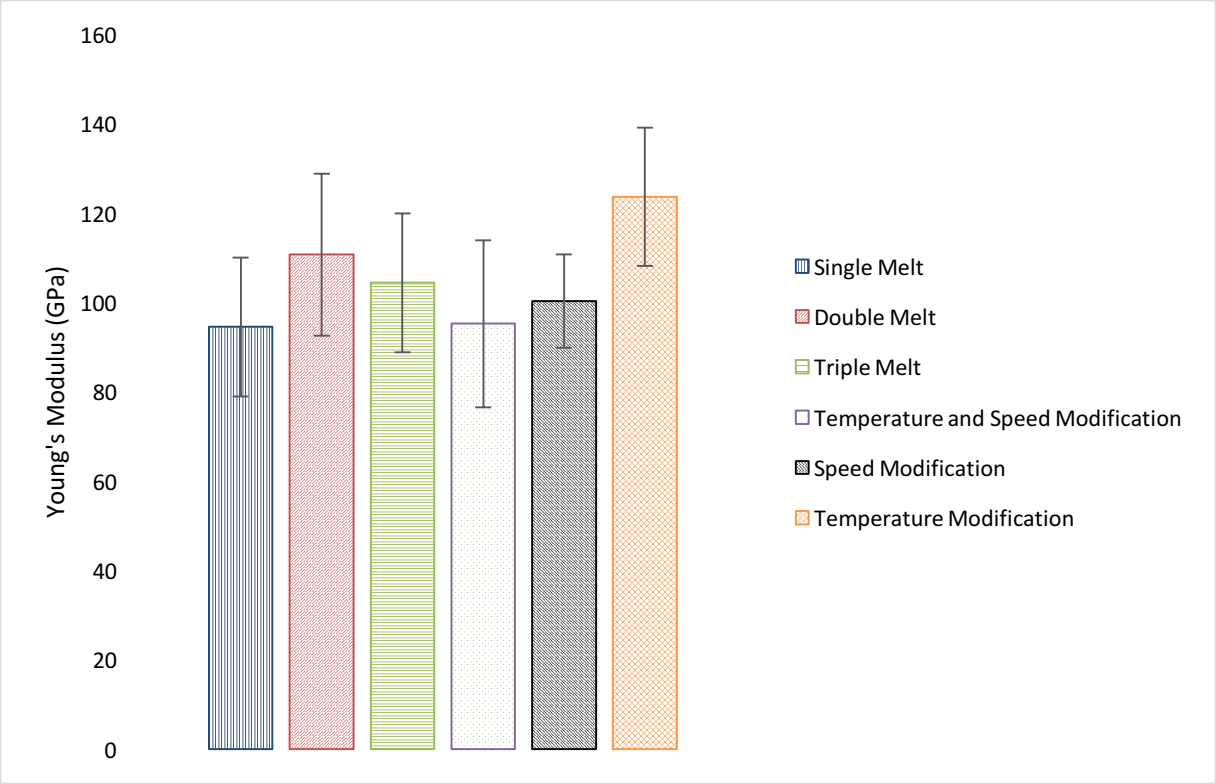

Figure 4.9. Young's Modulus result for modifying parameters in stop and go process. The error bar shows the +/- standard deviation

Figure 4.10 shows the tensile strain results obtained using different parameter modifications. The highest average tensile strain was obtained using double melt and a value of 0.96% was obtained. The tensile strain value shows a low value in compare to any EBM fabricated parts, which shows a further improved can be performed to improve mechanical properties.

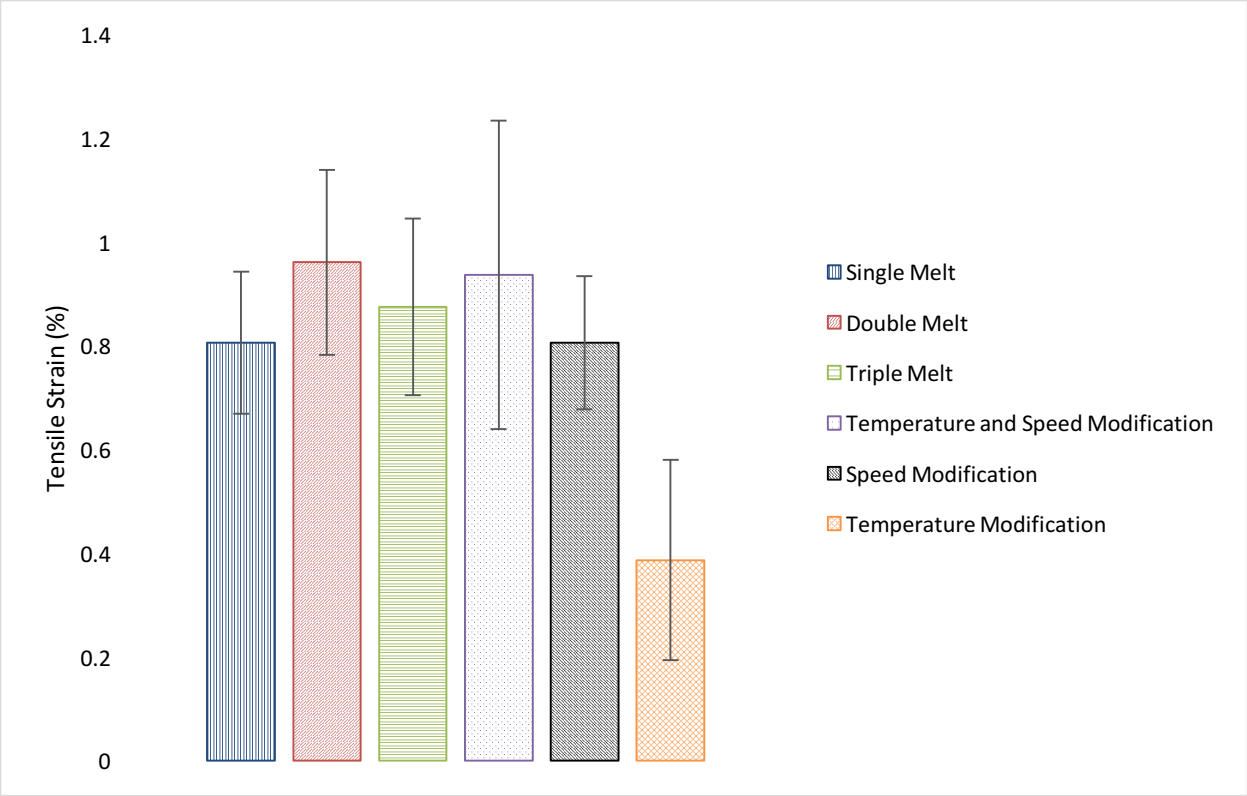

Figure 4.10. Tensile strain result for modifying parameters in stop and go process. The error bar shows the +/- standard deviation

The result shows that the interface bonding can be improved by modifying build parameters. To further improvement, HIPing will be performed on the samples. Typically, the HIPing improves the mechanical properties, mainly tensile strain by removing void or porosity presents in the interface joint.

The parameter modification test has shown that the interface bonding can be improved though modifying build parameters. The improvement was obtained using all build parameters considering specific aspects, such as: UTS, Young's modulus, and tensile strain. Overall, the highest tensile strain and highest UTS obtained using double melt fabrication indicates the better interface bonding in compare to other parameter modification, while having a high Young's modulus as well. The double melting could reduce the unmelted powder seen in Figure 4.7, which improved the interface bonding.

To further understand the structure-property relationship, the tensile results of different parameters used for fabrication, microstructure analysis was conducted in order to get a better relation on the

UTS and Young's modulus. By analyzing the microstructure a closer look was perform on the created interface by the different parameters. The first series of samples that were analyzed were (1) single melt, (5) speed modification, and (6) temperature modification. Figure 4.11 is an optical image of the single melted parts after polishing and etching. The bottom or first build microstructure shows a more Widmanstätten structure, where the top build has a finer grain structure, which could result in a larger strength or harder material.

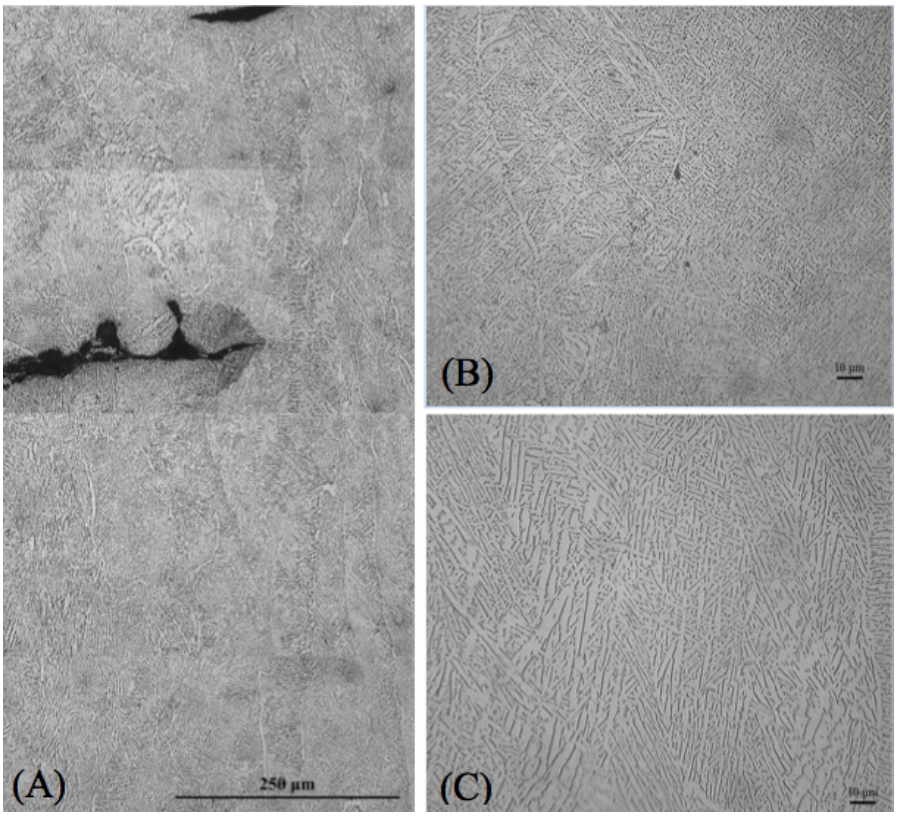

Figure 4.11: (A) Created interface of single melt process (B) Top microstructure and (C) bottom microstructure for parts fabricated using single melt parameter.

Samples in Figure 4.11 were section in the vertical direction, mounted, polished, and etched using Kroll's etchant (92% water, 6% Nitric acid, and 2% hydrofluoric acid) used typically in titanium alloys. The microstructure should provide the verification of the results for the tensile test. According to the tensile tests that were conducted (6) temperature modification parts should have a non-coherent interface causing separation between the two builds. Speed modification parts had higher UTS when compared to single melt parts, which should have a stronger interface. Note a large interface region is visible on figure 4.11 (a) where the image was obtained at lower

magnification than images (b) and (c) in order to gain the ability to identify the two different builds, however a columnar orientation of grains are lost as the second or top fabrication took place.

For the next parameter, where the modification came by reducing the fabrication speed, higher UTS was achieved when compared to single melt parameters. Figure 4.12 shows that between two different built, a common microstructure is visible. The second build or the top section (Figure 4.12 (a)) does appear to have a finer grain structure with more beta phase present (darker region).

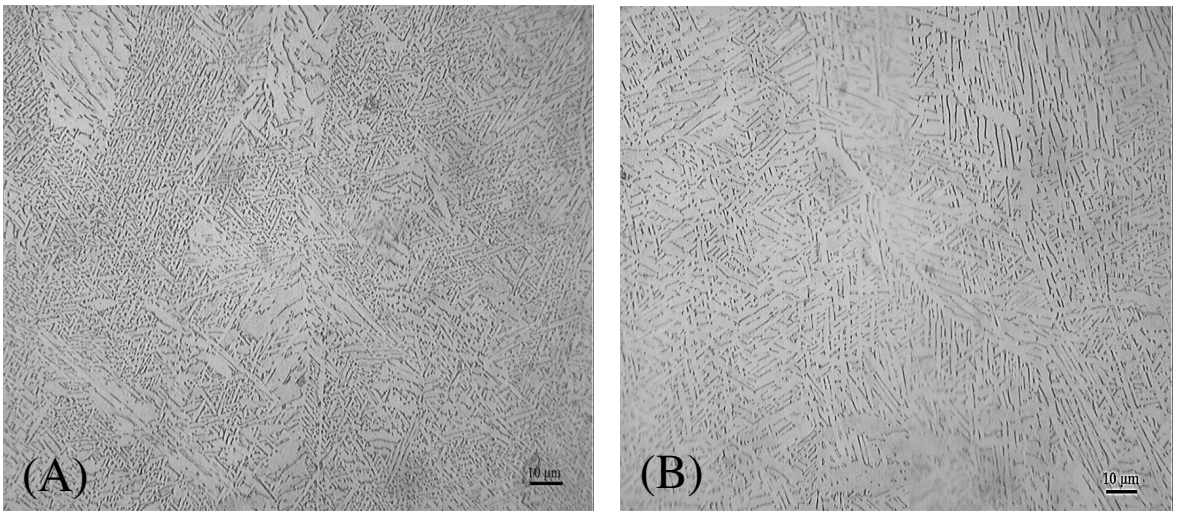

Figure 4.12. (A) Top or second build and (B) bottom or first build for speed modified parameter.

Samples that were built using higher temperature during the second fabrication produced lowest UTS of all the different parameters. The second fabricated section shows a martensitic microstructure (Figure 4.13 (A)), which is a typical brittle phase. By having a much more brittle phase the top build when compared to the bottom build, a reduction in UTS is predicted since there is a significant difference is hardness. Figure 4.13 is the optical images obtained for temperature-modified parameters.

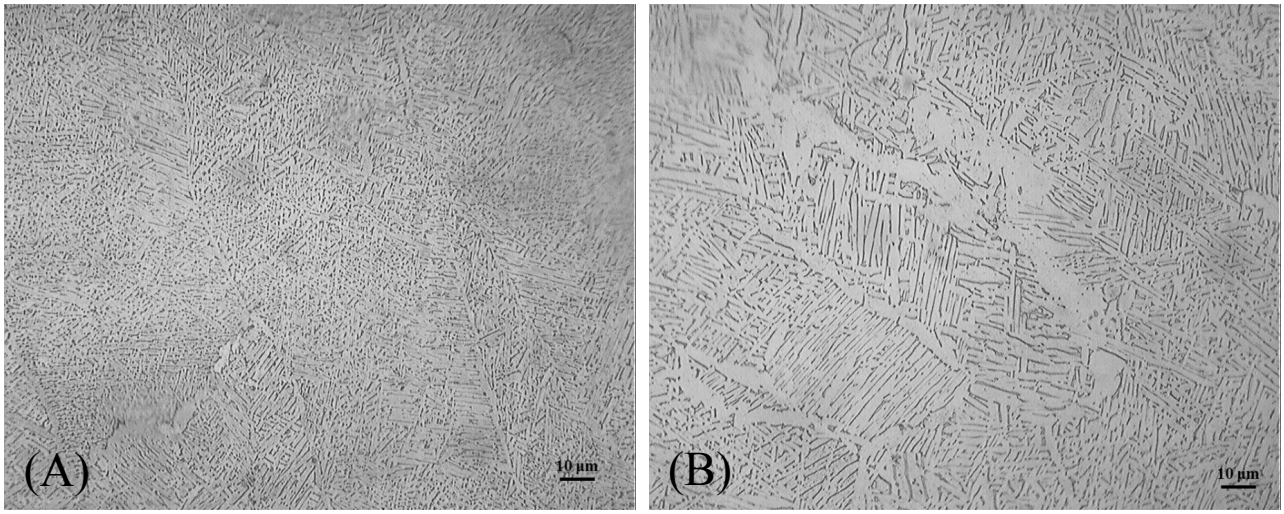

Figure **4.13**: (A) Top or second build and (B) bottom or first build for temperature modified parameter.

4.3 Fracture Surface Analysis

Figure 4.14-4.19 shows the SEM image of the fracture surface for the aforementioned parameter modifications. Figure 4.14 shows the SEM images of single melt interface. The image shows some unmelted or semimelted powder (Figure 4.14(a) and (b)) present at the interface joint. The surface shows mostly brittle surface while showing some place of ductile surface. Point to be noted, the ductile surface (Figure 8(c)) is commonly seen in Ti-6Al-4V parts fabricated using EBM.

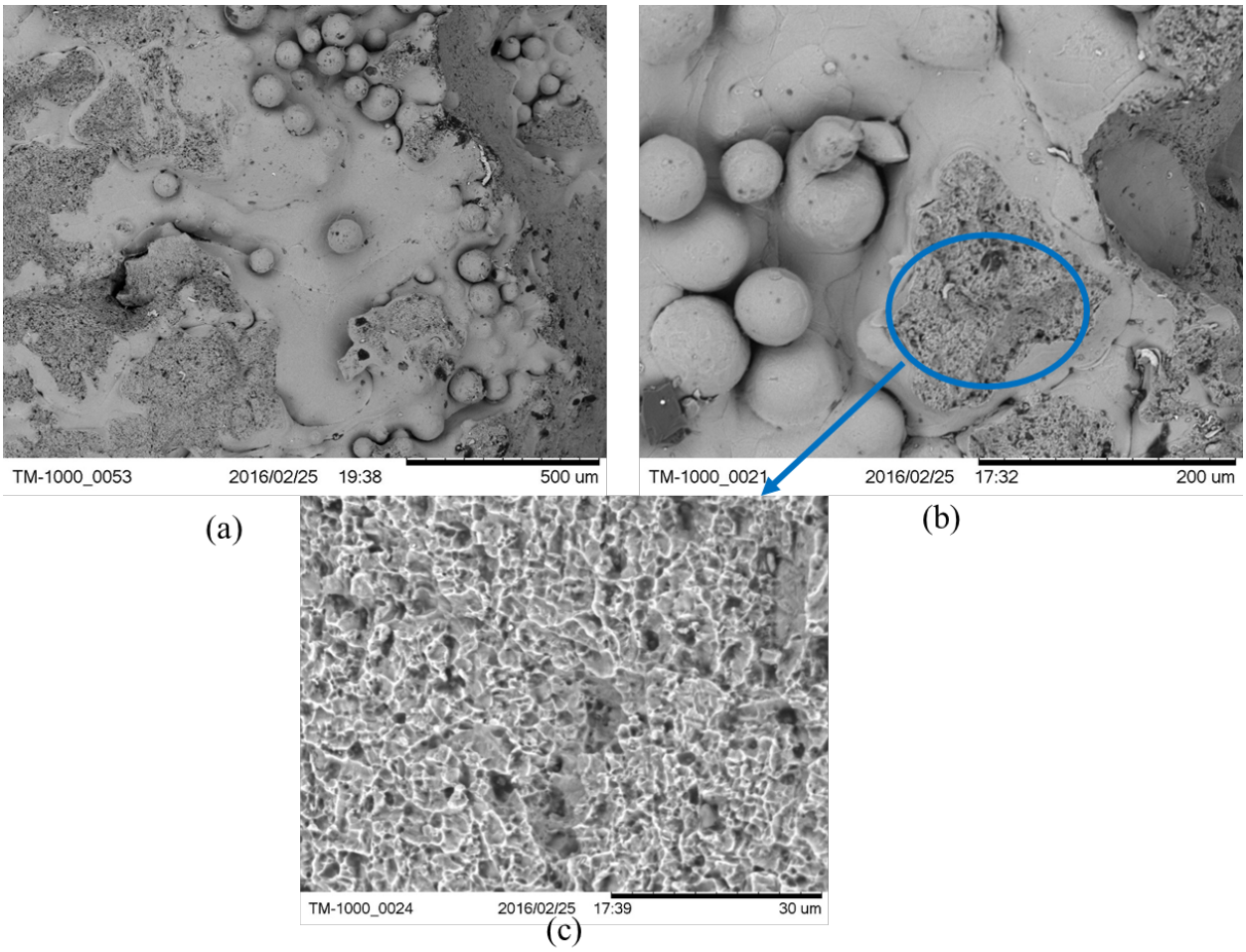

Figure 4.14: SEM images showing the interface bonding of single melt build, (a) showing both brittle and ductile surface, (b) plane showing ductile surface, and (c) zoomed in view of ductile surface

Figure 4.15 shows the SEM image of double melt interface joint. The image shows some unmelted and semi-melted powder. The point to be noted that the image shows more ductile surface in compare to the single melt surface. The increase of ductile surface might be the reason of improved mechanical properties of double melt interface bonded parts.

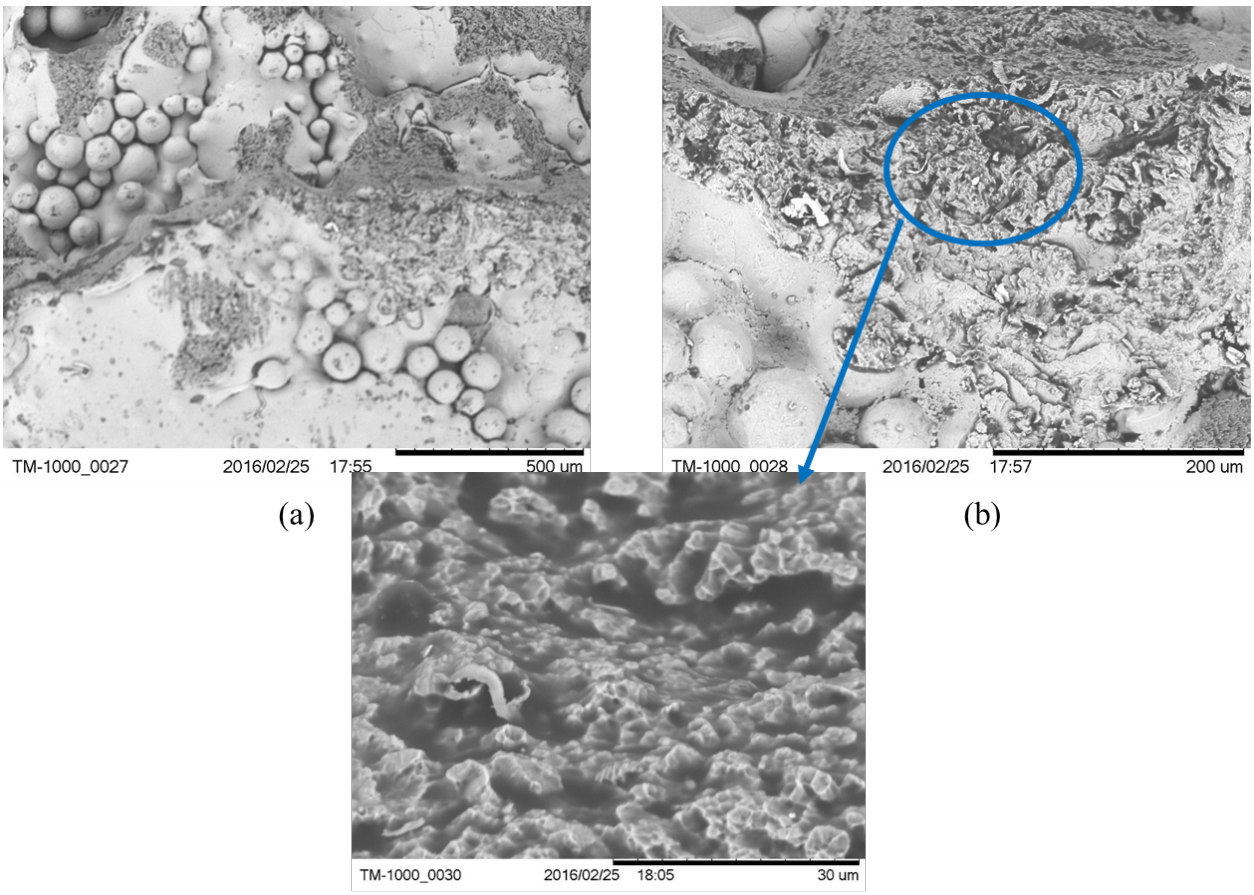

Figure 4.15: SEM images showing the interface bonding of double melt build, (a) showing both brittle and ductile surface, (b) plane showing ductile surface, and (c) zoomed in view of ductile surface

Figure 4.16 shows the SEM images of triple melt interface joint. The image shows significantly low amount of unmelted and/or semi melted powder in compare to single and double melt. High temperature and rapid cooling can cause microstructural change that needs to be analyzed in future.

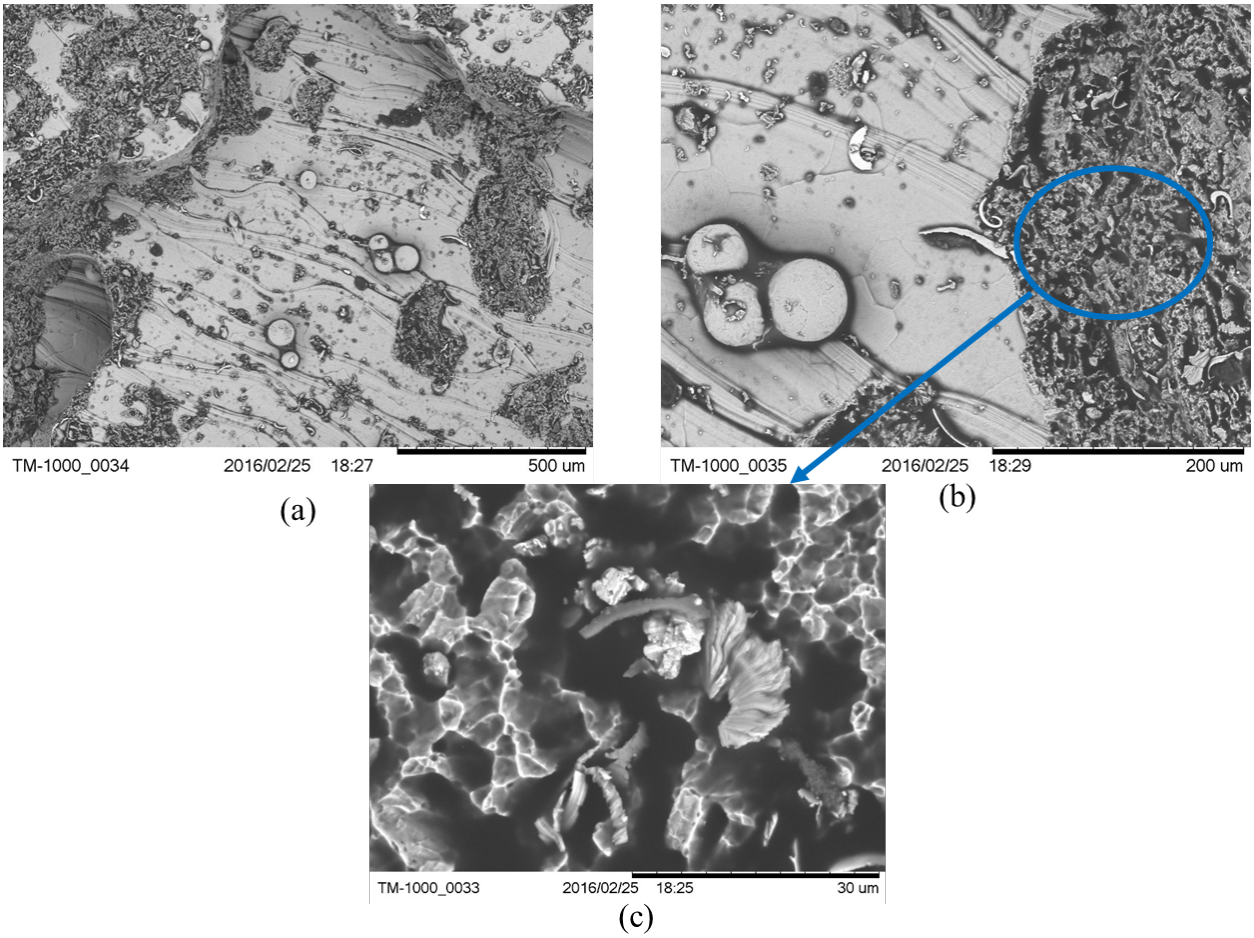

Figure 4.16: SEM images showing the interface bonding of triple melt build, (a) showing both brittle and ductile surface, (b) plane showing ductile surface, and (c) zoomed in view of ductile surface

Figure 4.17-4.19 shows the temperature and speed modification, speed modification, and temperature modification part's fracture surface. The fracture surface shows similar characteristics in the planes that has been discussed so far. The fracture surface shows unmelted and semi melted powder on the surface which can create in plane porosity, which can be detrimental for mechanical properties.

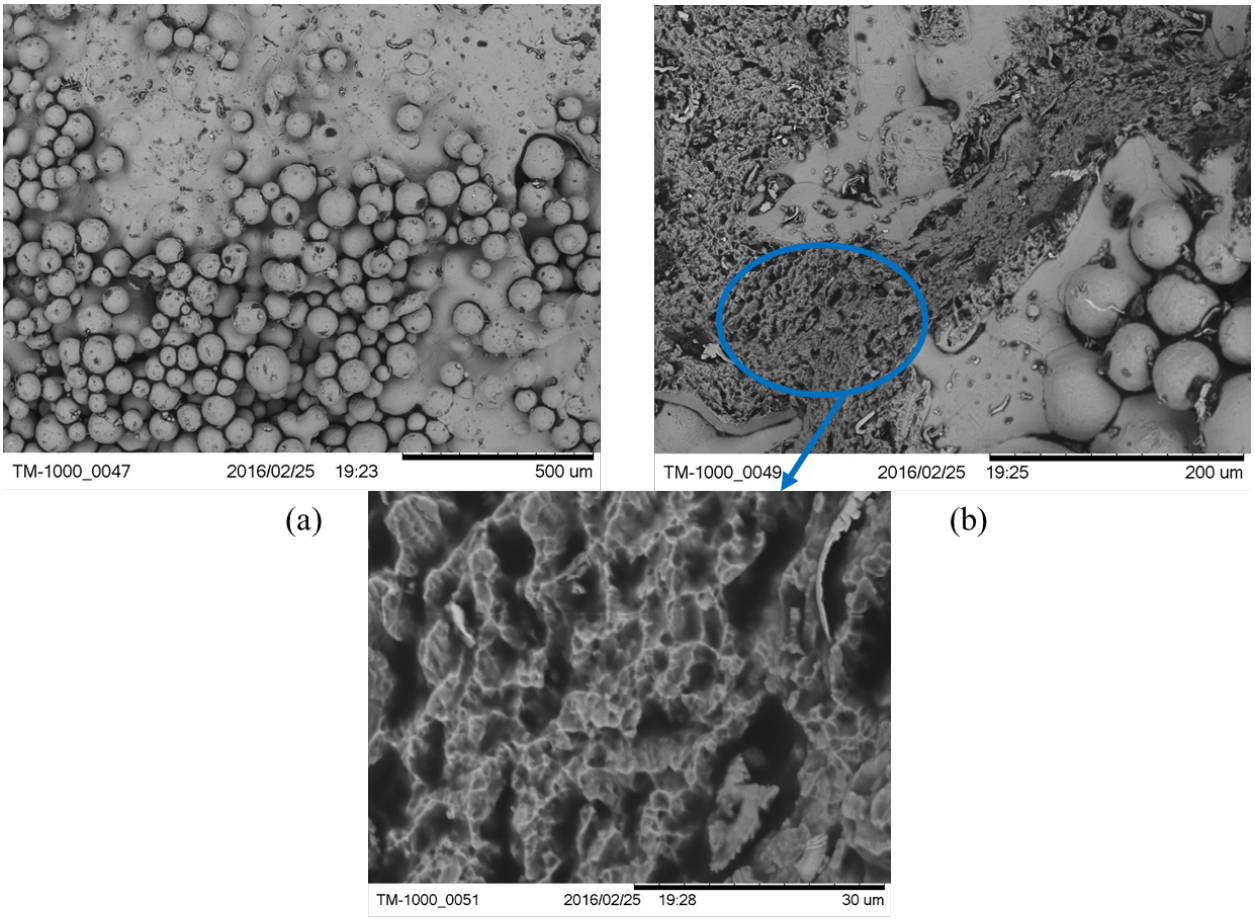

Figure 4.17: SEM images showing the interface bonding of temperature and speed modified build, (a) showing both brittle and ductile surface, (b) plane showing ductile surface, and (c) zoomed in view of ductile surface

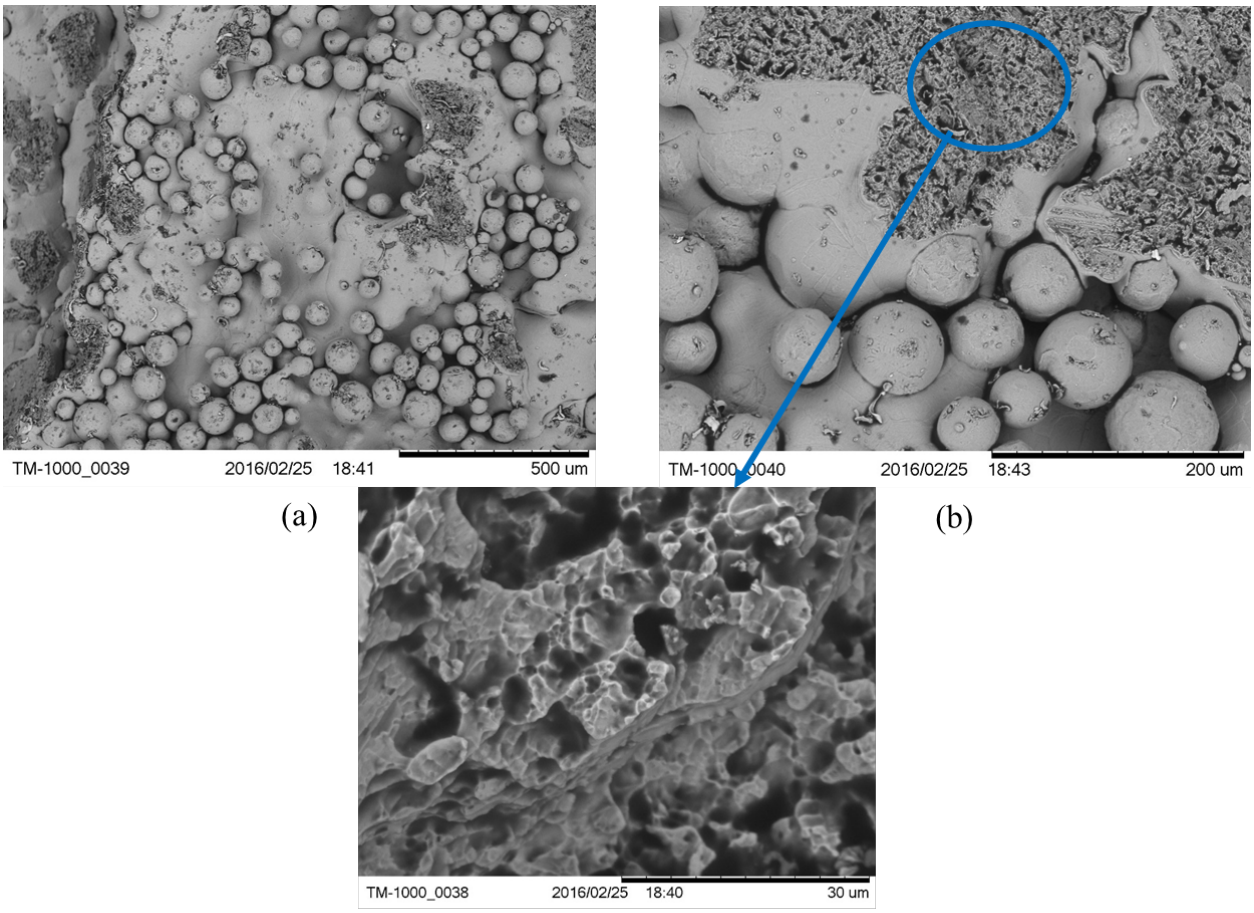

Figure 4.18: SEM images showing the interface bonding of speed modified build, (a) showing both brittle and ductile surface, (b) plane showing ductile surface, and (c) zoomed in view of ductile surface

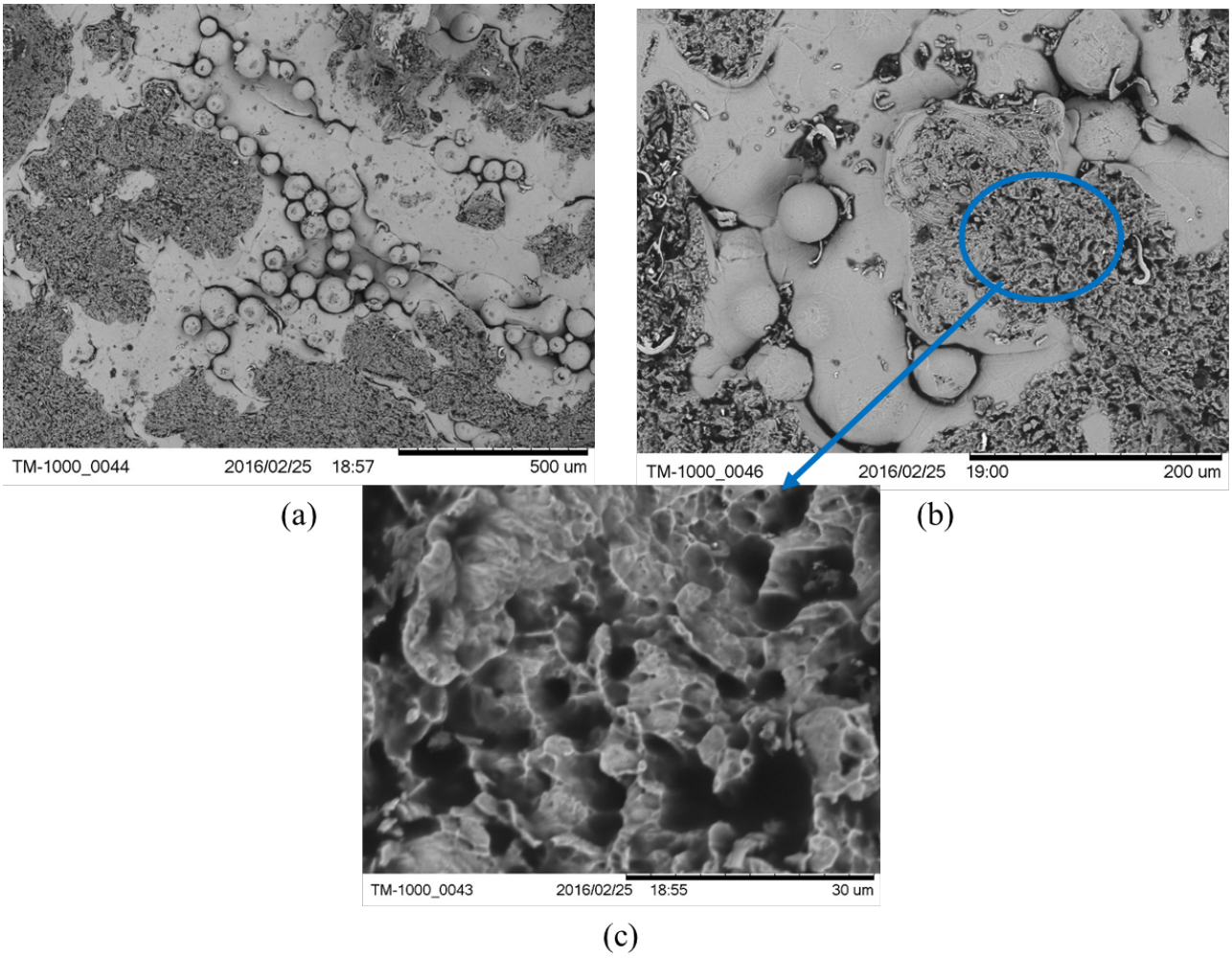

Figure 4.19: SEM images showing the interface bonding of temperature modified build, (a) showing both brittle and ductile surface, (b) plane showing ductile surface, and (c) zoomed in view of ductile surface

4.4 Effect of HIPping

The paused build tensile test specimens were fabricated using electron beam melting technology and then, the specimens were underwent hot isostatic pressing (HIP) process. The processing parameters were 1650° F and 15 ksi isostatic pressure for 2 hours. The tensile properties in between HIPped test specimens and non-HIPped parts were compared and reported. The comparison of mechanical properties of paused build fabricated specimens in HIPping with non-HIPping condition is shown in Figures 11-13. The parameter modifications are following:

1. Single scan
2. Double scan

3. Triple scan

Single scan refers to 1 melting sequence was applied in the interface at the same layer height, while double and triple scan means apply of 2 and 3 melting sequence, respectively. Figure 4.20 shows the average ultimate tensile strength (UTS) result obtained for the build modifications applied at the interface and comparison of HIPped and non-HIPped test samples. Point to be noted, 0.3 mm was considered as the modification length at the interface. The parameter modification was applied in the interface as the interface can work as a weak bonding place. The length was chosen minimal to avoid any further delamination that can happen due to overheating of the interface during the modified fabrication process. A highest 23% increase in HIPped sample in comparison with a non-HIPped sample was observed using a single melt build fabrication process. The highest average UTS value of 840 MPa was obtained using a double scan method. There was no statistically significant difference was observed in between non-HIPped and HIPPed sample for double and triple scan method.

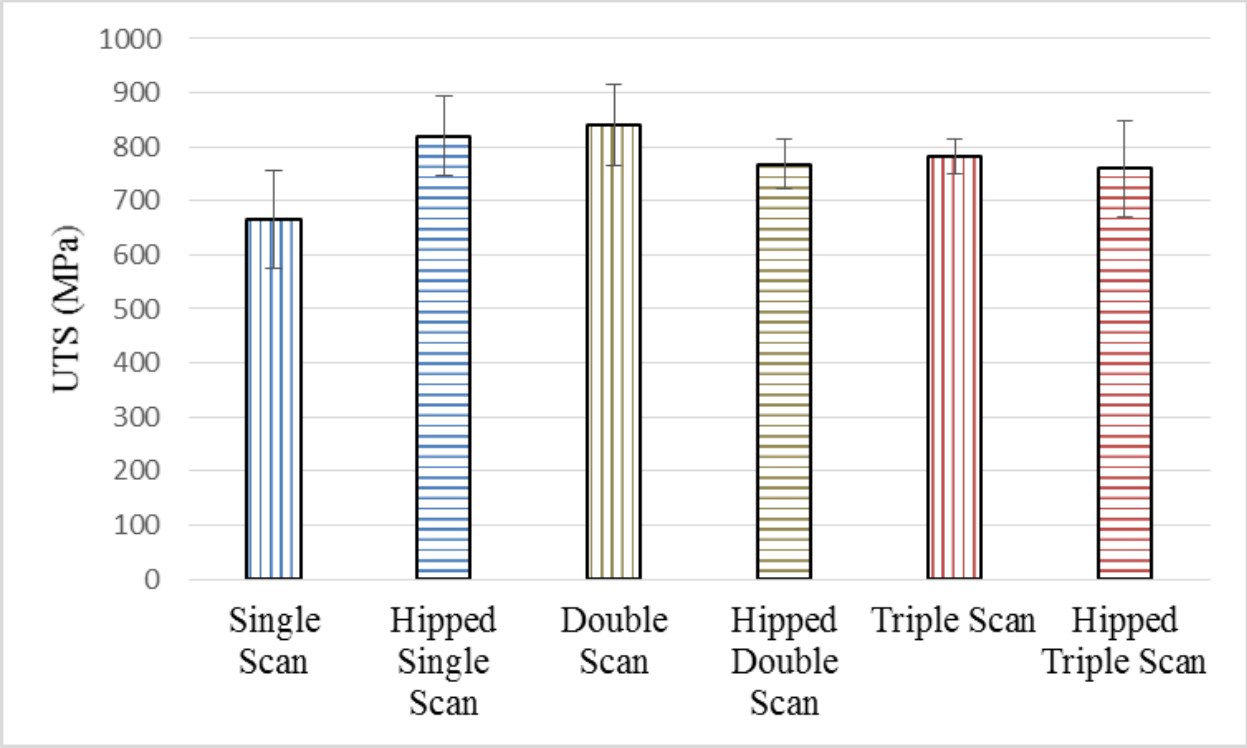

Figure 4.20. UTS result for modifying parameters in paused build fabrication process for both non-HIPped and HIPped sample. The error bar shows the +/- standard deviation

Figure 4.21 shows the Young's modulus result for the 3 different parameter modifications for non-HIPped and HIPped sample. The highest average Young's modulus obtained was 110 GPa for the double scan build method.

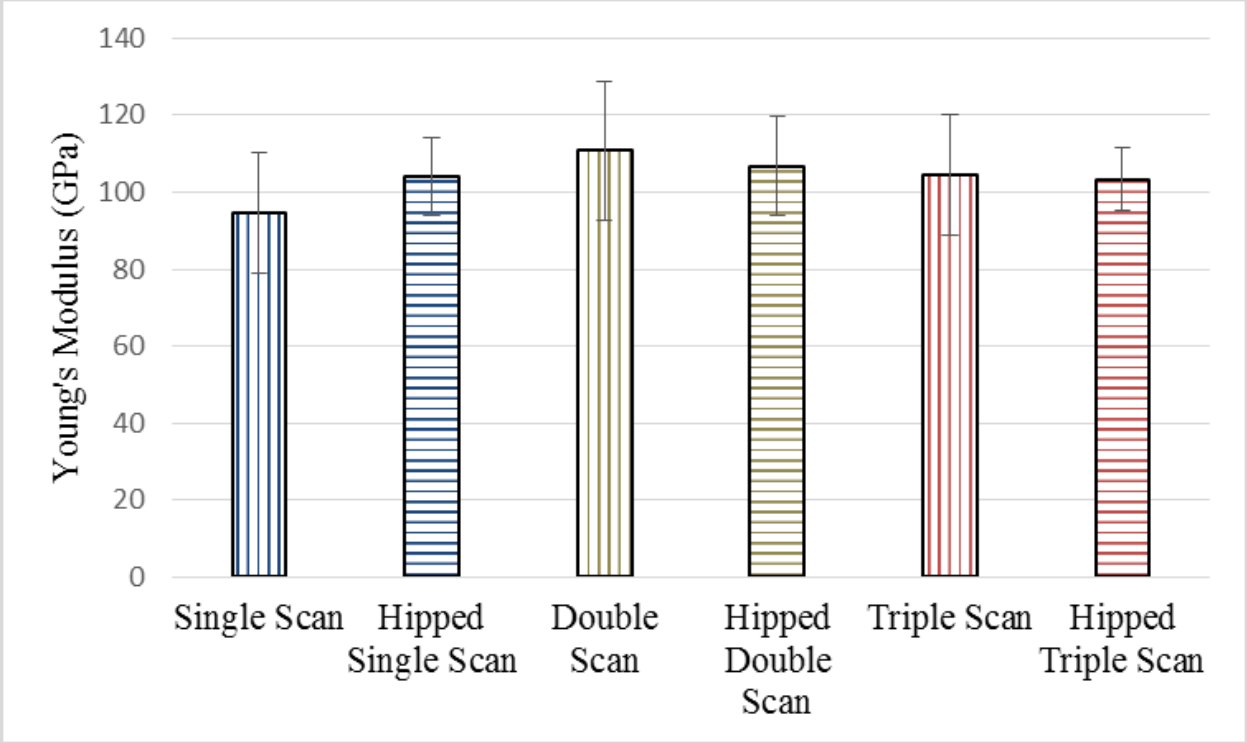

Figure 4.21. Young's Modulus result for modifying parameters in paused build fabrication process showing comparison in between non-HIPped and HIPped samples. The error bar shows the +/- standard deviation

Figure 4.22 shows the tensile strain results obtained using different parameter modifications. The average tensile strain values show a value of <1% in all parameter modifications. The specimens broke in the elastic region showing brittle behavior.

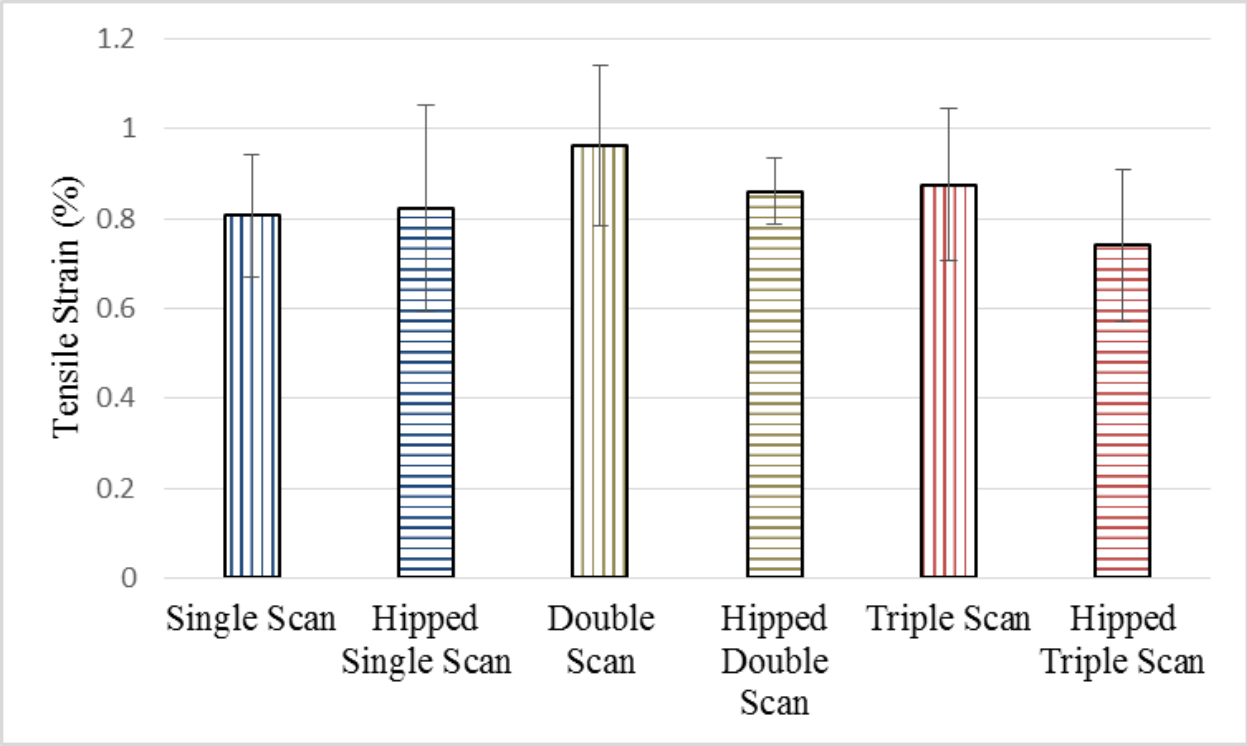

Figure 4.22. Tensile strain result for modifying parameters in stop and go process. The error bar shows the +/- standard deviation

Figure 4.23-4.25 shows the SEM image of the fracture surface for the aforementioned parameter modifications. Figure 14 shows the SEM images of non-HIPPed test samples. The single scan, double scan, and triple scan non-hipped fracture is shown in Figures 4.23(a), 4.23(b), and 4.23(c), respectively and Figures 4.23(d), 4.23(e), and 4.23 (f) shows the zoomed in view of the fracture surfaces. The figure shows brittle surface with the presence of ductile surface. The ductile surface shows dimples present in the fracture surface. The zoomed in view show the sizes of the dimples change in the interfacial bonded parts. Unmelted powder can be seen in the fracture surface for all 3 build method. All though, triple melt shows significant decrease in unmelted powder.

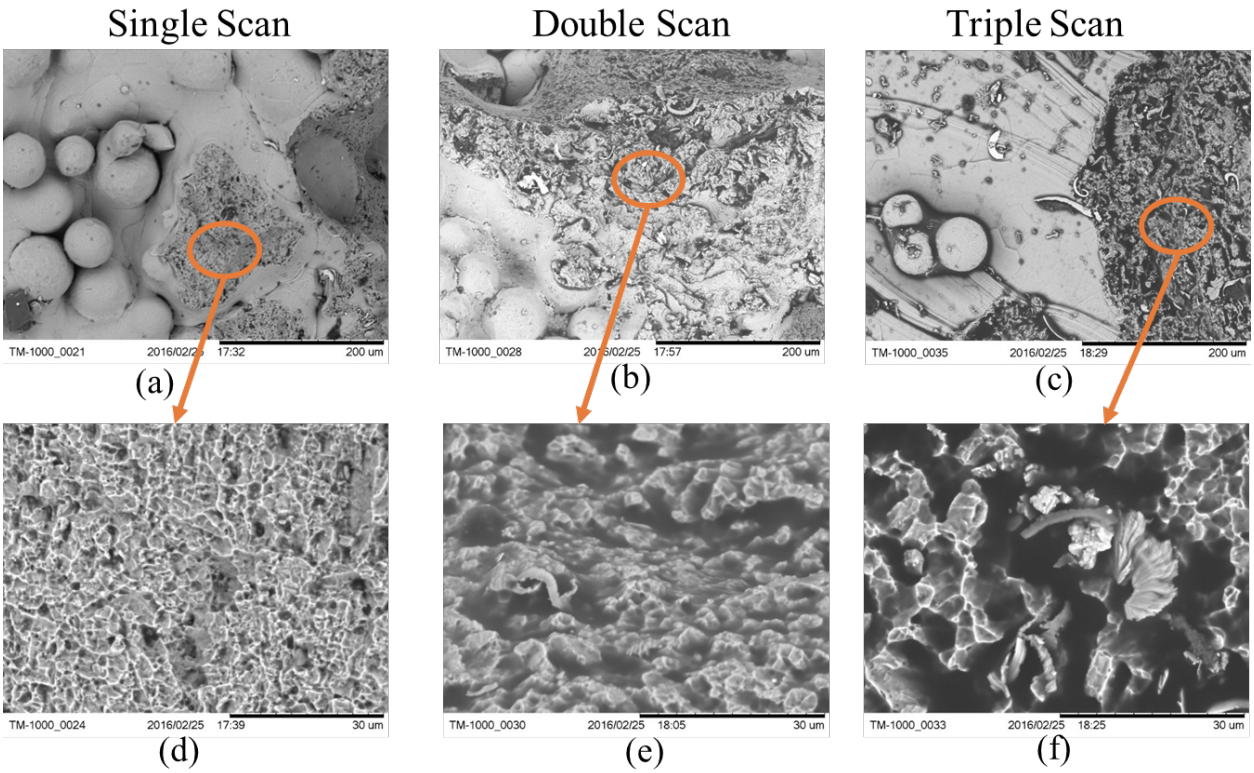

Figure 4.23: SEM images showing the interface bonding of non-hipped part, (a) single scan (b) double scan, (c) triple scan, (d) zoomed in view of single scan, (e) zoomed in view of double scan, and (f) zoomed in view of triple scan.

Figure 4.24 shows the SEM image of hipped samples. The single scan, double scan, and triple scan hipped fracture is shown in Figures 4.24(a), 4.24(b), and 4.24(c), respectively and Figures 4.24(d), 4.24(e), and 4.24 (f) shows the zoomed in view of the fracture surfaces. The fracture surface of HIPped samples is mostly showing ductile surface. Some pores can be observed in the fracture surface. Unmelted powder is not visible in the fracture surface of the HIPPed test specimens.

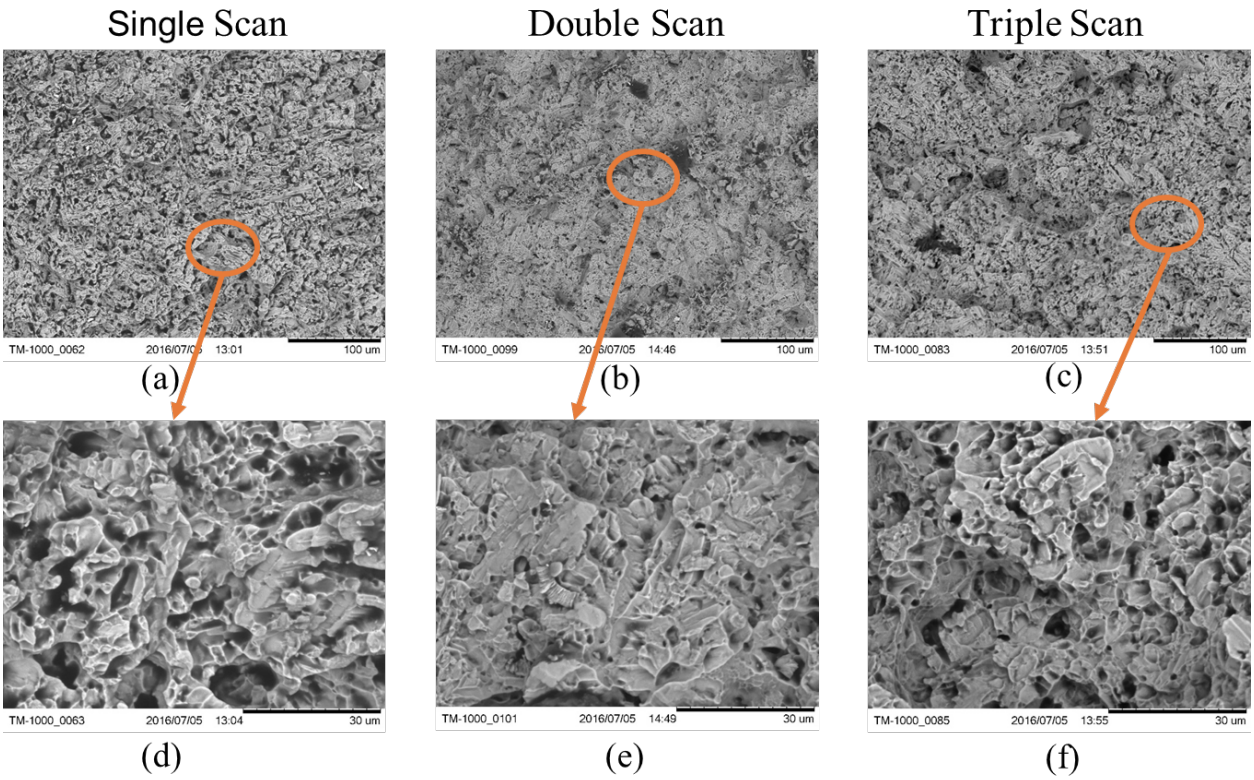

Figure 4.24: SEM images showing the interface bonding of hipped part, (a) single scan (b) double scan, (c) triple scan, (d) zoomed in view of single scan, (e) zoomed in view of double scan, and (f) zoomed in view of triple scan.

Figure 4.25 shows the entire fracture surface for both non-HIPped and HIPped test specimens. Figure 4.25(a)-16(c) shows the fracture surface of non-HIPped samples for single scan, double scan, and triple scan, respectively. The brittle and ductile surface with the presence of unmelted powder can be seen in the fracture surface. Figure 4.25(d)-4.25(f) shows the fracture surface for the HIPped samples. The ductile fracture region can be seen for the HIPped test specimens.

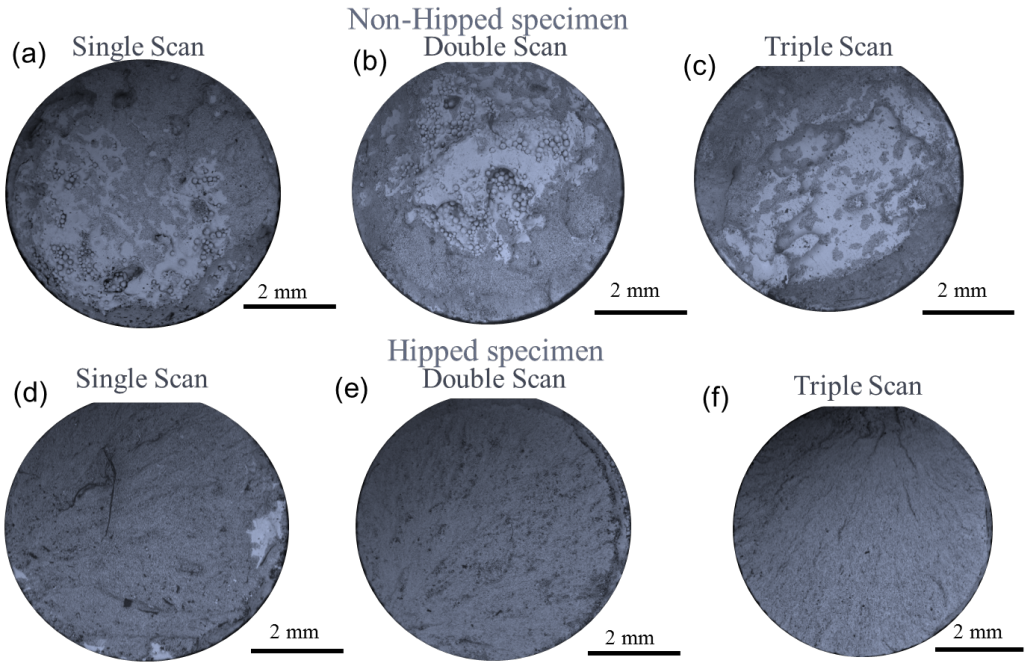

Figure 4.25: SEM images showing the entire fracture surface, (a) non-HIPped single scan, (b) non-HIPped double scan, (c) non-HIPped triple scan, (d) HIPped single scan, (e) HIPped double scan, and (f) HIPped triple scan

CHAPTER 5 SMART INJECTOR FABRICAITON AND TESTING

5.1 Smart Injector Design

We continued our fabrication process using selective laser melting (SLM) process. Inconel 625 was used as fabricated material for its property as a high strength and high temperature resistance properties. Lead zirconate titanate (PZT) and lithium niobate (LiNbO3) was used as a piezoceramic sensor material. The fabrication process of the smart injector using SLM technology is shown in Figure 5.1. The process starts with fabricating insert part that is going to inhibit the sensor material inside the injector and provides a plane space for continuation of fabrication process. Then, the bottom section is fabricated on the start plate. During the entire process, the partial build injector is attached to the start plate. The sensor material, insulating material (alumina plate), electrodes, and insert part are stacked together in the predesigned cavity. After the embedding process, the part is placed again in the build platform. The fabrication process continues until the process is complete. The fabricated injector is then cut down using a bench saw or any other cutting tool. The powder was removed from the injector using compressed air flow in the cavity and further powder removal was performed using ultrasonic energy. A point noteworthy, two sets of sensor assembly was used in both predesigned cavities. As a result, we can have two sensor data set to verify the results. Two thermocouple slots were included in the design for better monitoring process.

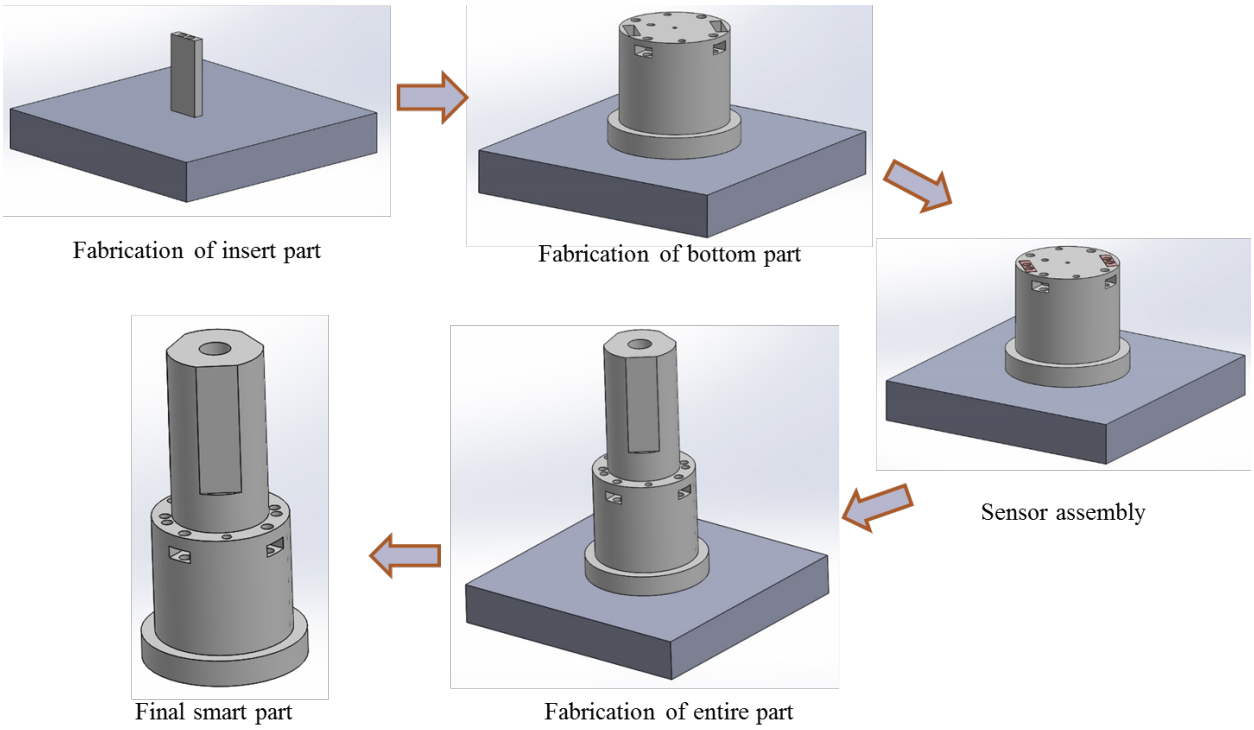

Figure 5.1. Schematic diagram of smart injector fabrication process

Figure 5.2 shows the fabricated smart injector with two sensor material embedded inside the metallic bod. The electrodes are only parts of sensor assembly that are visible from outside. The injector is attached to the build plate that was cut off before combustion testing.

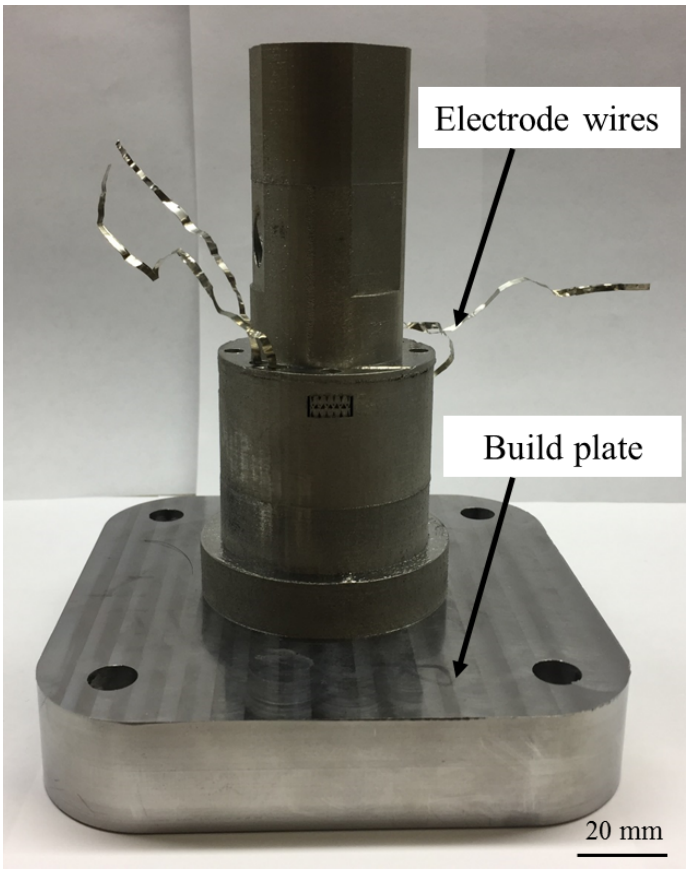

Figure 5.2: Smart injector fabricated using SLM technology

5.2 Surface Roughness Measurements

As we mentioned before, the pressure drop is directly affected by the surface roughness of the fabricated material. We also measured the surface roughness of the fabricated fuel injector using a laser based optical profilometer, the surfaces of the fabricated injectors were analyzed. As figure 5.3 shows, the EBM finishing is seven times the machined counterpart. A fabricated structure using SLM, improves significantly the roughness of the EBM, but it is 3x higher than the machined counterpart. This results will be used in the analysis of pressure drop for the combustion implementation of the smart injector.

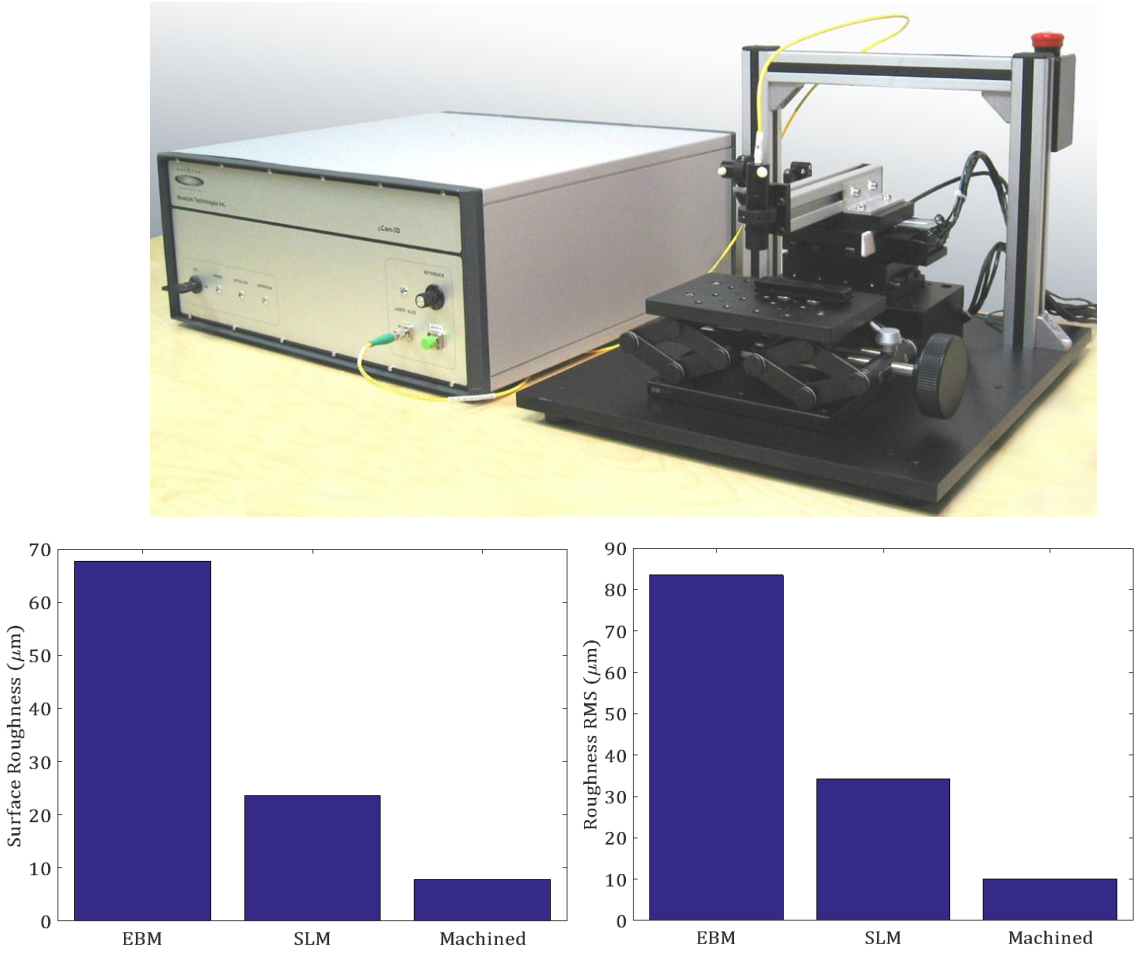

Figure **5.**3: Surface roughness and RMS roughness of the fabricated structures.

5.3 Smart Injector Testing in Combustion Environments

The smart injector was testing using hot firing experiments to show the functionality of the smart injector in combustion environments. The objective of the experiments are as follows:

- prove the functionality of a 3D printed coaxial shear injector fabricated using additive manufacturing (SLM)
- Provide heat exposure to a coaxial shear injector with embedded pyroelectric ceramic for current sensing in a real energy system application.
- Compare the temperature measured by the sensor to the thermocouple readings placed at different locations of the system.

The ignition system was composed of a swirl coaxial torch igniter, where air and methane works as oxidizer and fuel, respectively. The spark was created using a torch igniter. Figure 5.4 shows the set-up of torch ignitor.

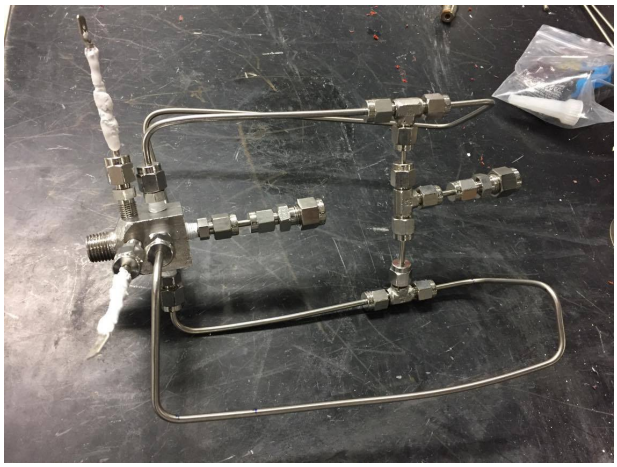

Figure 5.4. Torch igniter assembly used to initiate the combustion inside the MOAC.

The injector was tested to measure the pressure drop and flow rates using water pressure. Those parameters are important to obtain the desired flow rate. The injector is connected to a 50 psi tank and pressure at the outlet was measured using pressure transducer. Figure 5.5 shows the pressure drop testing setup.

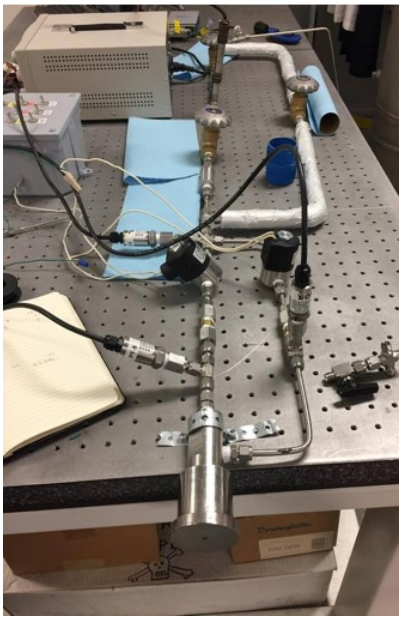

Figure 5.5. Set up used to measure the pressure drop of the smart injector

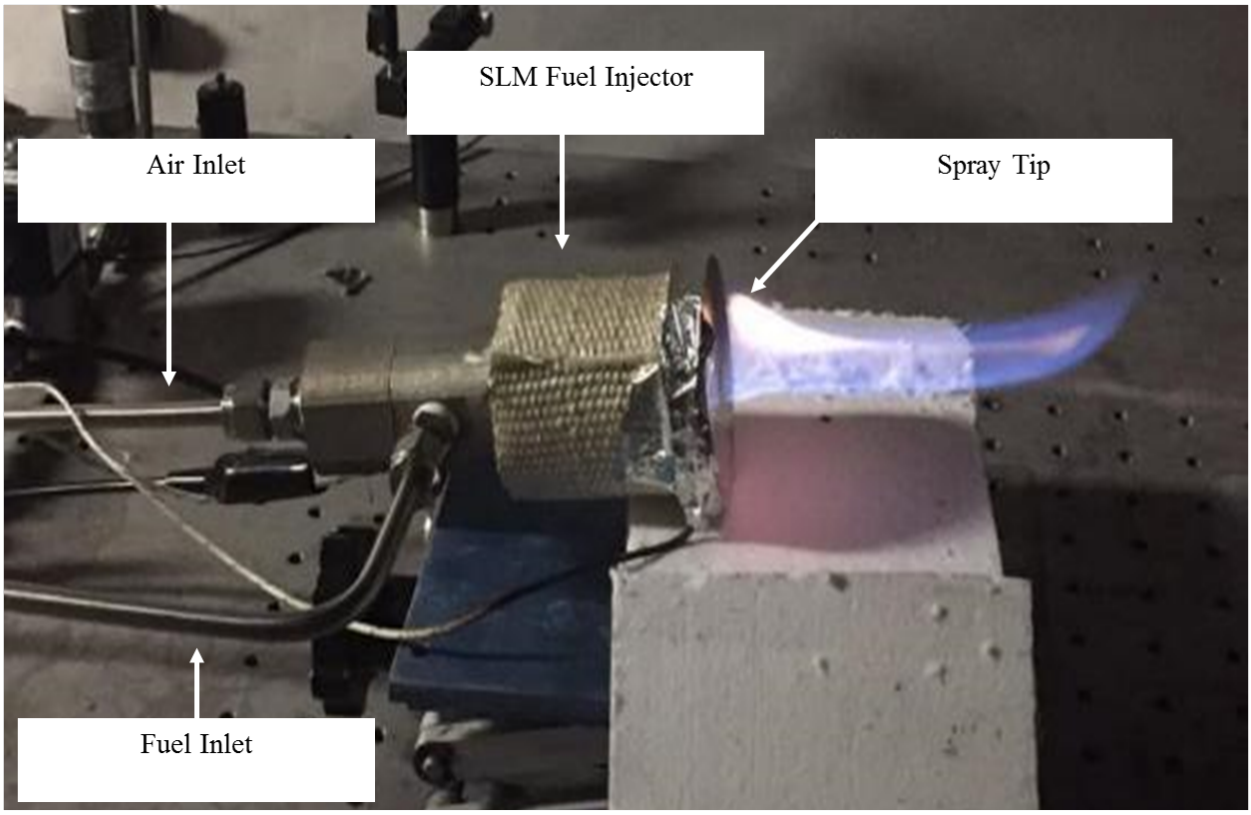

Figure 5.6: Testing of smart injector in combustion chamber

Figure 5.6 shows the smart injector testing in combustion chamber environments. The testing was performed to obtain the flame using the smart injector. The temperature of the tip was measured using sensor responses from the injector. The result was compared with a thermocouple temperature reading. The testing result is shown in Figure 5.7.

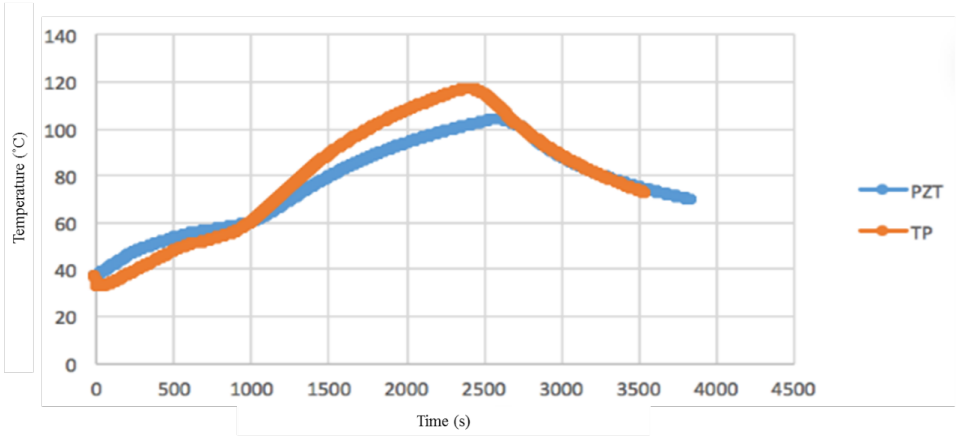

Figure 5.7: Testing results of smart injector testing in combustion environments

The testing showed a highest temperature rise of injector of 120º C. The typical injector temperature was not getting temperature as high as or close to flame temperature. Although, any kind of thermal shock or backfire can cause high temperature in the injector surface. The temperature of thermocouple showed good agreement with temperature calculated using PZT sensor material. That shows the viability of using piezoceramic sensor material in fabricating smart parts.

5.4 Microstructural Evaluation of Stop and go process

SLM fabricated “smart part” full microstructure is visible in Figure . The magnified views of the three interested areas are seen in Figure ; where (b) is first built, (c) interface, and (d) second built. The image reveals the large presence of melt pools, with no large difference with the three areas. All three magnified image appear with similar precipitate formation seen in pervious analyzed SLM Inconel 625 microstructure. The main difference observed is the distance between the melt pools of the first and second builds to the interface. As the second fabrication is initiated, the top surface of the first built interacts with the the laser multiple times, creating closer distances between melt pools. Second built had a average of 45 µm between layered melt pools, while an average of 23 µm on the interface. This issued may be resolved if the sample is heat treated (HIPed) removing the melt pool microstructure and leaving more exquiaxied grains structure. The minimal change or difference in microstructure for a stop-and-go SLM fabricated part leads to a more ideal fabrication process between the two powder bed fusion technologies.

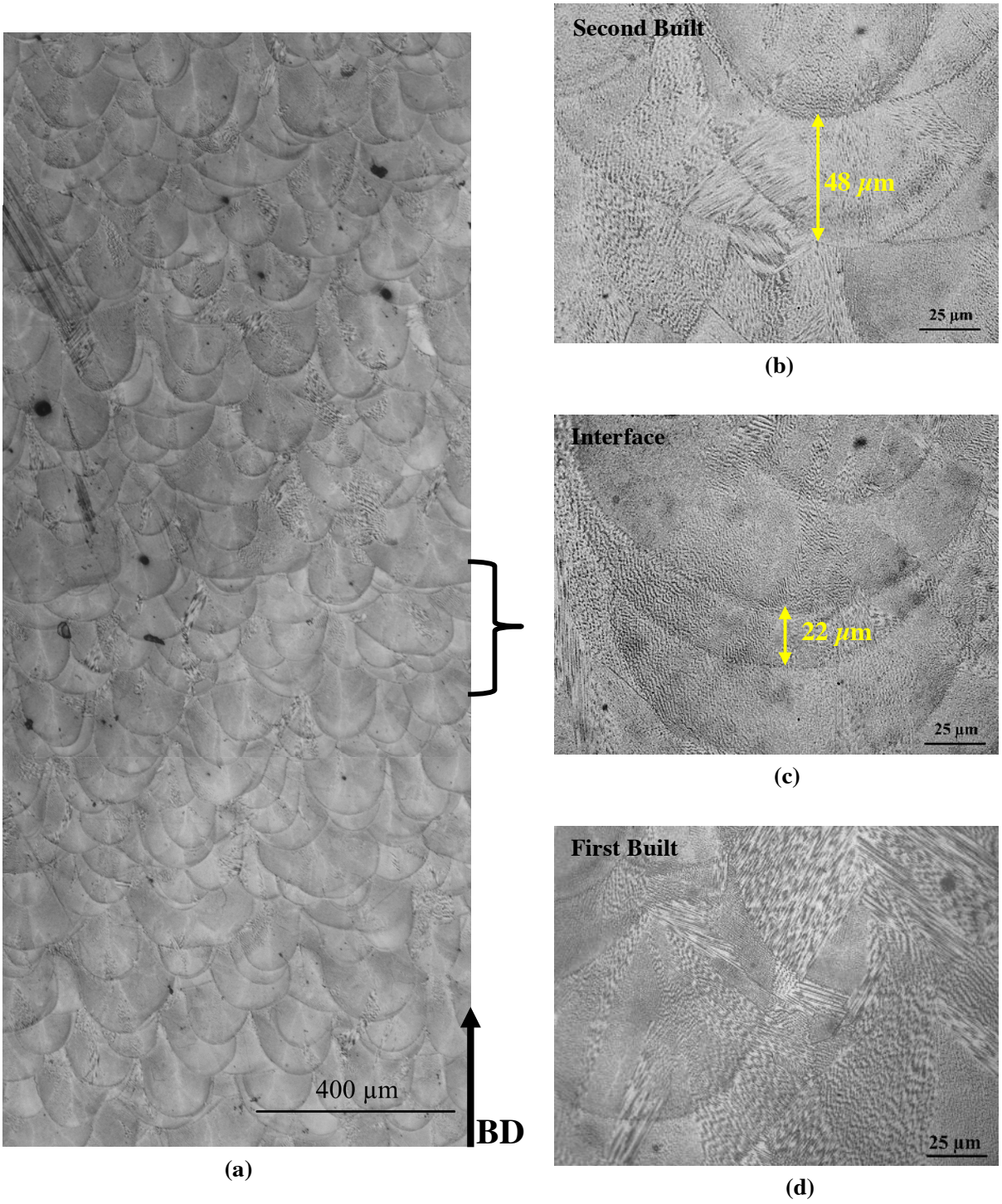

Figure **5.**8. Optical images of microstructure for SLM fabricated smart part, (a) entire microstructure view showing the evolution of the microstructure is paused, then continued; with a magnified view of (b) Second fabrication, (c) interface bonded section, and (d) first fabrication.